Heavy ion beam transmission in the AGOR cyclotron

Sen, Ayanangsha

Heavy Ion Beam Transmission in the AGOR Cyclotron

To Lt. Dr. Jaydeb Prasad Sen
-at least I tried

COVER: Schematic representation of the three sectors of AGOR cyclotron with a couple of off-centered orbits (courtesy :Avik Kumar Maitra).

This work is part of the research programme of the Stichting voor Fundamenteel Onderzoek der Materie (FOM), which is financially supported by the Nederlandse Organisatie voor Wetenschappelijk Onderzoek (NWO). Additional funding was provided by the European Commission within the Seventh Framework Programme through IA-ENSAR (contract no. RII3-CT-2010-262010).

Groningen, March 2013

RIJKSUNIVERSITEIT GRONINGEN

Heavy Ion Beam Transmission in the AGOR Cyclotron

Proefschrift

ter verkrijging van het doctoraat in de
Wiskunde en Natuurwetenschappen
aan de Rijksuniversiteit Groningen
op gezag van de
Rector Magnificus, dr. E. Sterken,
in het openbaar te verdedigen op
maandag 18 maart 2013
om 16.15 uur

door

Ayanangsha Sen

geboren op 21 juni 1983
te Durgapur, India

Promotor:	Prof. dr. S. Brandenburg
Copromotor:	Dr. M. A. Hofstee
Beoordelingscommissie:	Prof. dr. ir. R.A. Hoekstra
	Prof. dr. ir. O.J. Luiten
	Prof. dr. K. Hatanaka

ISBN: (Printed Version)978-90-367-6040-9
ISBN: (Digital Version)978-90-367-6041-6

Contents

Chapter 1

Introduction

1.1 General introduction

The AGOR cyclotron is a superconducting cyclotron delivering heavy ion beams with energies of 5.5 MeV per nucleon and more, depending on the charge to mass ratio. The experiments in the framework of the TRIμP program [1] at the KVI require the AGOR cyclotron to produce a wide range of high intensity heavy ion beams. These beams range from ^{206}Pb at 8 MeV/amu to ^{20}Ne at 23.3 MeV/amu with a desired beam power of about 1 kW. The AGOR cyclotron has not been designed for such high intensities of heavy ions. To reach this high beam power an upgrade program was initiated, which included amongst others the ECR ion source, a beam loss monitoring system and a new actively cooled electrostatic deflector [2]. In addition we started to investigate the transmission of very heavy ions at low energy to order to get as close as possible to the required intensities and to identify the difficulties we would encounter. Transmission experiments were done with a range of heavy ion beams such as Ar, Kr and Xe accelerated to energies of 8-10 MeV/amu. It was observed that the transmission strongly depends on injected beam intensity, which was varied over a few orders of magnitude. In figure 1.1 the extracted beam intensity is plotted as a function of the injected intensity for a $^{40}Ar^{5+}$ beam with a final energy of 8 MeV/amu. The extracted intensity displayed is scaled to the current at the lowest injected intensity to account for the extraction losses.

At low intensities the extracted current is linearly proportional to the injected current as indicated by the solid line in the figure. As the beam current increases, the extracted intensity is observed to saturate. At high intensity the beam loss causes a significant degradation of the vacuum as shown in figure 1.1. During transmission beam particles collide with the rest gas atoms leading to beamloss. Apart from outgassing, the pressure rise is caused by the lost ions which deposit their energy on the walls of the cyclotron vacuum chamber and liberate materials, i.e. cause desorption. Outgassing depends on the macroscopic temperature increase while desorption is caused by the individual ions. A positive feedback is created between the pressure rise and beamloss, thus leading to increased losses.

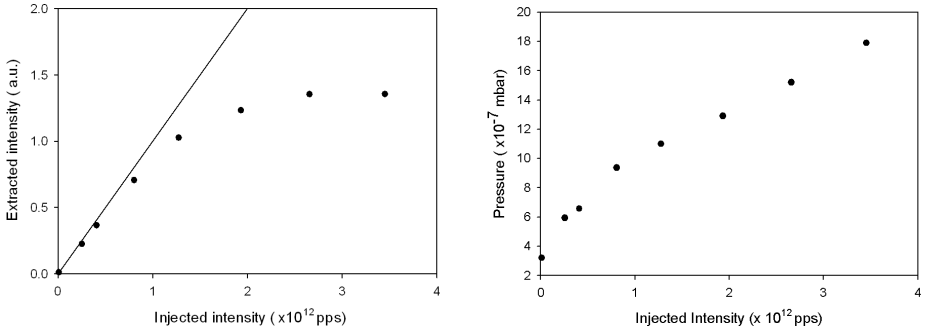

Figure 1.1: *Extracted intensity and corresponding rise in pressure for $^{40}Ar^{5+}$ at 8 MeV/amu as a function of injected intensity. The straight line indicates the linear dependence*

Beam induced outgassing and desorption in accelerators is not a new phenomena. The earliest observed beam loss due to beam induced desorption was in the Intersecting Storage Ring (ISR) at CERN in 1972 [3]. Beam loss induced vacuum degradation was also observed at LEAR (CERN) [4], RHIC Brookhaven [5] and the SIS18 at GSI [6].
The measurements shown in figure 1.1 were a part of the preliminary work done in 2004-2005 ([7] and [8]), and gave the motivation for the work presented in this thesis. Vacuum induced beam loss was identified to be a serious issue in accelerating high intensity heavy ion beams in our cyclotron [9]. The aim of the research presented in this thesis is to gain understanding of the beamloss processes in the cyclotron during acceleration of high intensity, low energy heavy ion beams, in order to improve their transmission and thereby the attainable beam intensity.
A simple approach to the feedback process is given in equations 1.1 and 1.2. Equation 1.1 gives an expression of the beam loss in the cyclotron [10]. The transmission T is the ratio of the extracted current I_{out} and the injected current I_{in}. Initial calculations were done for a base pressure P, assumed to be the same throughout the cyclotron. The attenuation co-efficient μ includes the cross-section and the path length of the particle in the entire machine.

$$T = \frac{I_{out}}{I_{in}} = \exp\left(-\mu P\right) \tag{1.1}$$

$$P = P_0 + Q_d(I_{in} - I_{out})/S_p \tag{1.2}$$

Equation 1.2 determines the rise in pressure as a function of the beam intensity lost in the cyclotron. Ions hitting the cyclotron vacuum chamber have a desorption co-efficient of Q_d and desorbed molecules are removed with a pumping speed S_p. The

instantaneous pressure P evolves from the base pressure P_0 and the intensity dependent component, and contributes to the feedback process in equation 1.1 and equation 1.2. The values of the pumping speed is assumed to be average over the cyclotron. The desorption co-efficient is assumed to be constant as a function of radius at which the ion is lost. In reality these values are not constants, so that the relative contribution of losses at a given energy may change as a function of intensity and pressure. Model calculations for a pressure P_0 = 10^{-7} mbar, show that for

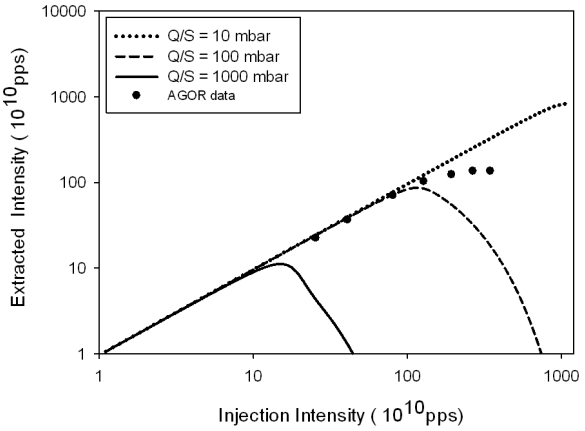

Figure 1.2: *Extracted intensity as calculated for different gas load (Q_d/S_p) using the model described in equation 1.1 and 1.2*

different Q_d/S_p (figure 1.2) the response of the exteacted intensity to the injected intensity varies considerably. The object of our study is to understand the beam loss process, and develop mitigation methods to reduce the feedback and increase transmission.

1.2 Beam loss mechanism

The beam loss mechanism is fueled by the feedback cycle indicated in figure 1.3. In their collisions with the rest gas molecules the beam particles have a certain probability to undergo a change of charge state. After such a collision the beam particles deviate from their initial trajectory, and they eventually end up hitting the walls of the cyclotron. The energy of these particles is deposited on the walls and causes desorption. This desorption leads to an increase in the pressure and thereby to an increase in beam loss.

To understand the beam loss mechanism, we have investigated the various pro-

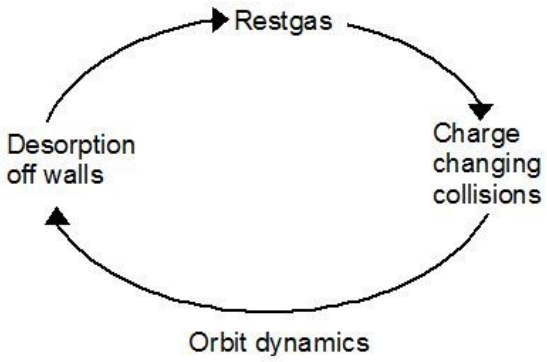

Figure 1.3: *Schematic diagram of the beam loss feedback cycle*

cesses shown in figure 1.3 and focused our studies on three components.

- Charge changing collisions: Beam particles undergo charge changing collisions with the rest gas and their trajectory deviates from that of the accelerated particles. This is the source of beam loss. At low intensity, where the feedback mechanism can be neglected, the transmission of heavy ion beams was measured as a function of pressure. In figure 1.4 we display the beam current in the interior of the cyclotron as function of radius from the center of the cyclotron at two different pressures. The figure shows that a rise in pressure by a factor of two reduces the transmission by approximately 60%. Measurements were, on purpose, made in bad vacuum with the help of the radial probe, discussed in section 2.5. The entire measurement will be discussed in section 3.4.1.

- Orbit calculations: Once particles have been lost, they ultimately hit the walls of the cyclotron. Orbit calculations track the lost ions and determine how and where these ions end up. The simulations are used calculate the angles of impact which are relevant in our case. The results are used as an input in our desorption studies.

- Wall desorption: Desorption for different heavy ion beams incident on different materials was measured under well-controlled circumstances, to give an estimate of the pressure rise caused by the lost ions. Studies measuring desorption yields have been done at several places including at GSI (U^{28+}) [11], at the ARRONAX Cyclone70 (H^-) (IBA) [12], and at CERN for LEAR (Pb^{27+}) [13]

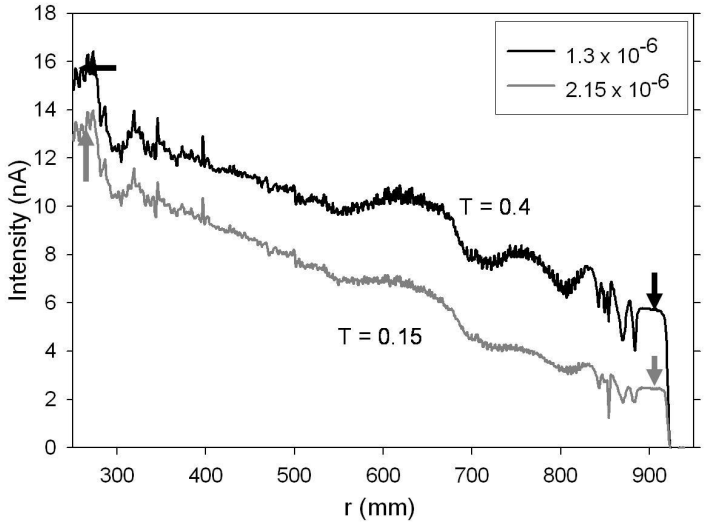

Figure 1.4: *Transmission for $^{40}Ar^{5+}$ at 8 MeV/amu with varying pressure in the cyclotron. (pressure in legend in mbars)*

and LHC (H^+)) [14]. A compilation of these desorption related experiments is given in [15]. Results from these experiments are not directly applicable to our situation for the following reasons:

- The AGOR cyclotron operates at a base pressure of 10^{-7} mbar as compared to 10^{-10} - 10^{-11} mbar base pressure in most of these accelerators.

- The energy regime we are interested in is up to at most 10 MeV/amu. The other facilities have a much higher energy range (10-150 MeV/amu U^{28+} at GSI and 9 GeV/amu Au^{79+} at RHIC).

- Based on our orbit calculations we expect angles of impact between 0° and 8°. Previous work has indicated a significant increase in the desorption yield at small angles of incidence as compared to perpendicular incidence [15]. The earlier experiments, however, looked at only two values for small angles of incidence [13]. For our case we needed a better angular resolution as compared to previous experiments.

1.3 Thesis outline

This thesis is organized in the following way:
In chapter 2 we introduce the AGOR cyclotron and describe its components, specifically the vacuum system. We also discuss beam dynamics for a cyclotron and conditions for horizontal beam stability. Chapter 3 looks at the specifics of charge changing collisions where we calculate beam transmission inside the cyclotron and compare them to transmission measured during low intensity experiments. Chapter 4 describes the orbit calculations where we simulated the trajectory of particles after charge exchange and tracked them till they ended up on the boundary walls. Results show that these particles are predominantly incident at shallow angles, which guided us in the design of the desorption experiment
In order to quantify ion-induced desorption we performed experiments to measure desorption yields of heavy ion beams incident on relevant materials at shallow angles of incidence. Chapter 5 describes the various existing models for desorption which might be applicable to our situation. Chapter 6 gives a description of the experimental setup for desorption measurements, the experimental procedure, and steps taken for data analysis. In chapter 7 we present our experimental results. We calculate the desorption yield from the observed pressure rise and quantify it based on various parameters. We also compare our observed results to the desorption yields predicted by the models. The desorption yield is also compared to experimental results in the cyclotron. In chapter 8 we summarize our conclusions on each of the subsystems of the desorption process as shown in figure 1.3 and give an outlook for the mitigation methods which may be used.

Chapter 2

AGOR cyclotron basics

2.1 Introduction

The aim of our studies is to improve the transmission of heavy ion beams in the AGOR cyclotron. In this chapter we will give an introduction of AGOR and its various physical aspects. We describe the magnets in the cyclotron and the vacuum conditions prevailing inside the machine. We also discuss the diagnostic tools which will be referred to in subsequent chapters.

2.2 The AGOR Cyclotron

The AGOR cyclotron is an evolved version of the first cyclotron built by Lawrence and Livingston in 1931 [16] which could accelerate protons to 80 keV. The AGOR cyclotron is a superconducting cyclotron which can accelerate light as well as heavy ions to high energies. It is a three sector cyclotron with three dees. The maximum kinetic energy of the accelerated particles T is is given either by the bending limit K_b or the focussing limit K_f (given by equation 2.1, where A is the atom is mass number and Q is the charge state of the particle). The bending limit is determined by the product of the maximum field strength possible and the extraction radius of the cyclotron. The focussing limit comes from the interplay between axial defocussing due to increasing fieldindex (needed to retain isochronism at higher energy) and decreasing axial focussing due to flutter decrease with increasing field (see Appendix B for a detailed explanation). For $(Q/A) < K_b/K_f)$, the magnetic field strength is the limiting factor while for $(Q/A) > K_b/K_f)$, the axial focussing is the limiting factor [17].

$$\frac{T}{A} = K_b \left(\frac{Q}{A}\right)^2 \; or \; K_f \left(\frac{Q}{A}\right) \tag{2.1}$$

AGOR has an effective bending limit K_b = 600 MeV and a focussing limit K_f = 200 MeV. Figure 2.1 shows the major components of the cyclotron; the yoke, the two pairs of superconducting coils, the RF structure and the axial injection system.

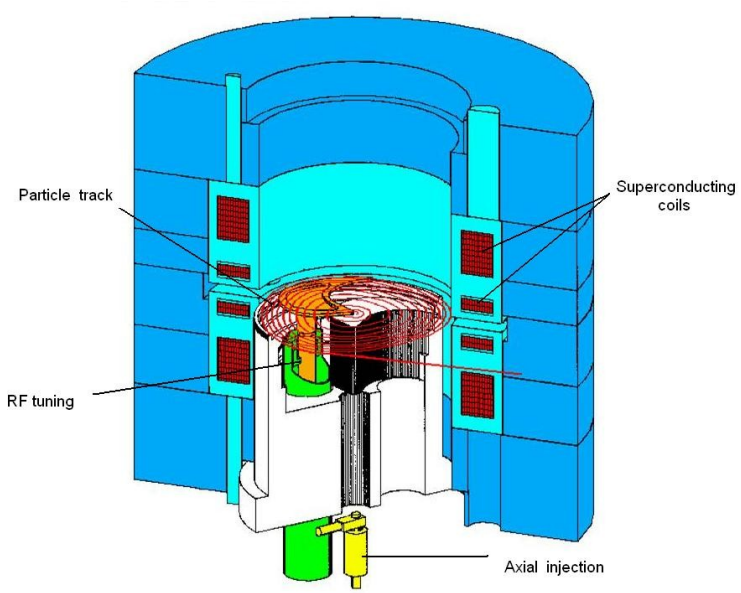

Figure 2.1: *Simplified cross cut of the AGOR cyclotron*

The operating range of the RF system is between 24 to 62 MHz and acceleration takes place in harmonics 2, 3 and 4 [18]. Figure 2.2 shows the operating diagram of the cyclotron representing all possible beams as a function of the charge over mass and energy over mass. The lines represent the operating limits while the dots correspond to the actual ions that have been accelerated. The upper curved limit line corresponds to the bending limit K_b = 600 MeV (for $\frac{q}{A} < 0.33$) and focussing limit K_f = 200 MeV (for $\frac{q}{A} > 0.33$). The lower limit corresponds to the resonance $\nu_r + 2\nu_z = 3$. The low energy limit is set by the minimum RF frequency while the maximum $\frac{q}{A}$ = 1 for protons.

2.2.1 Isochronism

Isochronism is the condition that the orbital period of a beam particle is independent of its momentum i.e. a particle takes the same time to complete one turn irrespective of the momentum.

$$\omega_{rev} = q\frac{\gamma B_0}{m} \tag{2.2}$$

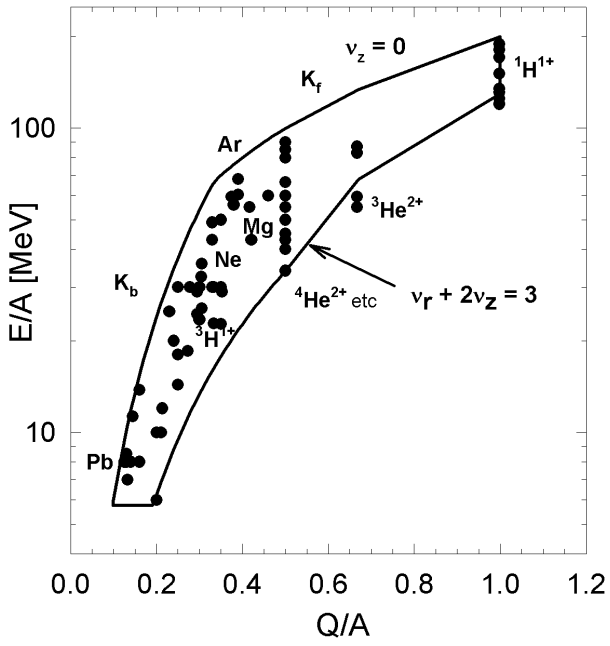

Figure 2.2: *Operating diagram and available beams for AGOR cyclotron*

In equation 2.2, B_0 is the average magnetic field at the center and m is the relativistic mass of the particle. The factor γ compensates the increase in the relativistic mass term to fulfill the isochronism condition. The revolution frequency is related to the RF frequency and the harmonic number h as given by

$$\omega_{RF} = h\omega_{rev} \tag{2.3}$$

The radial increase of the magnetic field required to maintain isochronism, results in vertical instability of the particle orbits, which is countered by introducing azimuthally varying fields [19].

2.2.2 Azimuthally varying field

Vertical focussing for particles is provided by introduction of sectors. Focussing is achieved by fields produced by wedge shaped extensions (Thomas focussing [19]). The raised regions are called hills and the recessed region called valleys. The succession of hills and valleys modulate the magnetic field in the azimuthal direction. The

azimuthal field variation produces a radial and tangential field component which along with the tangential and radial force components result in an axial force. Due to the tangential component of the field B_θ and the eccentric beam trajectory, a radial component of the velocity v_r is created. This results in a focussing axial force $F_z \propto \left(\bar{v_r} \times \bar{B_\theta}\right)$.
At higher energies the increase in the relativistic factor becomes large and thus the magnetic field increases rapidly along the radius. By spiraling the sectors, the valley-hill transition becomes more focussing and the hill-valley transition is less focussing. However, the stronger focussing at one edge has more positive effect than the negative effect of the smaller focussing at the other edge [20]. The spiraling of the sectors in the AGOR cyclotron is shown in figure 2.4 and figure 2.5.

2.3 Magnet

The magnetic field in AGOR is generated by 2 pairs of superconducting main coils and 15 sets of 6 trim coils [21]. The superconducting main coils can carry a maximum current of 900 A and 1600 A, respectively, to generate a maximum 4 T average field [22]. The large coil (figure 2.3) generates an average field slowly decreasing with radius [23]. The smaller coil closer to the median plane produces a field whose radial increase is substantially stronger than the radial decrease of the magnetic field of the large coil and the iron. With the right combination of currents in the main coils

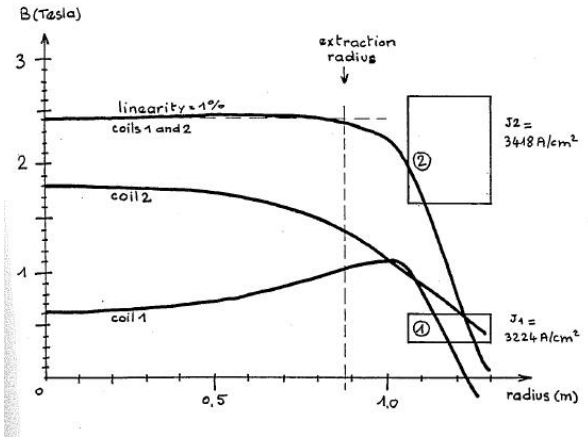

Figure 2.3: *Magnetic field strength for the two sets of main coils along the radius as shown in the design report*

both B_0 and the radial gradient required for a specific beam can be made with sufficient accuracy for isochronism. The trim coils correct the remaining deviations from isochronism. The average central magnetic field, B_0, ranges from 1.7 Tesla to 4.07 Tesla. The trim coils are shown in figure 2.4. The inner trim coils (2 and 3) help in centering the beam. The outer ones (14 and 15) are used to excite the ν_r = 1 resonance, and generate the precession motion (collective radial betatron oscillation) needed to increase turn separation and to orient the beam correctly at the entrance of the extraction system. At low field, the scalloping of the orbits becomes signif-

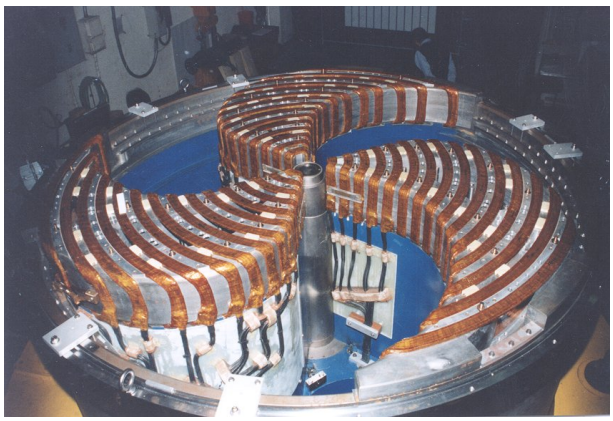

Figure 2.4: *Snapshot of the trimcoils and sectors in AGOR cyclotron (before the copper lining of the vacuum chamber is placed)*

icant due to the large azimuthal field variation. Due to this the beam will have to pass through a coupling resonance, $\nu_r + 2\nu_z = 3$, which the beam will not survive unless it passes through it very rapidly (about one turn). In our cyclotron the scalloping is reduced by introducing an additional shallow valley in the middle of the hill sector (width is approximately one-third of the total with of the hill) to shift the coupling resonance to a lower energy.

2.4 Vacuum system

The acceleration vacuum chamber of the AGOR cyclotron can be considered as a cylindrical pill box, 1 m radius with a height of 18 mm in the hill region. Surrounding the acceleration chamber, between the cryostats there is another vacuum chamber where the extaction elements are mounted. The entire vacuum enclosure is being pumped by two turbo pumps and three cryo pumps. The entire extraction system is in vacuum as well as the 6 RF electrodes and the RF tuning systems. Figure 2.5

shows a picture of the mid plane of our cyclotron with the RF liners (which connect the top and bottom vacuum chamber lids and close off the resonators radially) and the three extraction elements.

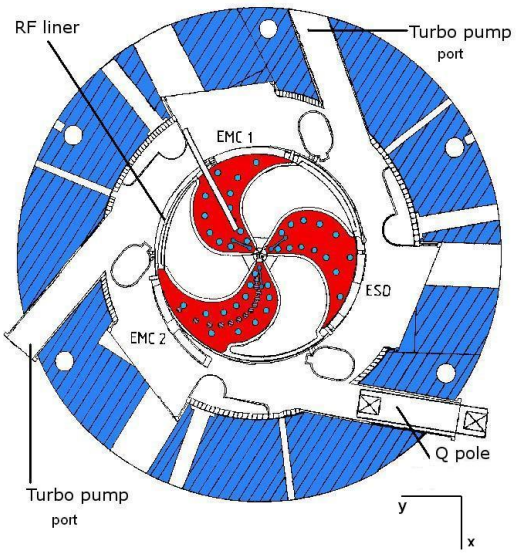

Figure 2.5: *Cross cut of the AGOR cyclotron showing the location of the turbo pump ports and the layout of the extraction elements (ESD, EMC1 and EMC2)*

Figure 2.6 shows the schematic diagram of the vertical crosscut of the acceleration vacuum chamber with the RF system. The RF liner and the extraction elements limit the conductance between the acceleration chamber and the turbo pumps. When the cryo pumps are switched off the vacuum in the interior of the cyclotron is not good enough to achieve full transmission for low energy heavy ion beams.
Normal operating pressure is 8×10^{-7} mbar, while for heavy ions additional cryo pumps gives a base pressure of 4×10^{-7} mbar [7], as measured near the external turbo pump. In the interior it is worse considering the low conductance. We do have additional pumping due to the cryo cooled extraction elements EMC2 and the Q pole. A study about beam transmission in the cyclotron and in the injection line is presented in section 3.4.1 and section 3.5.
Due to absence of an internal ion source, the gas load in the vacuum chamber comes only from outgassing. The sliding seals of the RF tuning mechanism have leaks and add to the gas load A typical rest gas spectrum of the cyclotron vacuum is shown in figure 2.7.

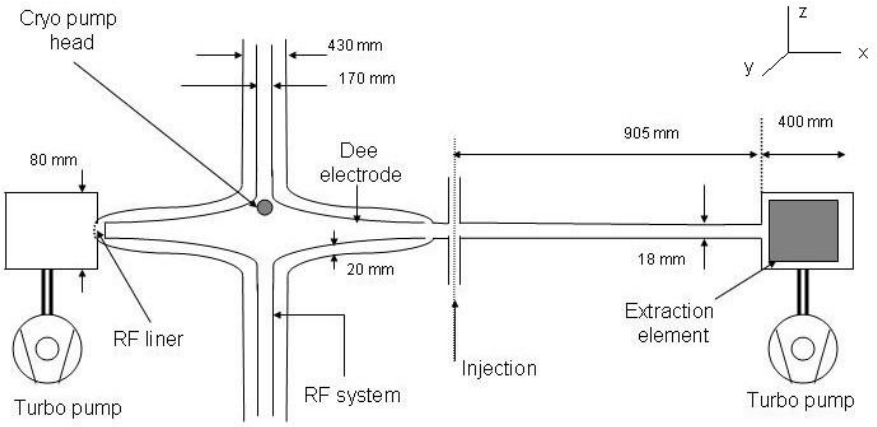

Figure 2.6: *Schematic diagram of the vertical cross cut of the AGOR cyclotron showing the location of the turbo pump ports and the RF system (not to scale).The cross cut follows a radius over the extraction element, then follows the symmetry line over a hill and subsequently a valley and then again follows a radius*

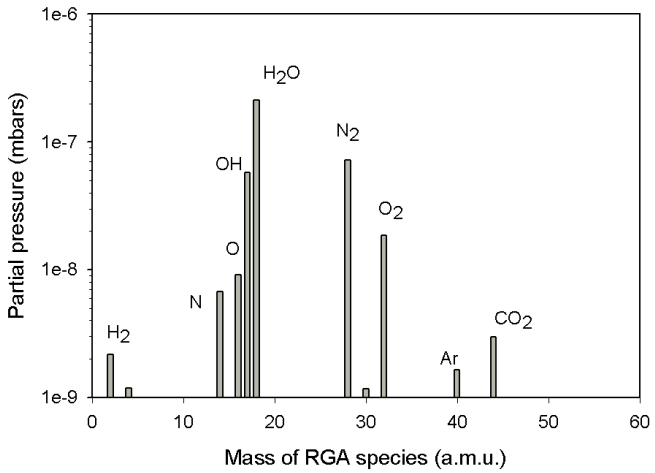

Figure 2.7: *Partial pressures of rest gas species measured in the cyclotron during pumpdown at a total pressure of 4×10^{-7} mbars at the RGA positioned on the circumference. Extraction elements are switched on and cryopumps switched off.*

2.4.1 The pumping system

The two turbo molecular pumps are connected to mid plane gap of the cryostat at the circumference. They individually have a pumping speed (at the pumps) of 850 - 1150 liter/sec for nitrogen [24]. In addition, there are three cryo pumps installed inside the three top RF electrodes to provide a higher effective pumping speed. The cold heads used to cool the cryo panels are located at the top of the upper RF electrodes away from the strong magnetic field. The measured pumping speed is 2000 liter/sec for hydrogen, 1200 liters/sec for nitrogen at 10^{-6} mbar [25] and 5000 liters/sec for water.
There are three pressure gauges situated near the circumference in the mid plane region near the turbo pumps. These gauges provide information about the gas load $Q = S \times P$. No measurement of the pressure in the interior of the cyclotron is possible under operating conditions. To estimate the pressure profile in the cyclotron we did some simulations using MOLFLOW [26] as described in Appendix A.

2.5 Beam diagnostic elements

Measurement of beam current inside the cyclotron has been performed with existing diagnostic equipment (see figure 2.8). In this section we introduce the elements we have used and discuss their performance.
Injection line:

- BSI4 :Faraday cup used to measure the current in horizontal section after the injection slits.
- BSI5 :Faraday cup which measures the beam current after BSI4. It gives a good relative measure of the injected current. Along with the reading of BSI4, measurements at BSI5 give an idea of the fluctuations in the ECR ion source.

Cyclotron:

- Radial probe : The radial probe is the most commonly used diagnostic tool. It consists of a block of copper with a tungsten wire attached at a slightly smaller radius and is used to measure the beam current in the interior of the cyclotron as a function of radius. A typical radial probe scan is shown in figure 2.9. The reading of the block does not give us the total current, since part of the current is intercepted by the wire. The wire is used as a diagnostic element to estimate the current density as a function of radius inside the cyclotron. The radial probe is designed to scan between the range of 250 mm to 950 mm. No measurements can be taken in the interior of the machine ($<$ 250 mm) since

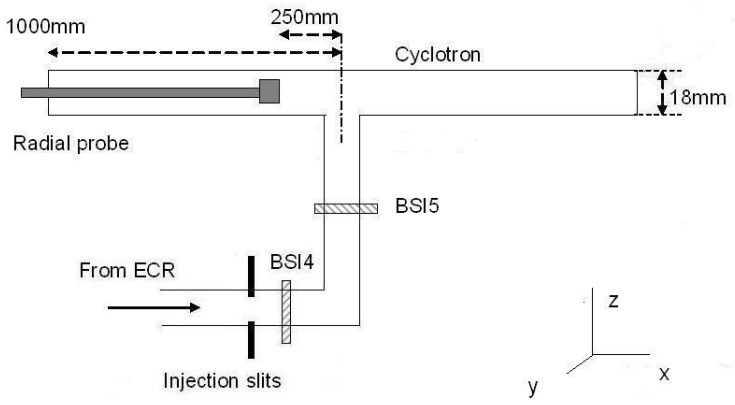

Figure 2.8: *Schematic diagram of beam elements in the cyclotron and injection line*

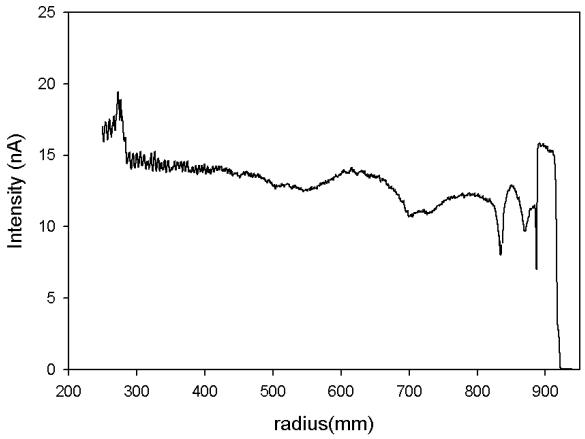

Figure 2.9: *Radial probe scan showing currents of block for $^{40}Ar^{5+}$ @ 8 MeV/amu; base pressure = 3.5×10^{-7} mbar*

the radial probe would then enter the acceleration gap. The radial probe also measures intensity of the extracted beam behind EMC1.

Extraction:

- BSX : This is a Faraday cup situated just outside the cyclotron . It is used to measure the current being extracted from the cyclotron.

Chapter 3

Charge changing collisions and beamloss

3.1 Introduction

As stated in chapter 1, beam loss in the AGOR cyclotron exhibits a positive feedback loop determined by two major interactions. In their collisions with residual gas atmosphere in the cyclotron beam particles have a certain probability to undergo a charge changing collision. After a charge changing collision particles will deviate from their original trajectory and eventually hit the walls of the cyclotron. The energy these particles deposit leads to desorption off the walls, which causes an increase in the pressure (a degradation of vacuum) in the cyclotron. This in turn leads to an increased probability of a change in charge state. In this chapter we will discuss the beam particle interaction with the rest gas, specifically charge exchange. We will estimate the total cross-section of the charge exchange process, using existing semi-empirical models, and predict transmission in the cyclotron and in the low energy beam line. These predictions will be compared to the measured transmission in the cyclotron.

3.2 Charge exchange

Of all possible interactions with the rest gas, charge exchange is the most relevant for our work involving fast heavy ion projectiles ([10], [27]). Beamloss due to rest gas interaction has also been observed in other comparable cyclotrons like the K500 cyclotron at NSCL [28].
The other relevant interaction is ionization of the rest gas which leads to vacuum degradation due to desorption induced by delta electrons. The other relevant interaction is ionization of the rest gas which leads to vacuum degradation due to desorption induced by delta electrons and ionized rest gas molecules. Because of the large cross section these particles may significantly contribute to the vacuum degradation, despite their low energy. However, we have no possibility to measure this contribution separately.

We include only single charge exchanges in our approach because the probability for multiple charge exchange in an inelastic collision is much smaller than single charge exchange [10].
There can be two kinds of charge exchanges in ion-atom collisions

- Capture or pickup : The beam particle [A] ionizes the stationary atom [B] and gains an electron.
$$A^{q+} + B \longrightarrow A^{(q-1)+} + \left[B^{+}\right] \tag{3.1}$$
- Stripping : The beam particle [A] collides with the stationary atom [B] and loses an electron.
$$A^{q+} + B \longrightarrow A^{(q+1)+} + \left[B + e^{-}\right] \tag{3.2}$$

The number of beam particles lost depends on the cross-section of interaction, the pathlength of the beam particle and the local density of rest gas at that particular radius. To estimate the total number of lost particles due to charge exchange we integrate the losses over all turns from injection to extraction. Given the small energy gain per turn, we approximate the particle track by 300 closed, constant energy orbits to simplify calculations. Each orbit has a fixed particle energy and the energy step between two orbits is taken to be constant. At the i^{th} orbit, the energy is given by:

$$E_i = E_0 + i\Delta E \tag{3.3}$$

The energy step between orbits, ΔE, is given by equation 3.4 where E_0 is the injection energy and E_f is the extraction energy for the particular beam.

$$\Delta E = \frac{E_f - E_0}{n} \tag{3.4}$$

The transmission at the ith orbit T_i, is calculated by equation 3.5.

$$T_i = \exp(-\sigma\left(E_i\right) L_i(E_i)\eta P) \tag{3.5}$$

In equation 3.5 the path length is given by the expression L_i for the ith orbit.

$$L_i = \frac{v_i}{\omega_{RF}/2\pi h} \tag{3.6}$$

The RF frequency is given by ω_{RF} , while h is the harmonic number as shown in equation 2.3. The velocity of the beam particle v_i is calculated from the energy E_i. The local pressure averaged over a single turn is given by P and η is Loschmidts number; the scaling factor between pressure and particle density. The cross-section of interaction σ depends on the velocity of the beam particle as discussed in the next

section. Finally we take a product of the transmission of all closed orbits to get the overall transmission.

3.3 Cross section calculations

There are several semi-empirical models which predict the cross sections of ion-atom collisions ([29] and [30]). If the velocity of the beam particle is much higher than the velocity of the electrons in the outermost orbital of the stationary rest gas atom, we have a short interaction time between the beam particle and the orbital electron. Increasing the velocity of the beam particle decreases this time of interaction and consequently the probability of capturing the orbital electron (by the beam particle) also decreases.
For stripping, at low energy, where the interaction time is determined by the electron orbital velocity of stationary atom, the loss cross section is proportional to the beam energy [31]. At high energy, where the beam particle velocity determines the interaction time, it is inversely proportional to velocity. For our calculations we have used three different models depending on the velocity of the beam particle and type of charge exchange. For electron capture two models have been used for low and high energies, respectively. For stripping there is a single model which is valid for all energies.

3.3.1 Capture at low energy

Low energy means that the projectile velocity is much less than the velocity of the outer orbital electron of the rest gas atom, which is captured. The velocity (v) of an electron in the nth orbit for an hydrogen like atom with atomic number Z is approximately given by

$$v = \frac{k_e Z e^2}{n\hbar} \tag{3.7}$$

where k_e is the Coulomb constant and $\hbar$ is the reduced Planck's constant. This equation does not include screening effects for many-electron atoms and relativistic effects, and is used to give a zero order estimate of v. For a hydrogen atom at ground state (Z = 1 and n = 1) the velocity of the electron v_0 = 2.2 $\times$ 10^6 m/s, which would correspond to a beam energy of 25 keV/amu.
According to the parameterization proposed by Schlachter [32] the low energy capture cross-section, $\sigma_{q,q-1}$, is independent of the projectile velocity. The capture probability is related to the balance between the Coulomb attraction force (between the projectile and the electron) and the binding energy of the electron. According to this model the capture cross section thus depends on the ionization energy (I_e) of the

Element / Molecule	Ionization potential (eV)
N	14.9
O	13.7
N_2	15.6
O_2	12.1
He	24.6
H_2O	12.6
H_2	15.4
CO_2	13.8

Table 3.1: *Ionization potential of different rest gas species*

stationary atom (eV) and on the charge (q)of the beam particle:

$$\sigma_{q,q-1} = 1.43 \times 10^{-12} \times q^{1.17} \times I_e^{-2.76} cm^2 \tag{3.8}$$

During initial calculations I_e for nitrogen was used as an approximation for the rest gas inside the cyclotron and the beam lines. Our calculation results have been compared to transmission experiments (section 3.4.1) where the pressure was varied by letting air into the cyclotron. The rest gas for these experiments can be assumed to be air. Approximation of the rest gas with nitrogen has also been used in vacuum calculations done at NSCL [33]. The values of the ionization potentials of most of the rest gas species are given in table 3.1.

At an operating pressure of a few $\times 10^{-7}$ mbar, the dominant rest gas species is water vapour. Taking a typical rest gas composition similar to the RGA spectrum as shown in figure 2.7, the ionization potential of the gas mixture is approximately 13.6 eV. Using ionization energy of nitrogen we underestimate the low energy capture cross-section by about 30 percent. In later calculations we have used this weighted ionization potential to calculate the cross-sections.

3.3.2 Capture at high energy

When the velocity of the projectile is much larger than the outer orbital electron velocity of the rest gas atom, the capture cross-section has a dependence on the velocity of the projectile as well as the charge state. According to Knudsen $et.al.$ [34], if the charged projectile is close enough to the atom for the Coulomb force between the ion and the electron to be larger than the centripetal force, the electron is released from the restgas atom.

$$R_r^2 \leq \frac{a}{mv^2} q e^2 \tag{3.9}$$

The release distance R_r gives the maximum distance between the projectile and atom at which the electron can be released from the atom, while q is the charge state of the beam particle. In equation 3.9 m, v, and a are the mass, velocity and orbital radius of the electron. When the potential energy of the electron in the electric field of the projectile is larger than its kinetic energy, the electron is captured by the projectile.

$$R_c \leq \frac{2qe^2}{mV^2} \tag{3.10}$$

Here V is the ion velocity. R_c is the maximum distance between the projectile and the electron at which capture can still occur. If an electron is released at a distance $R_r \leq R_c$ it is close enough to be immediately captured. The cross-section for this case is given by:

$$\sigma_1 = \pi R_r^2 \tag{3.11}$$

When $R_r \geq R_c$, the release of the electron takes place before capture can occur. The release is an adiabatic process which has a probability per unit time of the order of $\frac{v}{a}$ and capture can occur in a time of the order $\frac{R_c}{V}$ as described by Knudsen $et.al.$ [34]. In this case the probability that a released electron is captured is given by

$$\sigma_2 = \pi R_c^2 \left(\frac{v \times R_c}{a \times V} \right) \tag{3.12}$$

By summing the cross-sections in equation 3.11 and 3.12, an estimate of the total electron-capture cross-section is obtained, as detailed by Knudsen [34].

$$\begin{aligned} \frac{\sigma Z^{2/3}}{\pi a_0 q} = 5.085 \times 10^{-4} \int_0^{x_1} \left[e^{-x/3} x^6 \left(1 + 0.265x\right) dx \right] \\ +22.23 X^{-7} \int_{x_1}^{\infty} \left[e^{-4x/3} x^{-1} \left(1 + 0.265x\right)^4 dx \right] \end{aligned} \tag{3.13}$$

In equation 3.13 the parameter x is the reduced distance depending on a and the Bohr radius a_0 and v_0 is the first Bohr orbital velocity. The integration limit x_1 is given by the expression:

$$e^{x_1} x_1^7 \left(1 + 0.265x_1\right)^{-3} = 43714 X^{-7} \tag{3.14}$$

$$X = q^{-\frac{2}{7}} Z^{-\frac{8}{21}} \left(\frac{V}{v_0} \right) \tag{3.15}$$

3.3.3 Stripping

Stripping or loss of an electron from the projectile depends on the velocity of the projectile as well as binding energy of its outermost electron which has the largest probability of being removed. The stripping cross-section peaks when the projectile velocity is roughly 1-2 times the orbital electron velocity. The stripping cross-section is according to Franzke [35] described by equation 3.16.

$$\sigma_{q,q+1} = 3.5 \times 10^{-18+Y} \overline{q}^{-2} \overline{q}_T \left(\gamma^2 - 1\right) \left(\frac{q}{\overline{q}}\right)^b cm^2 \tag{3.16}$$

$$Y = (0.71 \log Z)^{1.5} \tag{3.17}$$

The parameter Y is calculated from the binding energies of the outer electrons [35]. The parameters $\overline{q}$ and $\overline{q}_T$ are the equilibrium charge state of the projectile and target respectively. The value of b is estimated from fit parameters and depends on the charge state (b= -4 for $q > \overline{q}$ and b= -2.3 $q < \overline{q}$). For an ion with atomic number Z_n, the equilibrium charge is calculated by equation 3.18 [36].

$$\overline{q} = Z_n \left[1 - \left(0.71 Z^{0.067}\right)^{\frac{\beta}{\alpha}}\right] \tag{3.18}$$

where β is the ratio of the projectile velocity to the speed of light, Z is the atomic number of the target and α is the fine structure constant.

In our calculations we have only taken single charge exchange under consideration. According to Knudsen $et.al.$ [34] the cross-sections for double capture are an order of magnitude smaller than single capture cross-sections.

3.4 Transmission calculations

Using the semi-empirical models for the cross section, the total transmission is estimated for beams accelerated in the AGOR cyclotron. From equations 3.3 and 3.4, we calculate the average energy at a particular orbit and subsequently determine the cross-section of charge exchange and pathlength for that orbit. The total trans-

mission, T, is then given by the product of the transmission of every turn.

$$T = \prod T_i \tag{3.19}$$

$$T_i = \exp\left(-\mu_i \eta P_i\right) \tag{3.20}$$

$$\mu_i = \sigma_i\left(E\right) \times L_i\left(E\right) \tag{3.21}$$

$$\sigma = \sigma_{q,q+1} + \sigma_{q,q-1} \tag{3.22}$$

As an example the different cross-sections for $^{206}Pb^{30+}$ as a function of radius inside the cyclotron are shown in figure 3.1. The low energy capture cross-section

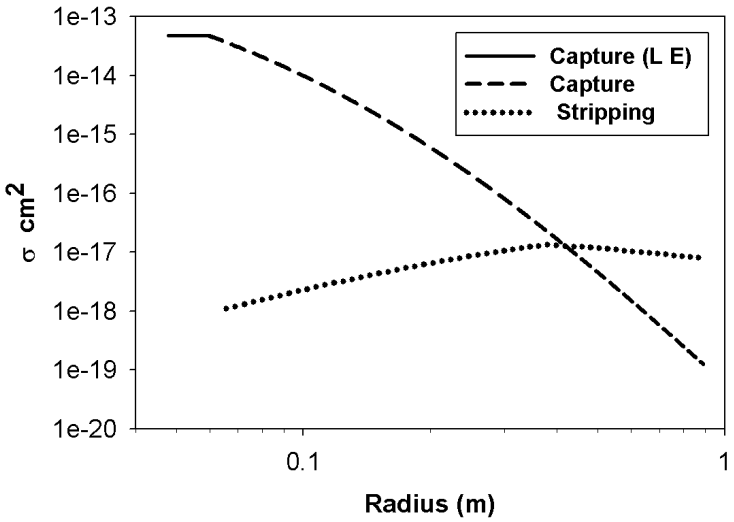

Figure 3.1: *Estimated cross-sections for $^{206}Pb^{30+}$; injection = 3keV/amu; extraction = 11.3 MeV/amu*

is applicable only for the first couple of turns, after which the high energy capture cross-section takes over. In the interior part of the cyclotron, capture dominates over stripping and is nearly 5 orders of magnitude higher. Near the extraction region of the cyclotron, stripping dominates.

The energy dependence of the total charge exchange cross section depends very significantly on the ion species, as is illustrated by figure 3.2, in which the cross sections for $^{40}Ar^{5+}$ and $^{206}Pb^{27+}$ accelerated to the same final energy of 8 MeV/amu are displayed.

Capture for $^{206}Pb^{27+}$ is much easier than $^{40}Ar^{5+}$, since the high charge state results in a stronger Coulomb attraction of an orbital electron in the rest gas molecule. Strip-

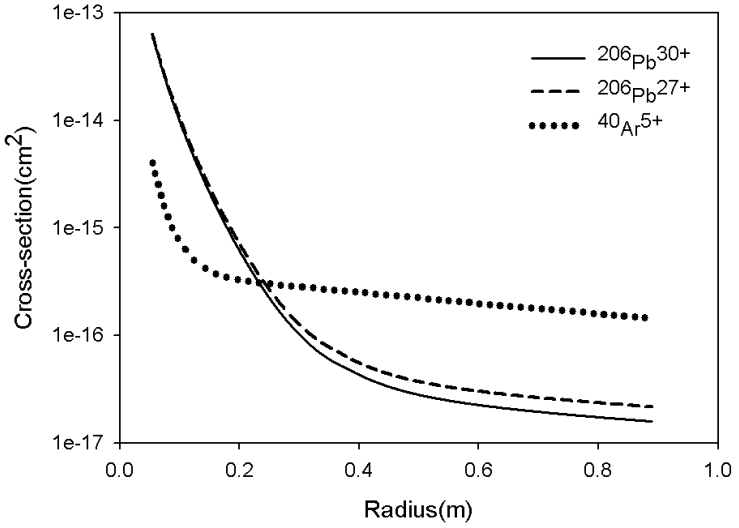

Figure 3.2: *Total cross-sections for different beams accelerated in AGOR*

ping is for the Pb more difficult than the Ar, since for a 27+ charge state the binding energy is much higher than the 5+ charge state.
The transmission inside the cyclotron can be estimated using equation 3.19. The to-

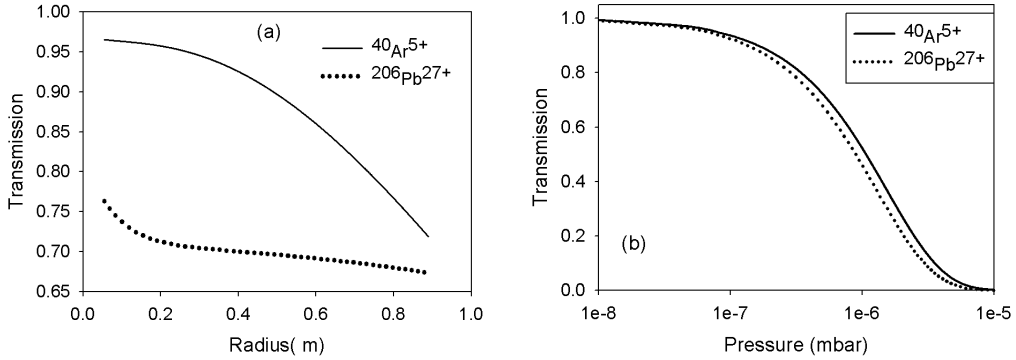

Figure 3.3: *Transmission for different beams accelerated to 8 MeV/amu in AGOR for (a) as a function of radius at a constant pressure 5×10^{-7} mbar and (b)as a function of pressure inside the cyclotron. Pressure in the injection line is equal to the pressure in the cyclotron.*

tal transmission depends on the product of the cross-section and pathlength of the ion. In the interior of the machine the cross-section is high but the path length is small. Near the extraction the cross-section is low but the path length is large. For $^{40}Ar^{5+}$ and $^{206}Pb^{27+}$ (figure 3.3a) the transmission as a function of the radius has been plotted. Transmission is calculated starting at the last Faraday cup in the vertical line (BSI5) and thus includes the 3.5 m vertical injection beam line (see figure 2.1) with a pressure of 5×10^{-7} mbar. Thus the transmission plotted for zero radius in the cyclotron for both beams is already less than 1.
Figure 3.3b gives an estimate of the transmission in the cyclotron as a function of the pressure. The pressure is assumed to be independent of radius in the cyclotron. The pressure inside the cyclotron in reality has a radial dependence. Simulations predicting the pressure profile have been presented in Appendix A. The pressure in the 3.5 m vertical injection line is assumed to be uniform and of the order of 5×10^{-7} mbar. The achievable pressure in the in the vertical injection beam line is relatively high due to the fact that no pumps can be mounted on this section because of design constraints. Since the cross-section is high at low energies, we expect large losses in this section, which decrease the overall transmission.

3.4.1 Cyclotron transmission measurement

Experiments have been performed to measure the transmission through the cyclotron. These measurements were done at low intensities, to reduce the contribution from ion induced desorption and outgassing from the radial probe. The pressure was then varied with the help of a controlled air leak near the RF resonators. The air flowed into the median plane through the gap between the dees and the pole cap and is assumed to give a homogeneous increase in pressure radially. The transmission inside the machine was measured as a function of the radius with the radial probe. The current measured by the radial probe is fractional because part of the beam is intercepted by the wire attached to the radial probe, as described in section 2.5. (In all subsquent discussions in this thesis beam current and beam intensity are equivalent.) The current intercepted by the wire varies as the radius. To eliminate effects of the wire the beam current is normalized to the current at a base pressure of 1.3×10^{-6} mbar at all radii and the ratio of the currents is plotted as the transmission as shown in figure 3.4. Further, for all pressures the currents at 250 mm have been scaled to the beam intensity at 250 mm at the base pressure, to account for any systematic effects due to source instability. In the figure the gray lines show the transmission as calculated by our simulations (also normalized to the transmission at the base pressure) giving a transmission of 1 at 250 mm radius (for the base pressure). It is seen for the lowest and highest base pressures , 1.5 and 5.1×10^{-6} mbar,

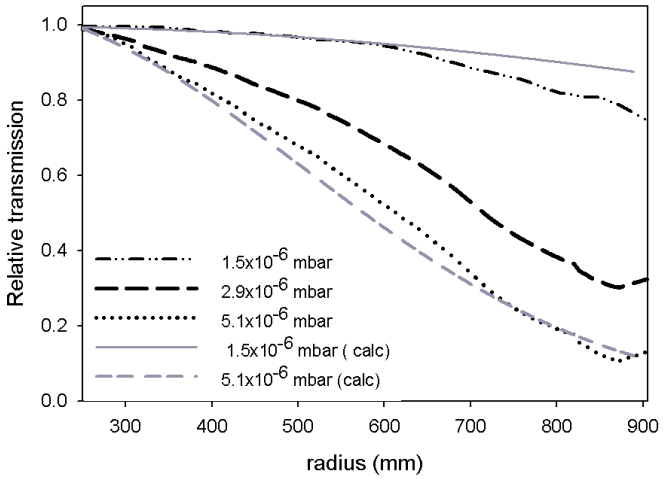

Figure 3.4: *Transmission at different base pressures as measured by the radial probe for $^{40}Ar^{5+}$ at 8 MeV/amu. Beam current has been normalized to beam current measured at a pressure of 1.3 $\times$ 10^{-6} mbars*

the slope of our calculated transmission and experimentally observed transmission is different. This can be explained by the presence of a non-uniform pressure profile especially in the center of the cyclotron (r $<$ 250 mm) where measurement is not possible.

To compare the transmission results from the radial probe experiments to our simu-

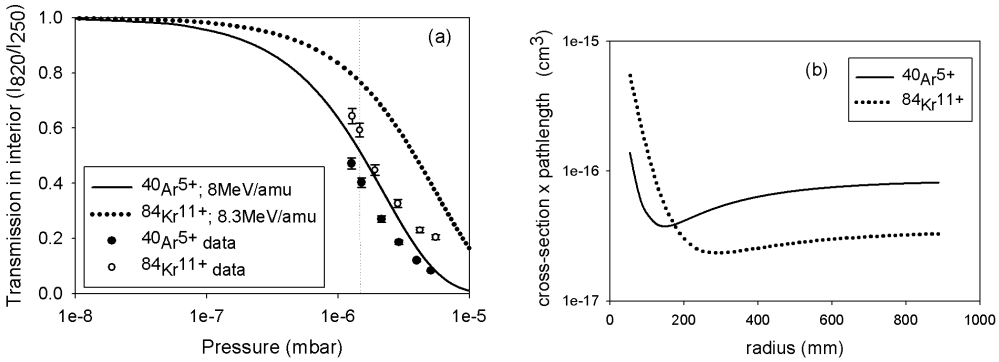

Figure 3.5: *Simulations for $^{84}Kr^{11+}$ and $^{40}Ar^{5+}$ at 8MeV/amu; (a): Comparison of transmission with experimental results (b): Cross-section $\times$ pathlength as a function of radius*

lations, we defined the transmission in the machine as the ratio of the beam current at a radius 820 mm to the beam current at radius 250 mm. In figure 3.5(a), the transmission at different base pressures has been plotted for both the simulations as well as the experiments. Comparison with experimentally observed transmission shows an overestimation in our calculated values. At a pressure of 1.45×10^{-6} mbar, experimental results for the Ar beam are about 22 % less than the calculated transmission values. For the Kr beam this difference is about 20 % at the same pressure.
This difference between the experimental and calculated values come from the systematic errors in both the pressure measurements and the cross-sections. The pressure used in our simulations is the value as measured in the pressure gauges near the turbo pumps without the cryo pumps. The pressure at the center of the cyclotron is significantly different from this measured value due to the low conductance in the interior. This uncertainity in pressure measurement results in our simulations to be off from the observed values by an arbitrary scaling factor. Figure 3.5(b) shows that the attenuation factor (cross-section $\times$ pathlength) as a function of radius is different for the two beams. Thus the response to a pressure change is different for both beams, explaining why the arbitrary scaling factor for ^{84}Kr is different compared to ^{40}Ar. The calculations give an estimate for the transmission of any beam as a function of pressure in our machine. In figure 3.5(a), the error bars represent a 5% error in the measurements taken by the radial probe. We also expect an error of about 20 % in the average pressure as seen in the pressure profile simulations A.3.
Experimental data [37], [38] have shown a good agreement with the predicted cross sections, especially for stripping, based on the formulas by Franzke et al. To estimate the quality of our simulations over a different pressure regime, experiments were done with a $^{40}Ar^{7+}$ beam at 12.3 MeV/amu. The pressure for this experiment was of the order of 4×10^{-7} mbar. Figure 3.6 shows the experimental observations (points) while the line shows the transmission as predicted by our simulations. The simulated transmission slope has been scaled to pass through the data point corresponding to the lowest pressure. The equilibrium pressure is this case is varied by increasing the beam current (from 200 nA to 2000 nA measured by the radial probe at 250 mm), similar to the rise in pressure observed during operation. The difference in the observations of figure 3.5 and figure 3.6 lies in the pressure profiles. For figure 3.5 the pressure is varied by letting in air from the RF, which gives a significantly different pressure profile than the Ar^{7+} experiment where the cryo pumps are operational and the pressure increase is caused by desorption at the outer radius and in the central region. The accuracy for our transmission estimation for any beam is limited by the determination of an accurate pressure profile inside the cyclotron. We are unable to measure the transmission in the interior of the machine ($r < 250$). This makes it impossible to determine the accuracy of our transmission estimation

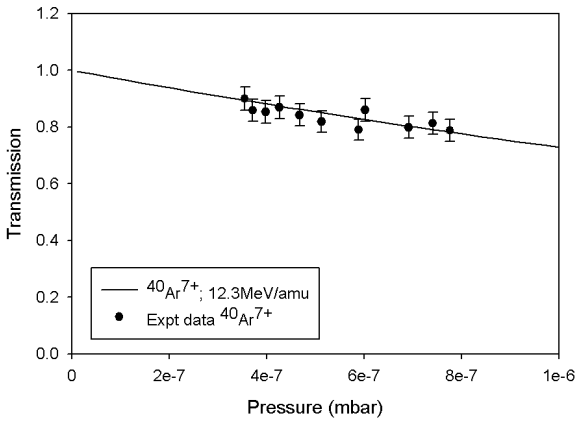

Figure 3.6: *Comparison of transmission between experimental results and simulation for* $^{40}Ar^{7+}$ *at 12.3 MeV/amu*

starting at the center of the machine.

3.5 Low energy beamline transmission

In the AGOR facility the beam produced at the AECR ion source is transported to the cyclotron through the low energy beam line. This beam line is divided into 4 segments - S_1 to S_4 (figure 3.7). While accelerating heavy ion beams a considerable loss is observed in the low energy beam line, which is caused by the high cross-section for capture at low energy. We performed experiments to verify our transmission simulations and determine the beam loss and dependence on pressure in the LEB line. Each of these segments has a pressure gauge which records the pressure in the beam line continuously. In the segment S_4 before the vertical beam line there is an intersection where beam line L_1 joins the main beam line.

3.5.1 Experiment

For our experiment a gas leak was introduced in the LEB line at the far end of L_1. An increase in the pressure in the beam line was observed for sections S_3 and S_4. The beam passed through the LEB line and its intensity was measured with the radial probe placed at a radius of 500 mm from the center of the machine. Measurements were taken at this radius to ensure that the beam consists of the selected ion species

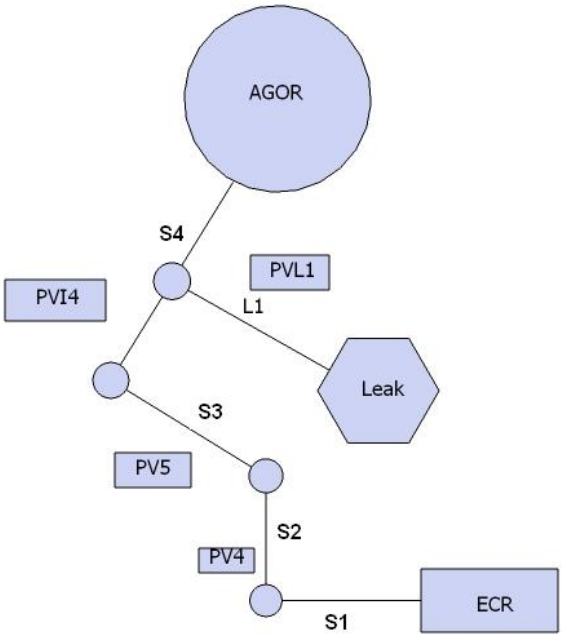

Figure 3.7: *Schematic layout of the LEB line in the AGOR facility*

only. The pressure in the LEB line was varied by controlling the gas flow with a needle valve. The pressure in the LEB line was increased and the beam intensity (post injection) measured, till the transmission had reduced significantly. The beam intensity measured is fitted with the expression

$$I = I_0 \exp\left(-\sigma\eta\left[\sum l_i.P_i\right]\right) \tag{3.23}$$

where σ is the cross-section for restgas interaction, l_i and P_i are the lengths and pressures of the i'th section of the LEB line. The exponential dependence of the beam intensity on the injection line pressure is shown in figure 3.8. The pressure distribution caused by the leak in the LEB line is non-uniform and scales with the pressure readings in each section. Thus the factor $\sum l_i.dP_i$ also scales with the readout pressure where $dP_i = (P2)_i - (P1)_i$ as described in equation 3.24.

3.5.2 Analysis and results

We do not get an accurate measure of the beam current I_0 at the ion source, as the current measured there includes other charge states. To eliminate this dependency we normalize the beam currents to the intensity at the lowest pressure. This also allows us to divide out the contribution from losses due to the initial pressure distribution. The transmission, T in the LEB line, when the leak is completely closed, is defined to be 1.

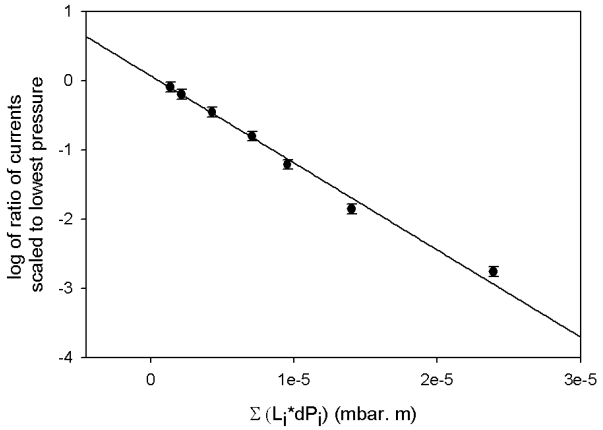

Figure 3.8: *Plot of logarithm of transmission as a function of* $\sum$ *length* $\times$ *rise in pressure*

$$T = \frac{I_2}{I_1} = \exp\left(-\sigma \times \eta \sum l_i \times [(P2)_i - (P1)_i]\right) \tag{3.24}$$

In equation 3.24 I_1 is the current measured when the pressure in different sections of the LEB line is $P1_i$ i.e. when the leak is closed, while I_2 is the current measured at pressure $P2_i$ for the i^{th} segment. A plot of the log of this transmission against the summed product $\sum l_i.dP_i$, gives us an experimental value of σ. From the regression line in figure 3.8 we determine a cross section σ = (4.5 $\pm$ 0.2)$\times 10^{-14}$ cm^2. This is in good agreement with the low energy cross-section given by [32]: 4.3$\times 10^{-14}$ cm^2. In figure 3.9 the measured transmission in the LEB line is plotted as a function of the average pressure in the LEB section. The fit in 3.8 also determines the initial beam current. We use that to scale the calculated transmission to the observed transmission. We assume that the pressure in each sections of the LEB line is constant. The total length of the LEB line is 16 m.

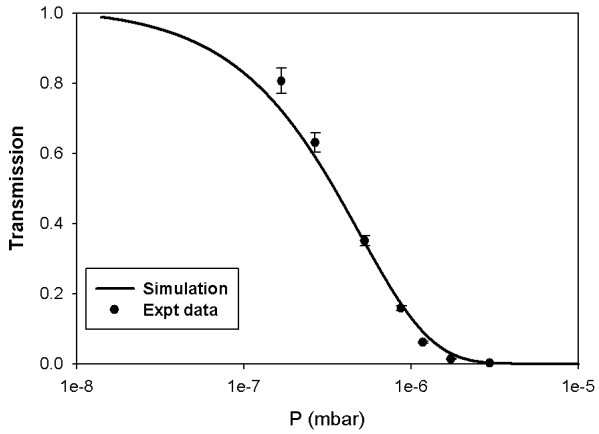

Figure 3.9: *Plot of transmission of $^{206}Pb^{30+}$ at 2.7 keV/amu as a function of average pressure in LEB line*

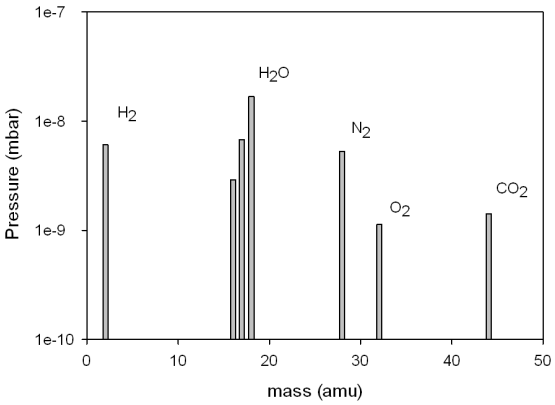

Figure 3.10: *Restgas spectrum in the LEB line after bakeout and replacement of seals as measured by the RGA*

Based on the experimental results we took steps to improve the pressure in the injection line. Baking out of the LEB line and replacing viton seals with copper seals in the beam line resulted in a pressure $< 3 \times 10^{-8}$ mbar (figure 3.10). This gives a transmission of more than 90 % for $^{206}Pb^{30+}$ in the LEB line as can be deduced from the figure 3.9.

Chapter 4

Cyclotron orbit dynamics

4.1 Introduction

In the previous chapter we looked at beam loss due to charge changing collisions. Charge exchanged particles are not accelerated anymore along with the rest of the beam particles due to a change in their charge over mass ratio. Under the influence of the magnetic field, these particles circulate in the cyclotron along a complex trajectory until they eventually, possibly after additional charge exchanges, hit a solid surface and deposit their energy. In this chapter we present simulations tracking the lost particles after charge exchange till they hit the walls of the cyclotron. We have studied the trajectory of particles post a single charge exchange. The aim of the simulation is to determine the region of impact of these lost particles on the walls, the angle of incidence (the angle which a particle hitting the chamber walls makes with the surface)and the energy distribution of particles hitting the walls. The latter depends on the radius at which the initial charge exchange occurred.

4.2 Magnetic field

We want to simulate the track of particles in the AGOR cyclotron. For that a realistic representation of the magnetic field in the cyclotron is used. This fieldmap is generated using existing, measured fieldmaps for different main coil and trim coil currents to accurately tune the field for a particular charge over mass ratio as described below.

4.2.1 Field map generation

For our calculations we have used a field map for $^{129}Xe^{26+}$ accelerated to 18 MeV/amu. For all other cases, a new field map can be generated. Most of the heavy ion beams under consideration in this thesis, have similar average field strength, compared to the $^{129}Xe^{26+}$ beam with an average field strength of 3.45 Tesla. For example for the $^{40}Ar^{5+}$ beam the average field strength is 3.64 Tesla. The comparable field strengths

of the beams indicate that the orbit for these beams are similar.
The field map is a grid of points in the (r,θ) plane, with a spacing of 5 mm in r and 1° in azimuth. For a particular beam the values of the main coil currents are estimated from the required B_0 and the final energy. First a field map is generated using a cubic spline interpolation of existing field maps measured for different sets of main coil currents. The local deviations from isochronism are then minimized by fitting the main coil and trim settings with a closed orbit tracking code [39]. Subsequently the phase profile ϕ_r is optimized over all radii to minimize the total phase slip integral, and the final fieldmap is calculated.

4.2.2 Field map calculation

The field map generated is a discrete map represented in a grid. For our simulations we need a continuous field map which gives the value of $B_z(r, \theta)$ at every point where we integrate the equations of motion. As $B_z(r, \theta)$ is periodic over θ a Fourier

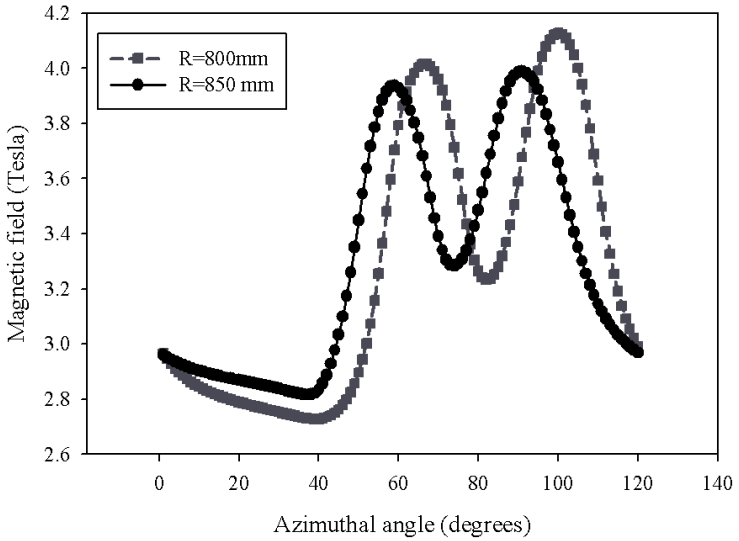

Figure 4.1: *Actual field map for $^{129}Xe^{26+}$ (18 MeV/amu) at different radii from the center of the machine*

transformation was done to determine the Fourier coefficients as a function of r. A recombination of these coefficients truncated at the 60th harmonic then gives the value of B_z at any particular θ. The higher order coefficients do not contribute to the

quality of the fit and their contribution is smaller than the noise level in the measurements. The Fourier reconstruction is made using only the third order harmonics, so that the final map will have the threefold symmetry of the cyclotron. Small first and second order harmonic terms are present actual magnetic field and influence particle trajectories close to extraction. For our current analysis they are not relevant.
To calculate the magnetic field at any point R, Θ, we first determine, the four grid lines in r co-ordinates which are on either side of R i.e. r_{i-1},$r_i < R < r_{i+1}$, r_{i+2}. From these four point we use the Akima spline interpolation method [40] to calculate the Fourier co-efficients for R. A reconstruction with the angle gives us the field value $B_z(R, \Theta)$. Figure 4.1 shows the calculated magnetic field for two different radii. The points represent the grid magnetic field map while the lines are a plot of the value of B_z as a function of θ calculated from the Fourier coefficients for this particular radius. A 3 dimensional plot of the magnetic field is shown in figure 4.2.

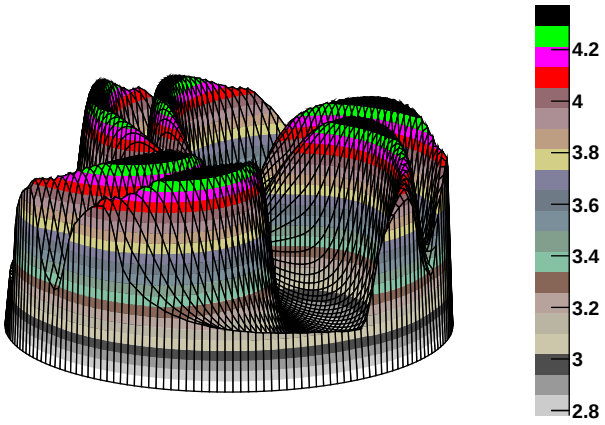

Figure 4.2: *3D view of the actual field map for* $^{129}Xe^{26+}$

4.3 Calculation of stable orbits

To determine the trajectory for particles after a charge exchange, it is necessary to first determine the orbit of the original ions. This serves as the starting point for the charge exchange. Given the small energy gain per turn, the spiral trajectory of a particle can be represented by a number of closed orbits (100 in our calculations) at

different energy and radii. Each closed orbit has a fixed energy and a corresponding average radius. To determine the track of a closed orbit we solve the equations of motion shown in equation 4.1-4.6 adapted from equations of motion used in tracking programs developed by TRIUMF [41]. In our calculations, we have taken the path length s as the independent variable.

$$r^{'} = \frac{dr}{ds} = P_r \tag{4.1}$$

$$P_r^{'} = \frac{dP_r}{ds} = \frac{P_\theta^2}{r} + \frac{q}{p} \times B_z \times P_\theta \tag{4.2}$$

$$\theta^{'} = \frac{d\theta}{ds} = \frac{P_\theta}{r} \tag{4.3}$$

$$P_\theta^{'} = \frac{dP_\theta}{ds} = -\left[\frac{P_r P_\theta}{r} + \frac{q}{p} \times B_z \times P_r\right] \tag{4.4}$$

where

$$P_r = \frac{p_r}{p} \; ; \; P_\theta = \frac{p_\theta}{p} \tag{4.5}$$

and

$$p^2 = p_\theta^2 + p_r^2 \tag{4.6}$$

The equations of motion are solved numerically using a Runge Kutta 4 integration method [42]. For a closed orbit with constant energy, the charge over momentum ratio is a constant. The integration method is energy independent and preserves the area in r, p_r phase space. For a particular orbit we calculate the initial radius r as shown in equation 3.6 and take an arbitrary θ as the initial co-ordinates. Fixed step sizes are taken in s for which r, p_r, θ and p_θ are calculated. After the particle traverses 120° (keeping in mind the three fold symmetry), we look at the difference between the r and p_r at the initial azimuth and the values after 120°. Since we take steps in the pathlength s, after a particular step we might not exactly be 120° from the starting azimuth. For this we look at two points before and after the crossover step where the particle crosses 120°. By taking a weighted average of these two points, we determine the final co-ordinates of the particle after a single turn.
For a closed orbit the necessary condition is for the particle to have the same co-ordinates after a single turn. To cope with truncation errors in the numerical integration process we define a convergence criterium for closed orbits. If the difference between the co-ordinates is less than a pre-ascertained value (a relative difference of 10^{-6} in our case), then the convergence condition is satisfied and that particular value of r and p_r is recorded as the co-ordinates for the particular closed orbit. If the difference is greater then we use it to determine a correction factor to r and p_r and

then run the simulation again.

4.3.1 Estimation of correction factor

To estimate the correction factor we first determine the first order transfer matrix for one third of the orbit and then solve for the eigen vector of this matrix. Using the difference after one third of the track and this eigen vector we calculate the correction to the initial conditions. We iterate the simulation with this correction factor until the termination condition is satisfied. We have observed that the orbits which satisfy the convergence criterion are stable with a relative accuracy ($\frac{\partial r}{r}$) of 10^{-4} over at least 60 turns.

4.4 Simulating a charge exchange

Once we have the initial conditions for the closed orbits, we simulate a charge exchange. We start with a stable orbit track, and at a particular azimuth change the charge state of the particle. We assume that the charge exchange process is instantaneous and that there is no momentum change of the beam particle. The charge exchange is implemented by changing p/q keeping the total momentum $\vec{p}$ and the radius $\vec{R}$ unchanged.
In a charge exchange a fast beam particle interacts with an electron of the rest gas atom. Due to the heavy mass of the projectile and light mass of the electron, the energy loss of the projectile is at most a few keV, resulting in a very small transverse momentum transfer. This small momentum transfer has also been observed in experiments ([43], [44]). Due to the negligible transfer of transverse momentum, the projectile scattering angles in our case are of the order of μrad [45]. At injection the beam has an emittance of about 100 π mm mrad. The spatial size of the beam is about 2 mm giving an angular divergence of 50 mrad. When compared to the angular displacement of μrad we conclude that the momentum transfer in the collisions does not change the radial and axial betatron amplitude of the particles and thus does not influence the motion of the particles. The change in charge to mass ratio of the ion, however, results in a large radial betatron amplitude.
We have not taken acceleration into consideration after the beam particle undergoes charge exchange ($\Delta q = 1$) because of the huge phase slip per turn. The phase slip per turn $\partial\varphi$ is given by:

$$\partial\varphi = 2\pi h \frac{\Delta B}{B} = 2\pi h \frac{\Delta q}{q} \tag{4.7}$$

For a heavy ion beam like $^{206}Pb^{27+}$ the relative change in charge state for a single charge exchange ($\frac{\Delta q}{q}$) is 3.8%. Combined with a harmonic number h = 4 , there is

a 54.7° phase slip per turn i.e. after approximately 6 turns the particle comes back at the same phase. A particle approximately takes 300 turns to reach extraction and there are 6 acceleration gaps in each turn (due to the three fold symmetry). A particle with extraction energy of 18 MeV/amu has an average energy change of 10 keV/amu for every acceleration gap. The change in the momentum for a charge exchanged particle after each acceleration gap is small and the fast changing phase component results in either an acceleration or deceleration after a turn. When averaged over multiple turns the net change in momentum is negligible. Combined with the large phase slip the low momentum change per turn leads us to conclude that acceleration does not significantly influence the trajectory of the ions after charge exchange.

4.4.1 Single charge exchange

The resulting trajectory of the particle is tracked using the equations of motion (equation 4.1) and the magnetic field map. The track of particles after a charge exchange is shown in figure 4.3.

In figure 4.3 the middle particle track represents the stable closed orbit. At an azimuth of 270° a charge exchange is simulated. The outer curve shows the trajectory after capture, while the inner curve shows the trajectory after stripping. For the $^{129}Xe^{26+}$, a single charge exchange results in a 3 - 4% change in the radius of curvature at that azimuth from the stable orbit. This change in radial curvature is equivalent to giving the particle a kick in the radial betatron amplitude of the same order. The orbit center shifts from the closed orbit center and the particles starts precessing in an off-centered band as shown in figure 4.4. In the figure we have followed the particle for 100 turns only. Allowing the particle to continue precessing would result in the entire band being filled up. The off centered band resulting from a single collision as seen in figure 4.4 does not move the particle track out of its region of stability. These particles continue to precess in their off-centered stable orbit until there is a second or a third charge exchange, depending on the $\frac{\Delta q}{q}$ per charge exchange.

To examine the effect of a charge exchange on the particle track and its relation to the region of stability we represent the trajectory of the charge changed particle in a phase space diagram (in r and p_r). Figure 4.5 shows the phase space diagram for particles after a charge exchange at an energy of 10.8 MeV/amu. Given the 3 fold symmetry of the machine we have simulated the collision at different azimuths in intervals of 24° over a single sector. In this figure r and p_r are plotted at a fixed azimuth of 30° (irrespective of the location of the charge change) at each turn follow-

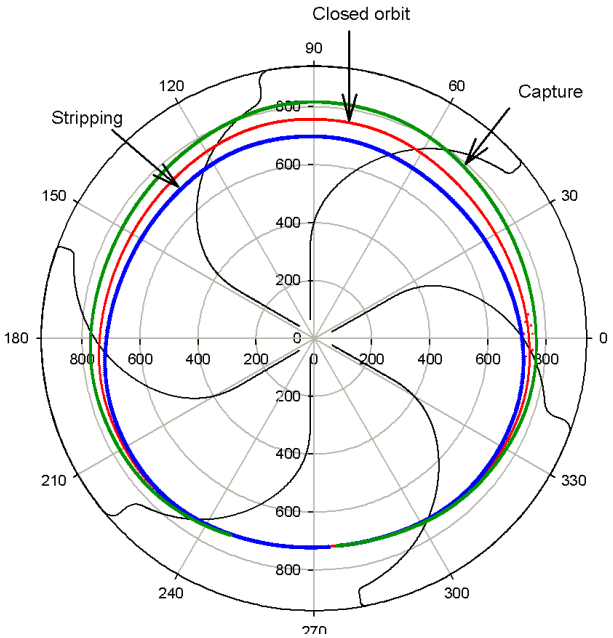

Figure 4.3: *Trajectory of charge exchanged ions post charge exchange for $^{129}Xe^{26+}$ extracted at 18 MeV/amu*

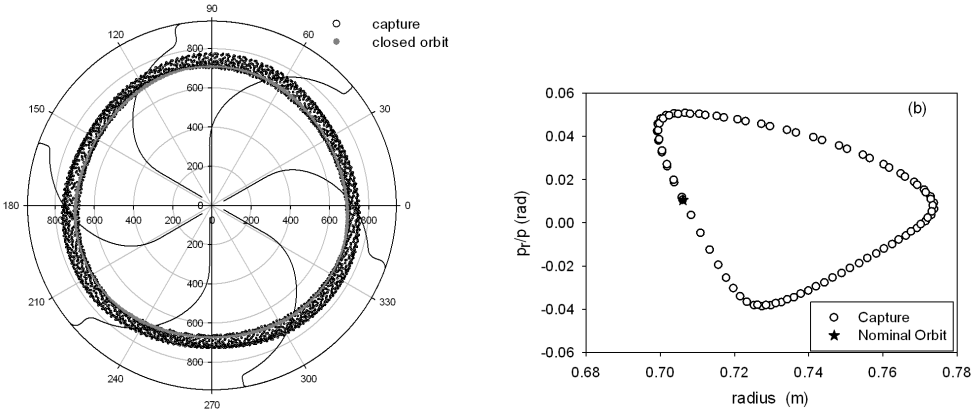

Figure 4.4: *Off-centered band of charge exchanged ions post capture and the corresponding nominal closed orbit for $^{129}Xe^{26+}$ at an energy of 10.8 MeV/amu: (a) polar plot (b) phase plot*

ing a charge exchange. For all test cases we see that the particle trajectory in phase space forms a closed loop. The phase space trajectories for charge exchanges at dif-

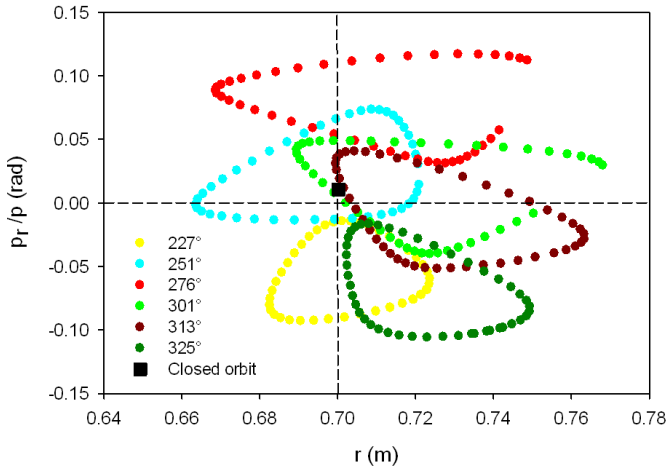

Figure 4.5: *Phase diagram of particles post a single charge exchange (stripping) at various azimuths for $^{129}Xe^{26+}$ at an energy of 10.8 MeV/amu*

ferent azimuths seem to rotate. These simulations have been done after tracking the particles for a fixed number of turns. For some azimuths the phase space trajectory is closed while for some they are not yet closed. This indicates that the local radial betatron frequency after charge exchange is different for different azimuths. From the location of the point of charge exchange, we observe that particles undergoing a charge exchange in the hill sector have a smaller increase in betatron amplitude than those that undergo charge exchange in the valley sector. This is due to the fact that in the hill sector the radius of curvature of the orbits is smaller, so that the change in radius (equal to a change in radial betatron amplitude) is also smaller. The larger betatron amplitude is associated with a smaller betatron frequency as the trajectory of the particle in phase space will be closer to the stability limit.

4.4.2 Energy dependence

To analyze the stability of this off-centered motion, we performed simulations introducing different changes in charge state at an arbitrary azimuth for various initial energies. Any particle that has undergone a charge exchange will eventually end up on the inner or outer walls of the vacuum chamber. For the outer walls of the vacuum chamber we define a limit at a radius of 0.905 m where the extraction ele-

ments are placed. In the interior of the machine we have posts connecting the upper and lower dees which also serve as physical obstructions for the particles. We have included the effect of the posts by defining an inner boundary at 0.030 m [46] where the track of the charge exchanged particles would get terminated.
In these simulations, particles undergo an arbitrary change in $\frac{\Delta q}{q}$ which does not correspond to a unit charge change. The calculations have been done in this way to obtain a more generic solution and to observe the region of stability with smaller steps. A percentage change in charge state also gives a comparison of different ions. A single charge exchange for $^{129}Xe^{26+}$ or $^{206}Pb^{27+}$ corresponds to a 4% charge change, while a single charge exchange for $^{40}Ar^{5+}$ corresponds to a 20% charge change. So the effect of a single charge exchange for the Ar beam corresponds to the effect of at least 5 charge exchanges of the Pb beam. In figure 4.6 the phase

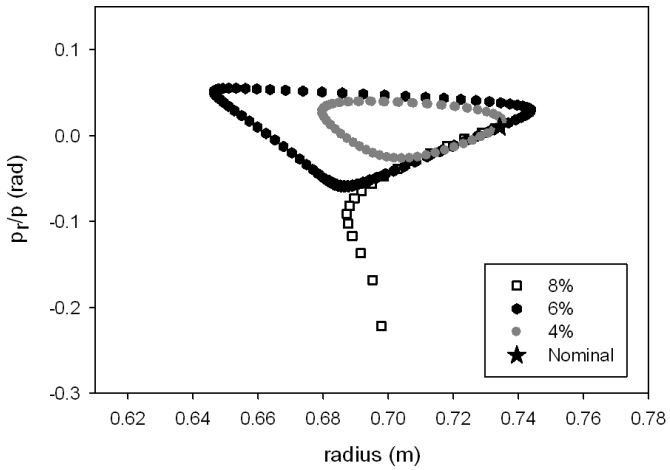

Figure 4.6: *Phase diagram of particles at the azimuth of charge exchange (215°) at an energy of 11.7 MeV/amu for $^{129}Xe^{26+}$ for different charge state changes*

space trajectory is plotted for charge exchange at a closed orbit with an energy of 11.7 MeV/amu. The phase space diagrams plot the radial momentum as a function of radius at an azimuth of 215° while the particle precesses in its off-center track. A particle orbit becomes unstable only if the change in charge ratio is larger than 8 %. The azimuth at which this diagram is plotted does not coincide with a symmetry point in the field so for the closed orbit (given by the black point) $p_r \neq 0$. The results from the simulation are valid for this azimuth of charge exchange and will be slightly different for charge exchanges at other azimuths.

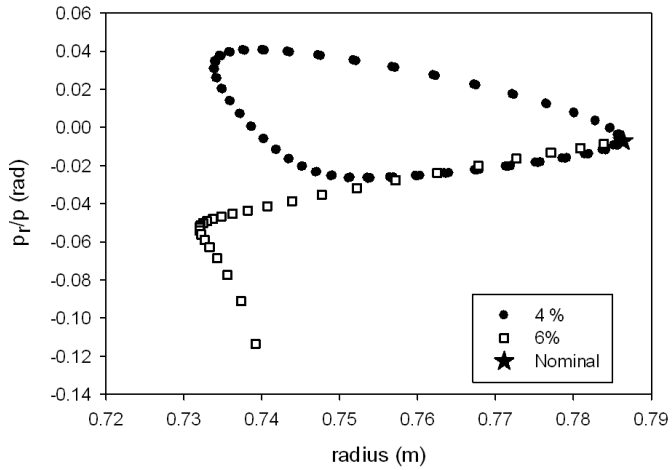

Figure 4.7: *Phase diagram of particles at the azimuth of charge exchange (215°) at an energy of 13.5 MeV/amu for $^{129}Xe^{26+}$ for different charge state changes*

Figure 4.7 shows that at an energy of 13.5 MeV/amu a 4 % increase in charge state does not lead the particle orbit to become unstable. Only a 6 % change makes the track unstable. As we move outwards to the extraction region, the area of stability in terms of $\frac{\Delta q}{q}$ becomes smaller and fewer number of charge exchanges are required before the orbit of these particles becomes unstable and they hit the walls of the machine. This is evident in the phase space trajectory for a particle after charge exchange at an energy of 15.3 MeV/amu in figure 4.8, which shows that a 4 % in charge state already results in an unstable orbit. For the Xe or Pb, several charge changing collisions are required in the interior of the cyclotron before the particle can go on to hit the walls. It is important to note that the effect of two charge exchanges is not similar to the effect of a double charge exchange. The effect of a subsequent charge exchange depends on the azimuth and the position of the particle in its precession motion at which the next collision occurs. The betatron kick of the next charge exchange adds up vectorially with that of the previous ones giving a resultant betatron amplitude which determines the track of the lost ions. It is similar to a random walk, so that the resultant betatron amplitude grows on average with the square root of the number of charge exchanges.

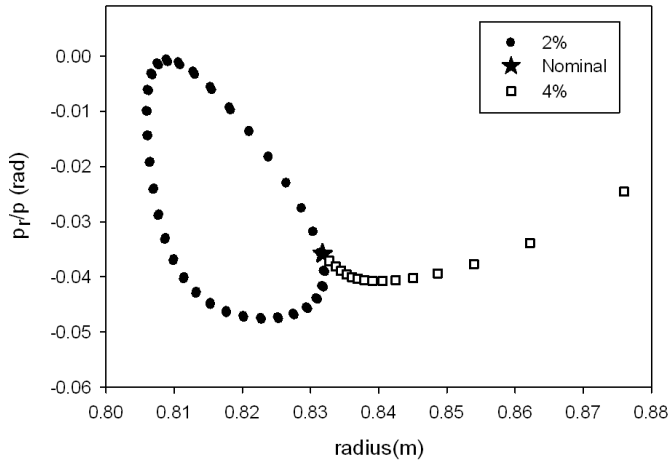

Figure 4.8: *Phase diagram of particles at the azimuth of charge exchange (215°), at an an energy of 15.3 MeV/amu for $^{129}Xe^{26+}$ for different charge state change*

4.4.3 Azimuth dependence

The stability of the off centered orbit not only depends on the radius at which the charge exchange occurs but also the azimuth at which it occurs. This azimuth dependence is illustrated in figure 4.9 which shows the particle trajectory after charge exchange at different azimuths. For some azimuths the orbit becomes unstable and the particles hit the walls of the machine after a few turns, while for other azimuths the orbit remains stable. The particles are lost near the maximum amplitude of the radius which corresponds to the hill sector. The particles with stable orbits continue to precess in their off-centered band till there is a further change in charge state.
From our simulations we conclude that only particles having near-extraction energies hit the walls after just a single charge exchange. A large percentage of particles have charge exchanges at lower energies which correspond to closed orbits in the interior of the cyclotron . We did simulations to investigate the trajectory of charge exchanged particles at lower energies. The phase space trajectory for charge exchanged particles from one of the inner closed orbits is shown in figure 4.10. From this figure we can conclude that particles would have to undergo at least two to three more charge exchanges before their orbit becomes unstable. The region of stability for stripping (increase in charge state) is less than capture (decrease in charge state), indicating that stripped particles will hit the walls much than the particles undergoing capture.

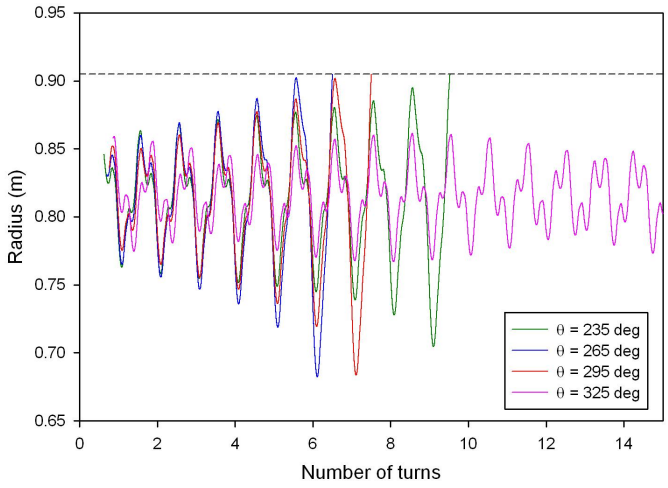

Figure 4.9: *Particle tracks after capture a different azimuths, at an energy of 16.74 MeV/amu for* $^{129}Xe^{26+}$

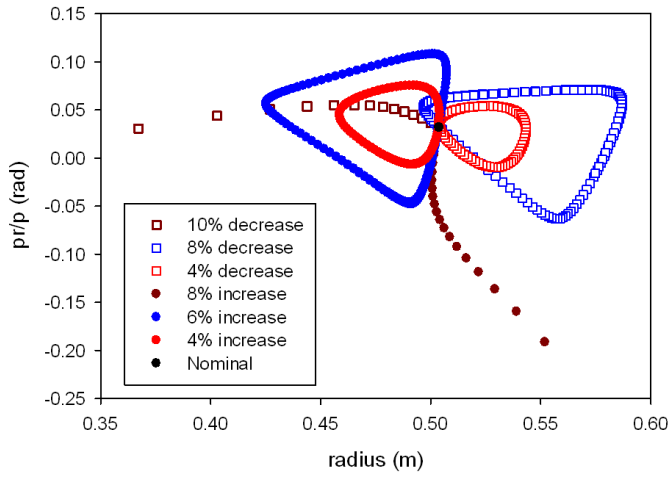

Figure 4.10: *Phase diagram of particles at the azimuth of charge exchange (215°), at an an energy of 5.8 MeV/amu for* $^{129}Xe^{26+}$ *for different charge state change*

4.5 Parameters of impact

Once we have the trajectory of particles hitting the walls we can estimate the impact parameters. This is input into experiments which give an idea of the desorption process which these particles fuel. We limit ourselves to the particles lost in the outer most radii. The contribution to desorption from the other particles is small, for reasons discussed below:

- The capture cross-section roughly scales with $\frac{1}{v^2}$, where v is the velocity of the ion. The pathlength and the turn density both scale with v. Using equation 3.5 we conclude that the loss per cm radially is uniform throughout the machine. The stripping cross-section is dominant over capture at larger radii. The losses at large radius will thus be greater than the losses in the interior.

- To first order the desorption yield scales with the total energy deposited on the surface. In the first couple of turns where particle energy is low, we expect a low desorption yield for these particles.

- Particles being lost halfway in the acceleration process (between an average radius of 0.3 m to 0.6 m), can hit either the inner posts or the outer vacuum chamber walls depending on the radius of charge exchange. The trajectory of these particles is near circular with a small radius of curvature as shown in figure 4.11. From the figure, we observe that stripping by a couple of electrons does not lead to the particle orbit to become unstable. If the Xe^{26+} loses 5 electrons or more, it spirals outwards and will hit the inner posts before reaching the outer radius of the cyclotron.
  The impact of these particles hitting the walls can be described with a simple geometrical picture. For the interior particles it is similar to the intersecting circles with a large difference of radius. For particles lost near extraction it is similar to intersecting circles with nearly the same radii. The angle of incidence of particles (w.r.t the surface) lost in the interior is thus on average much larger than for particles lost in the outer radii. Experiments [15] show that the desorption yield for large impact angles is lower than the yield for small impact angles, indicating that the contribution to desorption for these particles would be small.

For the large radii we looked at two aspects, namely the distribution of the points of impact and the angle of incidence on impact.

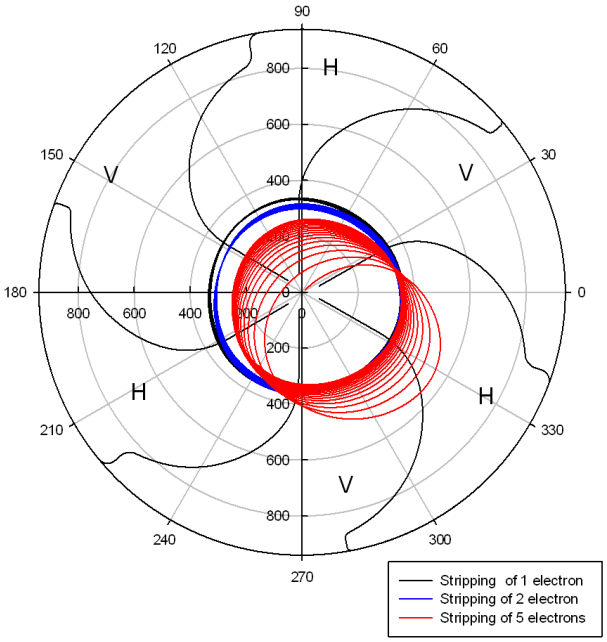

Figure 4.11: *Track of beam particles at an energy of 2.7 MeV/amu for $^{129}Xe^{26+}$ after stripping (1, 2 and 5 electrons)*

4.5.1 Point of impact

The points of impact of the particles on the perimeter walls are calculated in the simulation as the azimuthal coordinate where r crosses the boundary at a radius of 905 mm. Their distribution gives us information on the presence of possible hot spots along the boundary wall. In figure 4.12, the impact points after charge exchange are plotted (with an energy of 17.46 MeV/amu). The black points indicate the locations for a single sector where a charge exchange has occurred, in the r,θ plane. The red points indicate the points of impact after stripping and the blue points indicate the impact points after capture. The impact points are displayed for a single sector along the perimeter. For the stripping the particles are mainly lost in the hill sector, where the closed orbit is farthest away from the center. For the capture the picture is less evident, but we do observe a concentration in the hill sectors for the impact points.

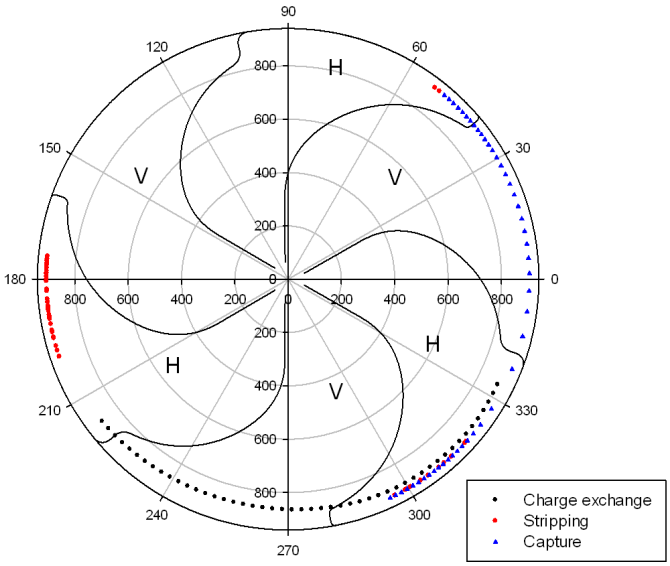

Figure 4.12: *Points of impact on the perimeter wall post capture at an energy of 17.46 MeV/amu for* $^{129}Xe^{26+}$

4.5.2 Angle of incidence

The impact angle of the charge exchanged particles is revelant for our desorption studies. Previous work done [15] shows significant difference for desorption yields at perpendicular and shallow angle of incidence. The simulations calculate the angle of incidence from the p_θ co-ordinate of the particle at the point of crossing the boundary. For the outer most orbits, a charge-exchanged particle hits the perimeter walls at a small angle of incidence. Figure 4.13 plots the angle of incidence for different azimuths where capture and stripping has occurred. The angle of incidence varies between 0° and 5°. For the particles lost from orbits near the extraction radius the distribution of angles of impact is shown in figure 4.14. This kind of shallow incidence is expected as the intersection angle between two circles with nearly the same radius is small.

4.6 Results

We simulated the particle tracks after charge exchange for $^{129}Xe^{26+}$ and looked at the impact parameters which we consider to be relevant for desorption yield. These

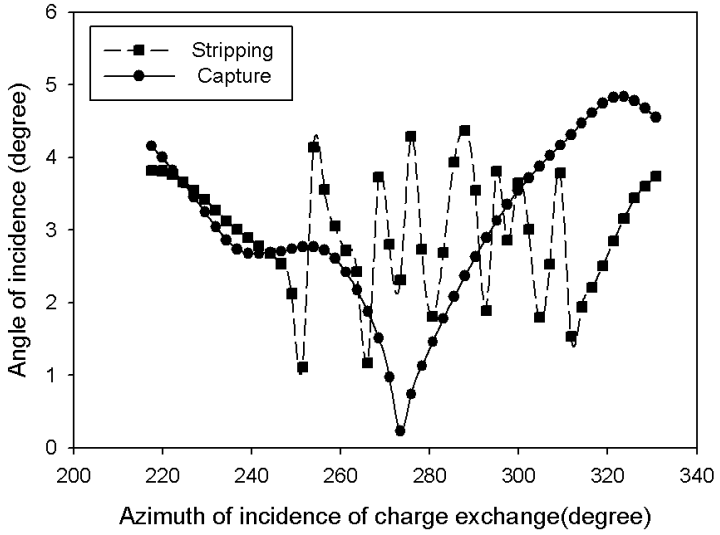

Figure 4.13: *Angle of incidence after capture of an electron for closed orbit at an energy of 17.46 MeV/amu for* $^{129}Xe^{26+}$

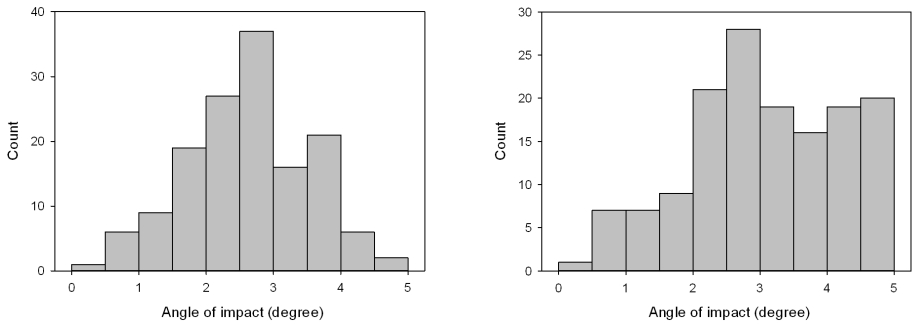

Figure 4.14: *Angle of incidence after capture and stripping for near extraction energies for* $^{129}Xe^{26+}$

results can be applied to any beam with roughly the same properties (energy and charge over mass ratio), independent of the charge state. Based on the simulations we can summarize the following about particles undergoing charge changing collisions.

- A single charge exchange generally does not lead to the particles hitting the outer walls of the machine. Most of the particles continue to precess in an off-centered stable orbit and have to undergo multiple charge exchanges before their track becomes unstable. Only particles with energies near the extraction energy of the beam end up on the walls post a single charge exchange.
- At outer radii the lost particles hit the walls at a shallow angle of incidence between 0° - 5°
- The particles lost at inner radii have a low energy and the angle of incidence has a much broader distribution due to the complex geometry of the center, reducing their contribution to the overall desorption.

Chapter 5

Models for desorption yield

5.1 Introduction

We investigate the desorption induced by the impact of an energetic projectile on a surface for different beams and targets. Empirical models are available, which predict the desorption yields from the energy deposition at the surface and along the particle track into the material. In this chapter we introduce these existing models, which we will use to interpret our observed results. We discuss the basic principles of these models of ion-induced desorption, and their dependence on the stopping power. We also examine the conditions to determine whether these models are suited to interpret our experimental observations.

5.2 Models for desorption

The existing models describe the desorption yields of fast ions incident on various surfaces, especially biomolecules, both for the keV and the MeV range. In the cyclotron we have MeV/amu ions incident on conductors which is rather high as compared to the situation for which the models were developed. We want to investigate the applicability of these models for our case and for that we examine each model independently.
These models treat desorption as an effect of energy deposition in the target material along the track of the fast projectile [47]. The energy deposited in the material leads to an excess of energy in the excited solid, which is dissipated by the molecules either directly exciting them or, as in the case of MeV projectiles, through secondary electrons. These excitations lead to the breaking of bonds, both ionic and van der Waals, resulting in desorption. Based on the excitation processes we have looked closely at two models that have been used in our energy range :

- Thermal spike model [48]
- Shock wave model [49]

5.3 Thermal spike model

This model, based on thermal considerations, may be appropriate for our observations, because it can be applied to high energy particles on conducting surfaces [29]. After the ion impacts perpendicularly on the surface, energy is deposited initially within a very small volume. This leads to a rise in temperature in this enclosed volume, which gives a characteristic thermal spike. A schematic diagram of the thermal spike model is shown in figure 5.1a, where the beam particle is incident perpendicular to the surface. The inner cylindrical core denotes the volume where the thermal spike is generated, while the outer cylinder denotes the expanding volume where the spike dissipates its energy. The radius of the inner core corresponds to the Bohr adiabatic radius [48], which is about 6 nm for the cases we consider. Once created,

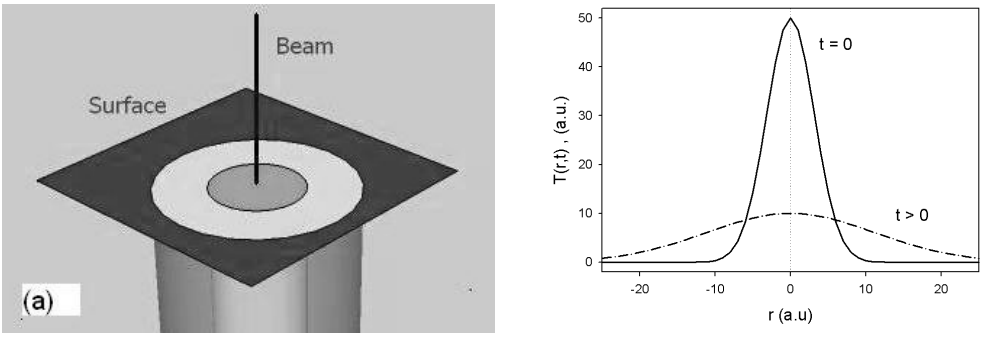

Figure 5.1: *The thermal spike model (a) Schematic diagram (b) Gaussian representation of the thermal spike, evolving with time*

the thermal spike spreads in time over the entire volume as indicated in figure 5.1b. The system can be considered to be one-dimensional since the track length is very long compared to the track radius, the stopping power (energy deposited per track length) does not change significantly over the track diameter and the distribution is azimuthally symmetric. In the figure both the temperature $T(r,t)$ and the radius (r) are represented in arbitrary units. The initial shape of the thermal spike is represented by the $t = 0$ solid curve. This spike spreads with time as a Gaussian, whose peak temperature decreases with time and the width increases as indicated by the dashed curve in the figure.
The temperature distribution can be calculated using the heat diffusion equation

$$\frac{\partial T(r,t)}{\partial t} - \frac{\lambda}{C_p \rho} \nabla^2 T(r,t) = 0 \tag{5.1}$$

where λ is the heat conductivity, C_p is the heat capacity, and ρ is the density of the material. We consider that heat is deposited at time $t = 0$ and assume that the heat diffusion is azimuthally symmetric. We can then rewrite the heat diffusion equation in a cylindrical co-ordinate system as

$$\frac{\partial T(r,t)}{\partial t} - \frac{\lambda}{C_p}\frac{1}{r}\frac{\partial}{\partial r}\left(r\frac{\partial}{\partial r}T(r,t)\right) = 0 \tag{5.2}$$

The solution to equation 5.2 as shown in [50] and [48] is given by

$$T(r,t) = \frac{T_0}{\nu(t)^2}\exp\left[-\left(\frac{r}{r_0\nu(t)}\right)^2\right] \tag{5.3}$$

where r is the direction perpendicular to the ion track and t is time elapsed since the ion has deposited its energy. The parameter $\nu(t)$ gives the change in radial width as a function of time.

$$(\nu(t)r_0)^2 = r_0^2 + 4\alpha t \tag{5.4}$$

$$\alpha = \frac{\lambda}{C_p\rho} \tag{5.5}$$

The initial thermal spike is enclosed in a cylinder with radius r_0 (indicated by the inner cylinder in figure 5.1) and has an initial surface temperature T_0. The surface temperature is related to the electronic stopping power $\left(\frac{dE}{dx}\right)_e$ [47].

$$T_0 = \frac{1}{\rho C_v \pi r_0^2}\left(\frac{dE}{dx}\right)_e \tag{5.6}$$

Here $\left(\frac{dE}{dx}\right)_e$ is the electronic stopping power on incidence and C_v is the heat capacity at constant volume.
A general expression for the desorption yield from the surface is given by the position and time integral of the surface evaporation rate $\Phi[T(r,t)]$ ([51], [29], [47]).

$$Y = \int_0^\infty dt \int_0^\infty \Phi[T(r,t)]2\pi r dr \tag{5.7}$$

The surface evaporation rate in 5.7 is given by calculating the flux of an ideal gas evaporating from a surface using the Maxwell-Boltzmann law

$$\Phi = n_M\sqrt{\frac{k_B T(r,t)}{2\pi M}}\exp\left(-\frac{U_A}{k_B T(r,t)}\right) \tag{5.8}$$

where U_A is the enthalpy of adsorption of a desorbed molecule, n_M is the molecule density, M the molecular mass and k_B is Boltzmann constant. The desorption yield is dependent on the surface temperature distribution only. It is assumed that there is no heat diffusion into the bulk which implies that the energy deposition is independent of depth at the relevant length scale. Existing literature [48] states that the desorption yield scales with the square of the stopping power. This scaling law has also been observed in calculated desorption yields [29] and experimental results for high energy heavy ions with perpendicular incidence [52].
The thermal spike model is limited to surface effects only. The initial cylindrical core has a radius in the range of about 6 nm for the cases we consider.. The depth of the Bragg peak for the $^{40}Ar^{5+}$ at 8 MeV/amu on copper is about 35 μm. The large difference in the two length scales,is used as the justification to consider the system to be one-dimensional and to neglect the contribution from the deep-lying Bragg peak to the surface temperature distribution.
However, when the particle is incident at an shallow angle (eg. 2°) the Bragg peak is located at a depth of 1.2 μm for the same Ar beam. Therefore the energy deposit along the whole particle trajectory, including the Bragg peak, may contribute to the surface heating and the desorption. To assess the contribution of the Bragg peak we looked at another model, i.e. the shock wave model, which gives an expression for the desorption yield when the energy is deposited at a certain depth below the surface.

5.4 Shock wave model

The shockwave model was developed to explain cluster emission in the sputtering of solids by ion beams [49] mostly in the keV energy range. The model is used for inorganic compounds and biomolecules. This model explains desorption from a single point source of energy just below the surface, which we feel is similar to the effect of the Bragg peak at a small angle of incidence.
As a fast heavy ion passes through a material, the deposited energy creates an energy spike. This high energy density leads to the creation of a shock wave which originates along the track and dissipates radially. The energy density deposited in the cylinder around the particle track is denoted by W_c. The shock wave propagates outwards radially from the central core with radius R_c as shown in figure 5.2. The internal energy per particle behind the shock wave front ($W(R)$) at a distance R from the center is given by equation 5.9 [49]

$$W(R) = \frac{W_c \left(\frac{R_c}{R}\right)^2}{1 - B + B(\frac{R}{R_c})^{1/2}} \tag{5.9}$$

where $B = \frac{16}{3}(2W_c/C)^{1/2}$ and $C = 1/(Kn)$, K is the compressibility of the solid and n is the atomic density of the material behind the shockwave front.
The boundary of the propagating shock wave, i.e. the largest radius at which ejection can take place is given by R_s, such that the following criterion is met for ejection:

$$W(R_s)cos^2\theta = U \tag{5.10}$$

In equation 5.10 U is the surface binding energy of the target molecules [53] and θ is the angle as shown in figure 5.2. The total number of particles ejected per unit track

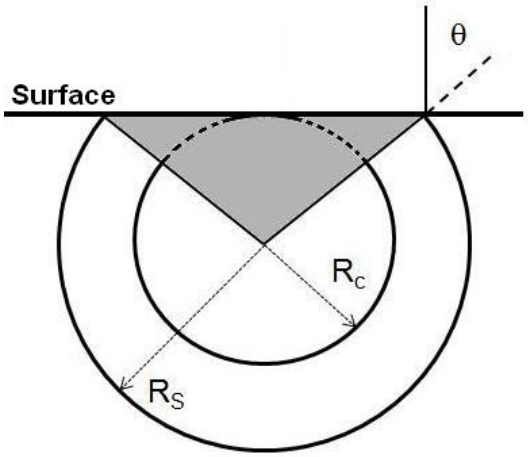

Figure 5.2: *Schematic diagram of the shockwave model for a vertical cross-section along the particle trajectory at a certain depth R_c. The beam particle goes through the center of the circles, i.e. its direction is nearly perpendicular the plane of the paper.*

length is proportional to the volume of the shaded region in figure 5.2, which is the cone from the axis of the shock wave to the boundary. The desorption yield is then proportional to the integral

$$Y = \int s^2 sin^2(\phi(s)) tan(\theta(s)) ds \tag{5.11}$$

$$tan(\theta(s)) = \frac{R_s}{s\ sin(\phi(s))} \tag{5.12}$$

where ϕ is the angle of incidence of the beam and s is the parameter denoting the track length of the beam particle trajectory. The angle θ varies along the particle track and is determined by the stopping power and depth below the surface of the track. The critical energy per atom W_c is of the order of 15 eV [49].
The stopping power of Ar is at most 12 keV/nm and this energy deposit is shared over the roughly 2400 Cu atoms/nm path length that lie within the Bohr adiabatic radius. The corresponding energy density is 5 eV per atom, which is below the critical energy density so that we do not expect the shock wave mechanism to contribute for Ar.
For Pb the stopping amounts to about 60 keV/nm in the initial part of the particle track, corresponding to an energy density of 25 eV/atom. This value is above the critical energy, therefore the shockwave mechanism may contribute to the desorption yield for Pb. Assuming the surface binding energy U to be around 1 eV this contribution is limited to the initial 0.5 μm of the particle track.

5.5 Conclusion

The thermal spike model has been developed for perpendicular incidence and therefore only covers the effects around the entrance point of the incident ion. At small angles of incidence the whole particle trajectory is at a shallow depth and may contribute to the desorption yield. We investigated whether the shock wave mechanism [49] could contribute to the desorption caused by the energy deposition along the particle trajectory in the bulk. We conclude that shockwave formation can contribute to desorption only over a very small fraction of the particle trajectory close to the entrance point for the heaviest projectiles, Xe and Pb.
The energy deposited along the particle track also leads to a local temperature increase of the surface through heat diffusion, similar to the thermal spike mechanism, that leads to increased outgassing. Along the particle trajectory a temperature transient propagates to the surface above the trajectory and consequently increased outgassing will occur due to the diffusion of the deposited energy. The timescale of this transient is about 1 ns.

Chapter 6

Desorption experiment: Setup and procedure

6.1 Introduction

In this chapter we discuss the experimental setup developed for the measurement of heavy ion induced desorption. After a charge changing collision, beam particles hit the walls of the cyclotron desorbing molecules from the surface material. Orbit calculations (as shown in the chapter 4) indicate that particles with the highest energies continue on a trajectory, intersecting the walls of the cyclotron at a shallow angle of incidence, between 1° and 8°. In order to get a better insight in the desorption induced by these particles in the cyclotron, quantitative measurements of desorption yields for various materials and ions under well controlled conditions are required. In this chapter we give an overview of the setup developed for these measurements. The choices for the beams, targets and the specifics of sample preparation and relevant cleaning procedures are discussed. We present the measurement procedure including calibration of pressure and steps taken to estimate the background pressure in the measurements. Finally the procedure used to calculate the desorption yield from the corresponding pressure rise is described.

6.2 Setup overview

A schematic view of the setup is displayed in figure 6.1. The main chamber is a six arm conflat (CF) crosspiece 150 mm in diameter. A beam position monitor (BPM) is attached to one port. It consists of a metal plate coated with scintillating material ZnS and is movable with the help of bellows. When the BPM is completely in, its center is located at the center of the chamber.
A turbo molecular pump unit (TMP) with a nominal pumping speed of 230 liter/s for nitrogen [54] is attached to a second port on the main chamber. A wide range vacuum gauge (Edwards WRG-S-DN40CF) is also attached to the main chamber, recording the pressure at all times. A section valve separating the main chamber and the target chamber, was implemented to vent only the target chamber thereby reducing the time taken to pump down the setup during a sample change.

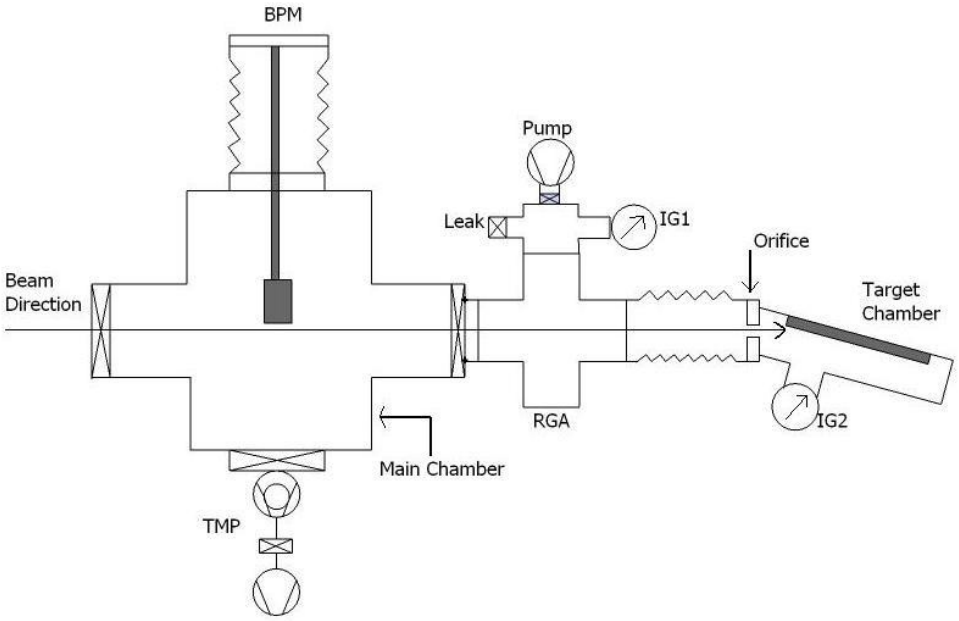

Figure 6.1: *Experimental setup schematics as seen in top view*

In front of the target chamber we have a conflat cross piece 64 mm in diameter as shown in Figure 6.1 to which the diagnostic equipment for the experiment is attached. On the other two ports we attach:

- A Rest Gas Analyzer (RGA-MKS, Microvision Plus) to determine the species dependent pressure rise
- On the other flange there is a cross piece (CF35) equipped with an ionization gauge (UHV nude gauge, Bayard-Alpert, Granville-Phillips 274) and a needle valve to vent the chamber for target changes. A roughing pump for the initial pump down after a sample change is attached to the remaining port.

A custom made 64 mm diameter bellow connects the actual target chamber to the second cross piece. The bellow allows the target chamber to rotate over an angular range of $\pm 4^\circ$ with respect to the beam axis. The target chamber itself is welded to a flange at an angle of 4 °, such that the target surface can rotate from 0° to 8° with respect to the beam axis. A second ionization gauge (UHV nude gauge, Bayard-Alpert

Granville-Phillips 274) is attached to the target chamber to record its pressure.

6.3 Pumping unit and pumping speed

The pressure in the cyclotron during acceleration of heavy ion beams is about 3 $\times$ 10^{-7} mbar. Beam induced deterioration results in a a pressure of around 10^{-6} mbar in extreme cases. To mimic these operating conditions the experimental setup is pumped down to a pressure of about 2 $\times$ 10^{-7} mbar in the target chamber. The pump is attached to the main chamber (figure 6.1) and the target chamber is pumped out via the bellows. Because of the complex shape of the setup the effective pumping speed in the target chamber was determined experimentally for helium using an adjustable leak and a helium leak detector. Pumping speeds for other rest gas species were then derived from the value for helium.

6.3.1 Determination of pumping speed of the setup

Helium was leaked into the target chamber through a fixed standard leak (10^{-6} mbar liter/s at 1 bar) from a reservoir at variable pressure. The pressure in the setup was monitored by the rest gas analyzer while a helium leak detector was attached at the end of the turbo pump to measure the helium gas flow rate. The pressure of the RGA and the flow rate of the leak detector was measured once the system had stabilized. The pumping speed at the location of the RGA was determined by the following equation [55]

$$S = \frac{Q}{P} \tag{6.1}$$

where Q is the gas load flow rate in mbar liter/sec, P is the local pressure and S is the pumping speed at equilibrium. Figure 6.2 shows the dependence of the measured flow rate with the pressure as measured with the RGA. The measurements were corrected for the sensitivity of the RGA for the different gases [56]. From the slope in the figure, the effective pumping speed for helium at the location of the RGA was determined to be 148 $\pm$ 5 liter/sec.
The nominal pumping speed for He of the turbo molecular pump is 240 liters/sec [54]. The conductance between the pump and the RGA, C, is then given by equation 6.2, where S_P is the pumping speed of the turbo pump and S is the pumping speed at the RGA.

$$\frac{1}{S} = \frac{1}{C} + \frac{1}{S_P} \tag{6.2}$$

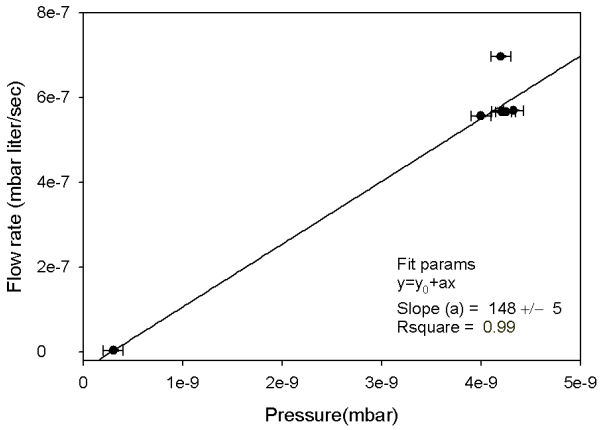

Figure 6.2: *Estimation of pumping speed in the setup for helium*

To find the pumping speed at the RGA for other gases equation 6.2 is used . From the conductance C of He, we calculate the conductance for other gases. In the molecular flow regime the conductance C for different gases is proportional to the ratio of the inverse of the square root of masses of the gases.

$$C \propto \sqrt{M}^{-1} \tag{6.3}$$

Finally we recombine the conductance and the pumping speed at the turbo pump for the specific gas species to calculate the pumping speed at the RGA. The pumping speed of the pump for different gases is listed in [54] and the dependence on molecular weight is shown in [57].

Rest gas species	S_P(liters/sec)	C (liters/sec)	S (liters/sec)
He	240	386 ± 34	148 ± 5 (measured)
CO/N_2	230	146 ± 12	89 ± 4 (calculated)
CO_2	210	116 ± 10	75 ± 4 (calculated)
H_2O	235	182 ± 16	102 ± 5 (calculated)

Table 6.1: *Effective conductances and pumping speeds for different rest gas species*

6.4 Beam alignment

The alignment of the setup with the beam line axis is a critical factor in minimizing the systematic errors in the angle changing mechanism. A good angular precision provides reproducibility for our experiments and also ensures that the beam only hits the desired target area. The setup was positioned such that the beam line axis passed through the center of the setup, both horizontally and vertically, as shown in figure 6.3. We also ensured that the center of the BPM coincides with the center of the main chamber and thus lies on the beam line axis.

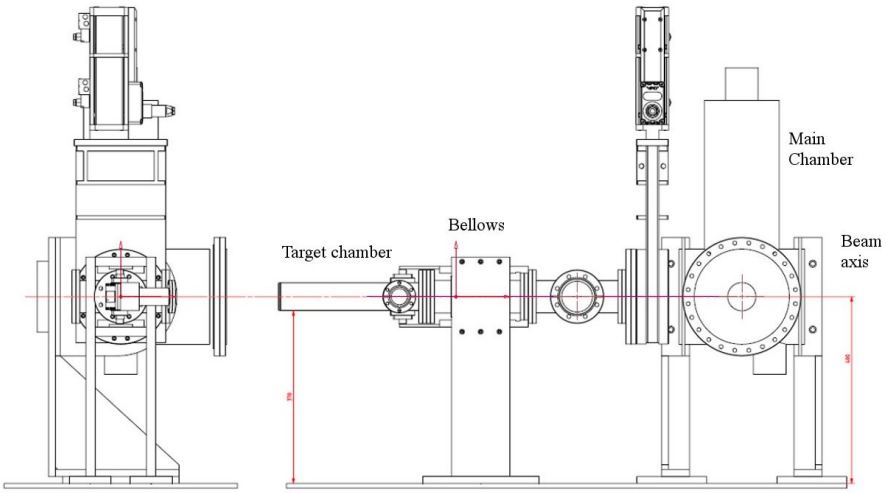

Figure 6.3: *Schematic diagram of the setup and beam axis*

6.4.1 Beam alignment

In the setup, we use the beam position monitor in the main chamber for the preliminary beam alignment as the last harps (diagnostic equipment used to verify if the beam is centered along the beam axis) are 1.5 m upstream from the target. Upstream in the beam line, an aligned telescopic viewer and an infrared camera are located, as indicated in figure 6.4. The beam spot is displayed on a monitor in the control room. By manipulating the bending magnets B4 and B5 and the 2D steering magnet in front of B5 (figure 6.4) we adjust the position of the beam in transverse phase

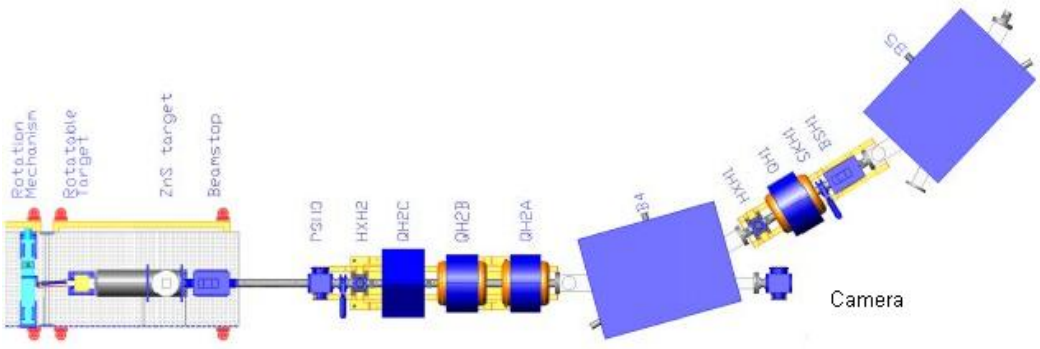

Figure 6.4: *Overview of the set along with components of the high energy beam line*

space such that it follows the axis of the beam line. The two quadrupoles QH2A and QH2C are used to verify the beam alignment and get the smallest possible spot size on the BPM.

6.5 Target chamber

The target chamber is a pill box with dimensions 300 mm $\times$ 56 mm $\times$ 30 mm. It is made of stainless steel and has an opening of 260 mm $\times$ 30 mm on one side where a replaceable target lid can be attached. The target chamber is welded to the flange connecting to the bellows at 4° as shown in figure 6.5. On the opposite side of the lid, a CF30 stem has been attached to mount the ionization gauge measuring the pressure in the target chamber. The target lid has a small block protruding 23 mm on one side as shown in the figure. This block has a 250 mm $\times$ 25 mm surface which is the target surface. For a beam with 4mm diameter incident at an angle of 1°, the spotsize generated has a length of 230 mm, which is thus the minimum required length of the target surface. Based on our orbit calculations, we are interested in small angles of incidence between 0° and 8°, which can be achieved by the custom made bellows. Figure 6.6 shows the target chamber layout for the zero degree position. The point of rotation lies on the point (as shown in the figure) joining the bellows to the target chamber. When the target is at 0°, the beam does not hit the surface since the beam has an average radius of 2 mm and the beam axis is 2 mm above the target surface. We have made this design choice to fix one end of the

beamspot (where the near edge of the beam profile intersects the target surface, figure 6.7) as our point of rotation. When the angle of incidence changes that particular end of the spot remains unchanged while the area of the spotsize changes. This design choice reduces the length of the target surface required for our angular range and reduces the arm for the range of motion of the bellows.

6.5.1 Adjusting the angle of incidence

Using the BPM we ensure that the beam passes through the center of the main vacuum chamber. The next step in the alignment process is adjusting the target chamber to ensure that the beam does not spill over the target surface on to the chamber walls. If the beam hits the side walls of the target chamber, the desorption measurements will be biased. The target chamber is fixed in the 4° position and a viewing target is mounted on the target chamber. A schematic diagram of the target chamber at 4° and the span of the beam spot on the target is shown in figure 6.7. The viewing target is an aluminum piece with a perspex slab glued to the frame on the target surface side. The inner side of this slab is coated with the scintillating material BaF_2. We chose BaF_2 over ZnS since it was easier to coat a homogeneous layer of BaF_2 on to a perspex surface. When the beam is incident on the target surface, it will generate a spot, which we observe with the help of a CCD camera.

The image from the CCD camera is used to check two conditions.

- The beam is confined to the target surface and does not hit any other parts of the target chamber.
- The beam spot for all angles does not move along the target surface laterally , and the upstream edge of the beam spot, which coincides with the point of

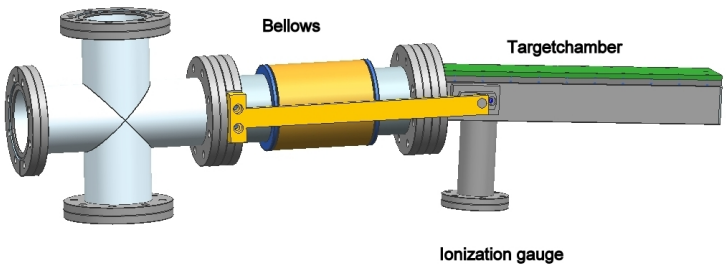

Figure 6.5: *Topview(schematic) of bellow attached to the target chamber*

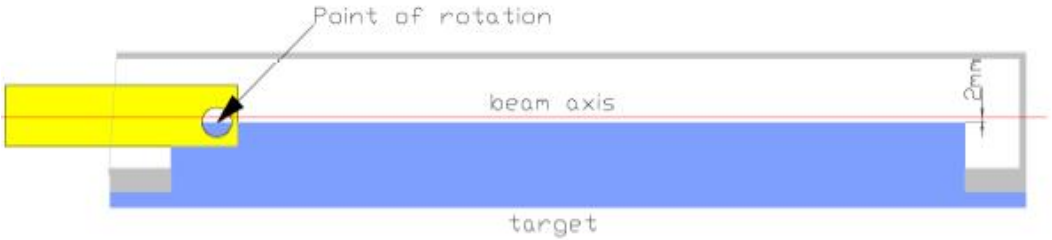

Figure 6.6: *Layout of the target chamber (topview) and the beam axis at zero degree position*

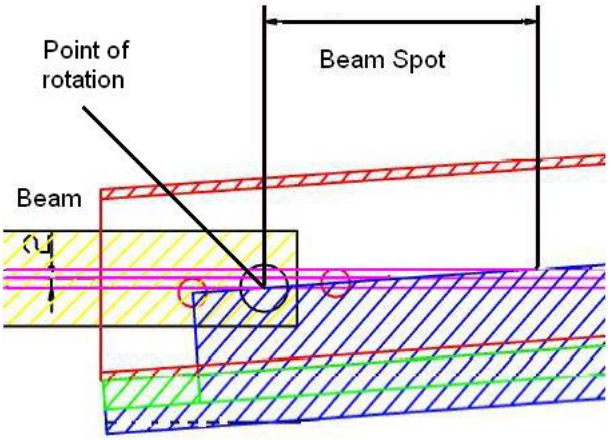

Figure 6.7: *Alignment of target surface at 4°. The parallel lines indicate the beam with a radius of 2mm*

rotation, is independent of the rotation angle of the target.

- The length of the beam spot scales with the angle of incidence.

We measure the spot size by taking a horizontal cross cut at the center of the spot profile (as shown by the dotted line in figure 6.8) at different angles.The cross cut gives a profile which can be fitted well with a Gaussian (figure 6.9). The width of the Gaussian fit, scales with the inverse of angle of incidence. This implies that the area where the beam is incident on the surface scales with the angle, as expected. We also observe from the figure that the start (right edge) of the Gaussian distribution is the same for all angles of incidence. This verifies that the beam passes through

Figure 6.8: *Beam spot as observed by the CCD camera, at an angle of 1 degree*

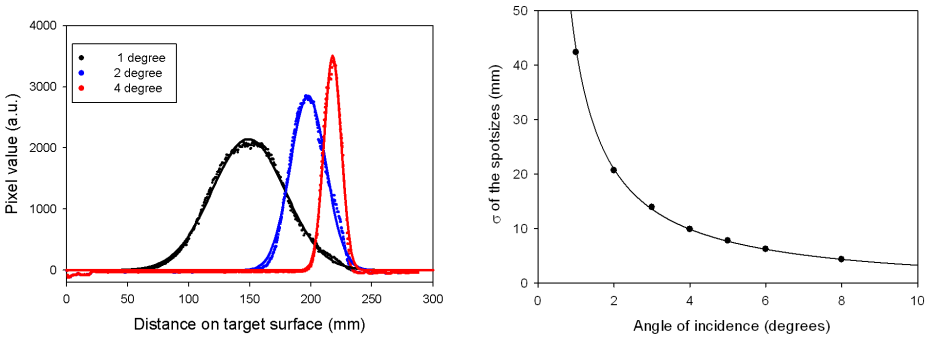

Gaussian fits of spot sizes σ of the Gaussian fits

Figure 6.9: *Gaussian fits and corresponding σ of spot sizes at various angles of incidence*

the point of rotation (see figure 6.6) of the target chamber.

6.6 Angle changing procedure

During early trials of the experiment, the target chamber was rotated by moving the end of the target chamber with a vertical post and screw setup (see figure 6.10). The chamber was positioned after calculating the distance from the vertical posts for the corresponding angle from design diagrams (as shown by the red line in figure 6.10). To change the angle of the target chamber we rotated the screws, and we verified the distance with the help of calipers. However this method of changing the angle was modified for the following reasons.

- The reproducibility of this method was limited by errors in measuring the distance of the screws with the calipers. The error associated with initial positioning at the end of the chamber was about 1 mm which translated to an angular error of 0.2°.

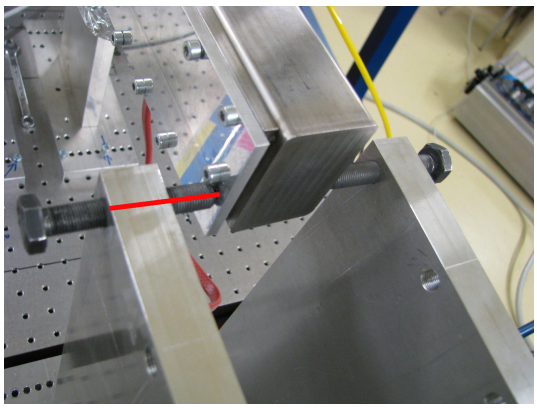

Figure 6.10: *Screws attached to vertical posts to fix the angle of incidence*

- Changing angles was time consuming. For every single measurement the angle had to be changed manually, which took us around 15 to 20 minutes.

To resolve these issues an angle changing mechanism with improved accuracy and reproducibility was constructed. The target chamber had a new cylindrical extension welded at its end, which can be attached to a remotely controlled calibrated positioning device (XY table). The extension rests on the support of the XY table fixing the vertical height and improving the vertical alignment. The XY table moves along the horizontal X axis and shifts the cylindrical extension. This mechanism keeps the system moving in the X and Z directions and allows rotation about the turning point. The positioning of the target chamber with the help of the XY table is reproducible to within 0.1 mm which leads to a corresponding $\Delta\theta$ of 0.02° (1° angular displacement corresponds to 4.63 mm lateral displacement at the end of the target chamber). It also considerably reduced the delay between subsequent measurements (described in 6.9) and allowed us to use beam time more efficiently.

6.7 Beams

The experiment has been designed to quantify desorption induced by heavy ions hitting the walls of the cyclotron. For our measurements we have used beams with the charge over mass ratio and final extraction energy as given in the table 6.2. The motivation to use different beams was to investigate any atomic number (Z) dependence of the desorption yield and interpolate any observed dependence to predict desorption yields for other heavy ions.

Beams	$\frac{q}{A}$	Extracted Energy (MeV/amu)
$^{16}O^{2+}$	0.125	8.0
$^{40}Ar^{5+}$	0.125	8.0
$^{84}Kr^{11+}$	0.130	8.14
$^{129}Xe^{16+}$	0.125	8.0
$^{206}Pb^{27+}$	0.131	8.5

Table 6.2: *Beams used for desorption experiment*

Previous studies investigate a dependence on the electronic stopping power ($\frac{dE}{dx}$) by varying the energy of the beam incident on the target [30]. In our case changing beam energy without complete retuning of cyclotron and injection system is impossible. Therefore we have used different beams (with nearly the same charge over mass ratio) to vary the stopping power and analyze its effect on the desorption yield.

6.8 Targets

For the targets we have concentrated on materials present in the cyclotron vacuum chamber: copper, aluminum and stainless steel. All the targets were made by machining solid blocks of materials. This has the following benefits.

- Thermal: Heat conduction would be uniform all over the target material
- Vacuum: No unnecessary air pockets due to removable parts, ensuring a faster pumpdown.
- Tolerances: Machining ensures that the surfaces at a constant height.

All the target surfaces have been machined with a roughness parameter of around Ra 0.8 [58] which is also the specification for the relevant surfaces in the cyclotron.
Some of the copper parts in the machine have not been cleaned since the commissioning of the machine since they are unreachable. These copper parts have developed an oxide layer on the surface. We therefore, also used a copper oxide target, which was made by oxidizing the surface of a copper block in a moisture rich environment for about a month.
Recent studies done at GSI [59] lead to the conclusion that gold plated copper has a significantly lower desorption yield than pure copper in a vacuum of 10^{-11} mbar. These results motivated us to apply a gold coating to parts of the peripheral walls of the cyclotron that are hit by charge exchanged particles and are readily accessible for the application of the coating. A similar gold coated target was also used in our

experiments. The coating consisted of an 0.5 μm nickel layer to prevent hydrogen diffusion covered with a 1 μm gold layer. Figure 6.11 shows the gold coated copper

Figure 6.11: *Gold coated copper target*

target after it has been irradiated in an experiment, the reddish patch in the middle of the target surface corresponds to the beam spot, suggesting that material has been eroded from the surface by the beam. Similar erosion however has not yet been seen in the interior of the machine.

6.8.1 Target cleaning

To prepare the targets for experiments the target surfaces were cleaned after machining. All target surfaces were first washed with a soap solution in an ultrasonic bath for 30 mins. For the copper targets a fresh soap solution was used every time and the contents of the bath were drained after this procedure. The targets were rinsed thoroughly in de-mineralized water. The target samples were then either baked in an oven at 200° C at a pressure of 10^{-2} mbars, for 20 mins or were blow dried with a heat gun for around 15 mins depending on the availability of the oven. After a final cleaning of the surfaces with alcohol, the samples were placed in a glove box with silica gel where the relative humidity is constant at 4 %. The cleaning procedure is aimed at removing grease or oil residues and fingerprints after machining the parts. Not much attention is given to removing the water layer adsorbed on the target surface as the RGA spectrum in the machine also shows that a lot of water is present in the cyclotron under operating conditions (pressure 4×10^{-7} mbar).

6.9 Desorption measurement

To quantify the desorption we measure the rise in pressure in the setup when the ion beam is incident on the target surface. A measurement continues until the pressure

reaches equilibrium. The rise in pressure is recorded by the two ionization gauges and the rest gas analyzer (RGA).

6.9.1 Ionization Gauges

The two ionization gauges factory calibrated for nitrogen over the range of 10^{-3} mbar to 10^{-11} mbar have been used. The pressure is read out from the gauge controller via an analog output. The readout is recorded in a PC using an analog to digital Measurement Computing DAQ system [60]. A calibration has been done to relate the actual pressure as shown in the gauge display to the voltage recorded by the ADC. The DAQ system has provisions to adjust the rate at which the data is recorded and stored. It has a fixed buffer memory of 30,000 samples per channel, limiting the timespan of a single uninterrupted data run depending on the recording rate. The measurements for the ionization gauges are stored in a file and are reviewed later for offline analysis. The ionization gauges record the total pressure in the target chamber and near the RGA as shown in figure 6.12. The pressure recorded in the first ionization gauge (IG1, see figure 6.1), near the RGA, is lower than second one (IG2), in the target chamber, because of the limited conductance of the bellows. Apart from measuring the pressure rise, the ionization gauge reading is used to verify the total pressure as measured by the RGA.

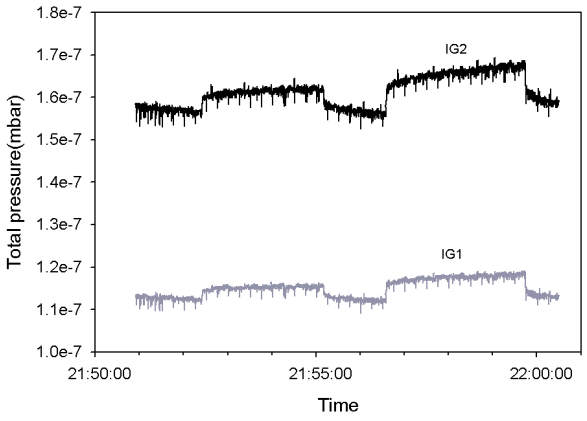

Figure 6.12: *Response of the two ionization gauges*

6.9.2 Rest Gas Analyzer

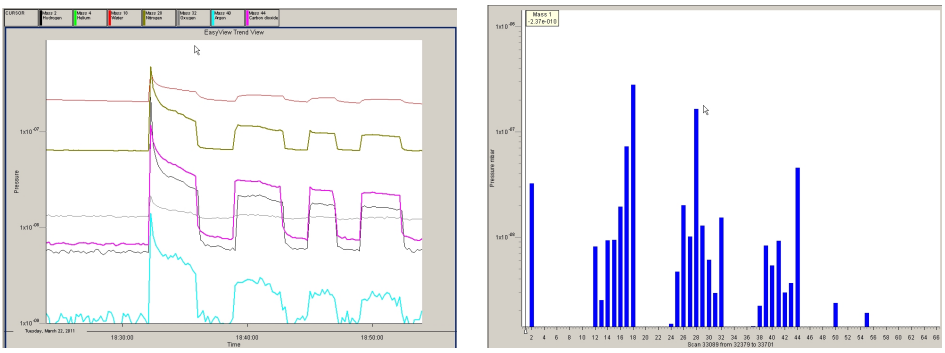

Time response RGA spectrum

Figure 6.13: *Screen shot of the RGA display during for* $^{40}Ar^{5+}$ *at 8 MeV/amu incident on the surface at 2°*

We use a MKS Microvision rest gas analyzer [61] which can measure the partial pressure up to mass 100 of the rest gas species. However we recorded only up to mass number 66, since most of the components we observe from desorption are below this mass limit. The RGA scans the set mass range with a specific frequency and records the pressure of each mass. In our case we have set the scanning time period to the maximum of 12 secs for the entire mass range. This ensures a greater accuracy of the recorded data. The RGA has a lower detection limit of around 10^{-11} mbar and has an external display showing data recorded in real time. We analyse the partial pressures of mass 18 (H_2O), mass 28 (CO/N_2), mass 32 (O_2) and mass 44 (CO_2) as these masses showed significant increase in pressure when the beam is switched on (figure 6.13).

6.10 Surface cleaning and measurement procedure

It was observed that upon the first incidence of the beam on the target a quasi-instantaneous increase in pressure occurred, as is illustrated by the ionization gauge profile displayed in figure 6.14. The sharp peak around time 21:46 hours shows this first response.

After a considerable irradiation time the sharp rise upon incidence of the beam disappears and a monotonous rise towards an equilibrium pressure is observed when switching on the beam. This observed pressure behavior can be explained by the considering two sources for desorption.

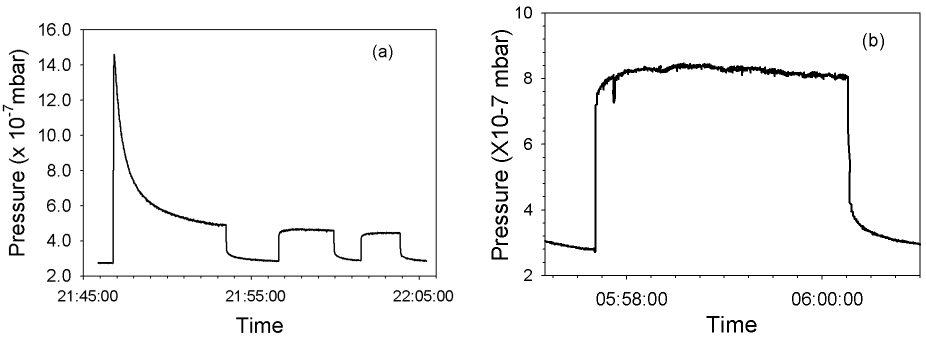

Figure 6.14: *Response of the beam incident on target surface as measured by the ionization gauge during (a) cleanup sequence and (b) single measurement*

- The loosely bound materials sticking on the surface as observed from the peak in figure 6.14. These molecules have a small reservoir and that can be depleted quickly by the ion beam incident on the target.

- The tightly bound surface material being desorbed. These molecules mostly have an infinite reservoir (within the period of the measurements, because the beam induced pressure increase varies only slightly with time) and are the main contributors to ion-induced desorption in the cyclotron, which occurs over extended periods of time.

To clean the sample of the loosely bound molecules, we position the target surface at the lowest angle (i.e. at 1°), such that the beam is incident on the complete target area that will be irradiated during the actual measurements. The beam intensity is set to the maximum achievable (normally around 200 nA - 300 nA). This gives a beam power of about 15 Watt incident on a target beam spot of 230 mm $\times$ 4 mm.The target is repeatedly irradiated for short periods until the pressure response does no longer exhibit a peak with subsequent decrease but instead monotonously increases towards an equilibrium value (see figure 6.14).
Figure 6.14 shows a typical pressure response during a single measurement. After the initial conditioning it was observed from the RGA response, that different rest gas species took different time spans to reach equilibrium, the maximum time being taken by mass 18 (H_2O). From the observations we estimated that a time of 3 minutes of beam on target ensures that all the rest gas species attain equilibrium. For a single sample, the desorption yield was measured for different beam intensities and different angles of incidence. We positioned the target at the lowest angle of incidence, and beam intensity on target was varied from 25 nA to 200 nA (or maximum

achievable for a particular beam) to probe the intensity dependence. The angle was then increased in 1° steps to 8° and then retraced back to 1°, to determine the angle dependent systematic effects, depending on the short term history of the sample.

6.11 Background subtraction and data analysis

A series of measurements done on a single target surface with a single beam gives us a pressure response as shown in figure 6.15. We are interested in measuring

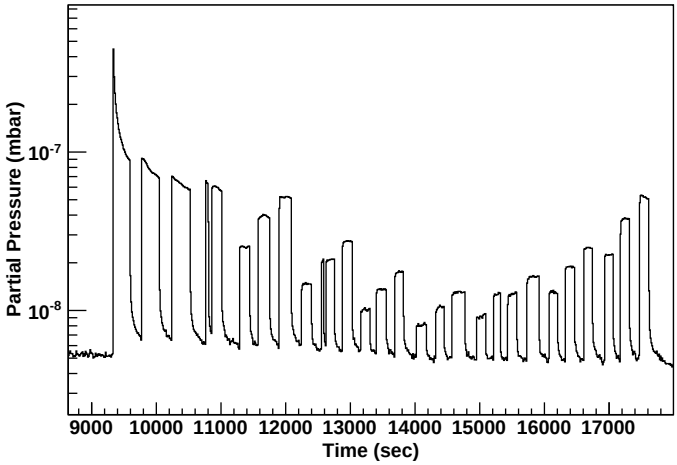

Figure 6.15: *Pressure response from RGA for mass 28 (CO/N_2), $^{129}Xe^{16+}$ on Aluminum target*

the rise of pressure due to beam on target. This requires the determination of the background or the baseline pressure. The pressure response includes two kinds of background.

- The steady slow pump down of the entire setup gives an exponential background. We calculate the time constant for the pump down by fitting the pump down curve from the RGA data as shown in figure 6.16. From that we extrapolate the background pressure and subtract it from the pressure response.
- After each incidence of beam on target, stopping the beam leads to a decrease in pressure. This decrease has two components: a fast decrease with a small time constant and a slow decrease with a larger time constant. It is possible

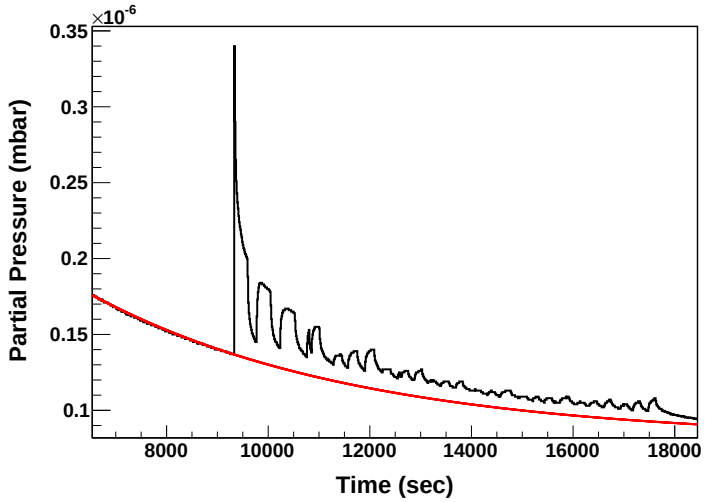

Figure 6.16: *Fit for initial pump down response from RGA data for mass 18 (H_2O) , $^{129}Xe^{16+}$ on Aluminum target*

to reach the initial pressure after a long time period, which we cannot afford due to a limited amount of beam time. Instead, we have the beam switched off till the pressure stabilizes enough to determine a base pressure. There is a tail from the previous measurement corresponding to the slow pump down component. We can fit this slow region, as shown by the interval between the two arrows, and then extrapolate and subtract from the subsequent measurement (as shown in figure 6.17a).

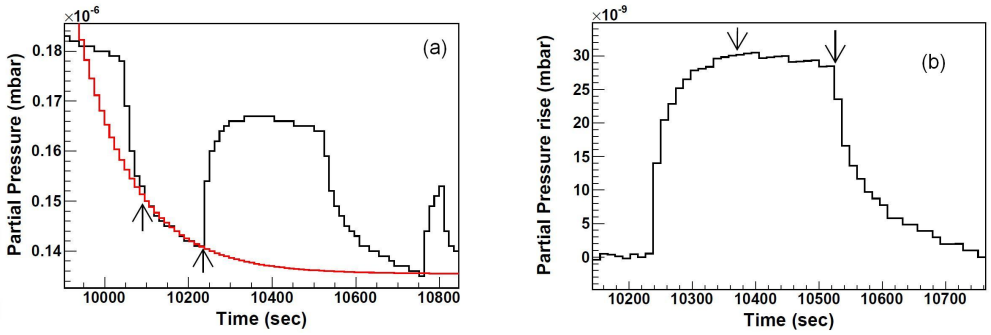

Figure 6.17: *(a)Fit for post-measurement tail and subsequent (b)pressure response after background reduction from RGA data for mass 18 , $^{129}Xe^{16+}$ on Aluminum target*

Once the backgrounds have been subtracted we get the response for a measurement as shown in figure 6.17b. For the increase in pressure we compute the average equilibrium pressure of the response, roughly being the average of the pressure value between the second minute and third minute while beam is on target as shown by the arrows in figure 6.17b. The statistical uncertainty is determined from the σ of the data points in that time range.
During the measurement sequence it was observed that at the same angle the pressure rise measured at different times is slightly different (figure 6.18). This difference

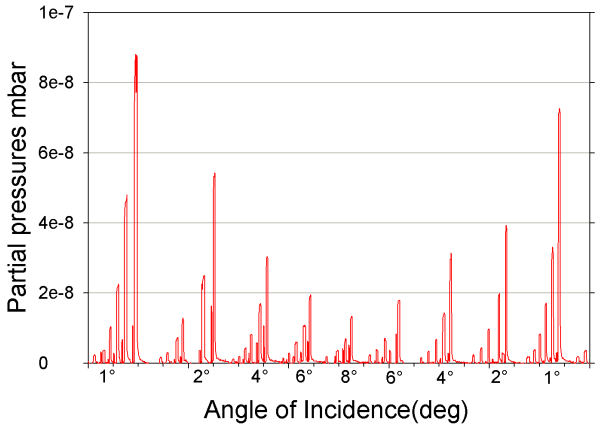

Figure 6.18: *Series of measurements taken at different angles and different beam intensities. RGA data for mass 28 , $^{40}Ar^{5+}$ on Copper target*

can be explained by the gradual cleaning of the target surface by the beam. When we proceed in the sequence from a lower angle to a higher angle not much beam has been incident on the target surface in the initial stages. While measuring the rise in pressure for an angle the second time, the surface condition of the target changes (depletion of the material on the surface) due to the additional amount of beam being dumped on the target. The pressure rise observed for the same angle is somewhat less for beam-on-target later, than earlier in the measurement sequence. The difference between the two measurements is calculated and is added in our estimation of errors.

6.12 Calculation of desorption yield

From the measured increase in pressure we extract a desorption yield using the pumping speed determined according to the procedure described in section 6.3.1.

The yield of a particular rest gas species can be determined by the conductance method [15] as shown.

$$\eta_{des} = \frac{\Delta P \times S}{\dot{N} \times k_B \times T} \tag{6.4}$$

where ΔP is the rise in partial pressure of the gas during ion bombardment on target, S is the pumping speed of the gas, $\dot{N}$ is the number of ions incident on target per second, k_B is Boltzmann constant and T the temperature (300 K). The rise in pressure is measured for different rest gas species by the rest gas analyzer and the pressure sensitivity of the different species is accounted for [56]. The flux of ions on target is measured by the Faraday cup at the exit (BSX) of the cyclotron. The high energy beam line has a pressure of around 10^{-7} mbars, so the difference in beam current from the measured value to the actual value incident on the setup would be limited to at most a few percent. We did not stop the beam and measure the current near the setup because the outgassing of the Faraday cup increased the base pressure in the setup.Using equation 6.4 we calculate the desorption yield as discussed in chapter 7.

Chapter 7

Desorption measurement: Results

7.1 Introduction

The previous chapter described the measurement procedure and methods to determine the beam induced pressure increase and how to calculate the desorption yield. The rise in pressure is dependent on various factors which affect desorption. In this chapter we investigate the dependence of the pressure increase for different rest gas species on various parameters such as beam intensity, angle of incidence and the stopping power.

7.2 Increase in pressure from the RGA spectrum

Our main experimental observations have come from the data of the rest gas analyzer measuring the partial pressure of the different desorbed gases. A typical response for a beam incident on target is shown in figure 7.1.

From the RGA partial pressure spectrum we observe the different base pressures for different rest gas masses. Even though the base pressure for mass 18 (H_2O) is higher than the other rest gas species, the relative pressure increase is smaller compared to mass 28 (CO) and mass 44 (CO_2). This different response of water might be due to the high sticking factor of water molecules as compared to the other rest gases. Figure 7.2 shows the response for water as compared to CO. When the beam is incident on target we have an instantaneous rise in pressure in both cases, which can be attributed to a direct effect of ion induced desorption. After the instantaneous rise there is a slow rising component suggesting that also a macroscopic process is involved, presumably related to heating of the whole sample. For water we observe that the time constant of the slow process much larger than for CO, while the absolute value of the pressure rise for H_2O is smaller than that for CO (figure 7.1). This may come from the presence of additional sinks in the setup (possibly sticking of H_2O to the walls of the setup, especially the bellows) which would reduce the number of water molecules reaching the RGA and give a lower absolute value for water. Another observation from figure 7.1 is the absence of partial pressure response for

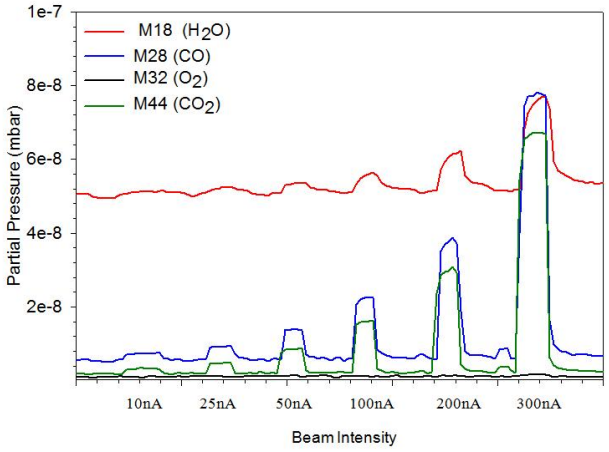

Figure 7.1: *Increase in pressure measured by RGA for $^{40}Ar^{5+}$; 8MeV/amu on a copper target; varying intensity*

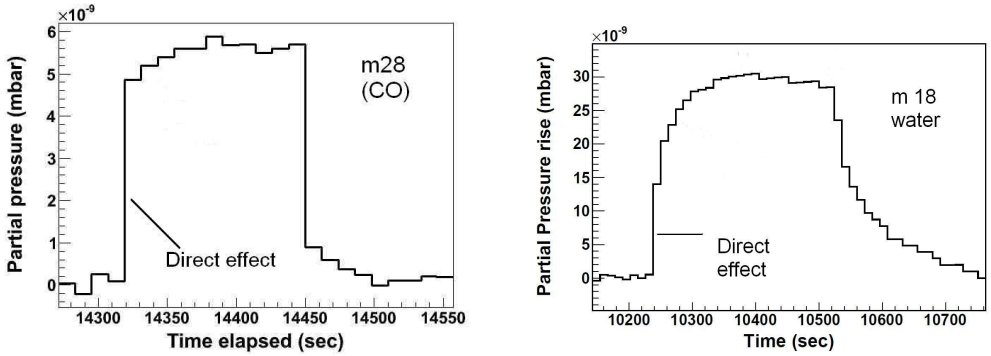

Figure 7.2: *Pressure response after background reduction from RGA data for $^{129}Xe^{16+}$ on Aluminum target*

mass 32 (O_2) indicating that only a small part of the mass 28 peak corresponds to nitrogen and the rest would be CO or C_2H_2. This CO/C_2H_2 stems from the breakdown of contaminants, namely heavier hydrocarbons, presumably from machine oil, O-rings etc.

From our observations we determine the dependence of the desorption yield on various factors, namely the angle of incidence, the target material and the energy of the beam. These factors have also been investigated in previous experiments [15]. The pressure increase observed in the RGA is used to find the desorption yield using

equation 6.4. For CO and CO_2, we are not certain about additional sinks apart from the pump in the setup. For H_2O determination of the absolute pumping speed is not possible due to pumping of the water vapour by the walls of our setup caused by the high sticking factor of water. Thus for all the rest gas species the values for the desorption yields calculated are strictly speaking lower limits. We currently have no knowledge of the error bars to be put on the measurements for water and an accurate measurement of the pumping speed of water might be considered in the future.

7.3 Dependence on beam intensity

The desorption yield depends on the particle flux on the target surface, which is directly proportional to the beam intensity. Figure 7.1 shows that for all rest gas species an increase in intensity gives a higher yield. The detailed analysis displayed in figure 7.3 shows the pressure increase to be linearly proportional to the the beam

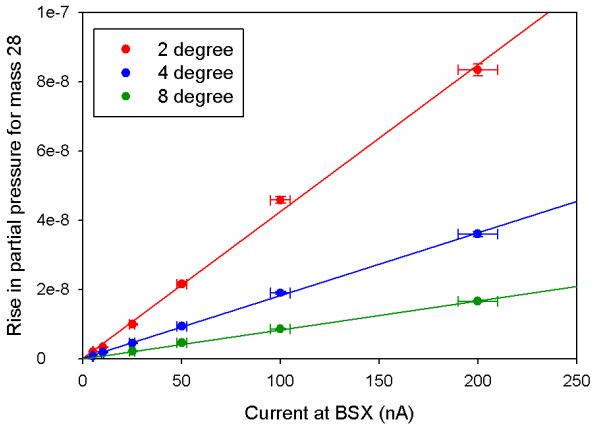

Figure 7.3: *Dependence of increase in pressure measured by RGA on the intensity for $^{40}Ar^{5+}$, 8MeV/amu on a copper target, varying angle of incidence*

current at a given angle of incidence. The different slopes for the different angles also indicates a dependence on the angle of incidence, which is discussed in section 7.4. Using this intensity dependence we scaled the increase in pressure with the current at BSX.

7.4 Dependence on angle of incidence

Existing literature [52] shows that desorption yield changes with the angle of incidence of the beam, with perpendicular incidence having a lower yield than small angle incidences. Our orbit calculations show a distribution of the angle of incidence of lost ions between 0° to 8°. Earlier studies have not explored the shallow angle region in great detail. Experiments done at CERN with 4.2 MeV/amu lead ions for just 2 angles, 0.8° and 5.2° [15] determined that the angular dependence is less significant than a $(1/\sin\theta)$ dependence. We looked in more detail at shallow angles of incidence to examine angular dependence of the desorption yield.

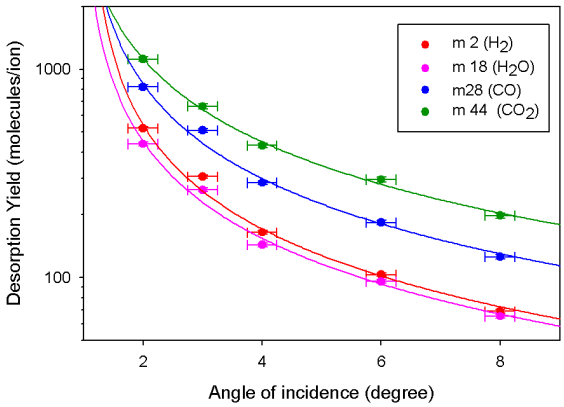

Figure 7.4: *Dependence of desorption yield on the angle of incidence for $^{40}Ar^{5+}$; 8MeV/amu on a copper target; for incident intensity at BSX 200nA*

In figure 7.4, desorption yield for different rest gas species has been plotted for different angles of incidence for the same beam power (scaled to 200 electrical nA at BSX). Initially each of the mass species was fitted to the inverse of the angle of incidence $(a/(b+\theta))$. (For small values of θ, $\sin\theta$ was approximated as θ in the fit.)

From the fit parameters as shown in table 7.1 the parameter b indicates that there is a constant offset of about 1°. This systematic error was due to an offset in the angle as discussed in section 6.6. With the introduction of the XY table, this systematic offset was significantly reduced. Figure 7.5, shows the angle dependence for a Xe beam on a copper target after the design modifications (section 6.6) were made. In the figure there are two data point corresponding to every angle, because two measurements are taken at each angle as shown in figure 6.15 in section 6.11. Since the surface history changes, the measured increase in pressure at a particular angle also

Rest gas species	$a(\times 10^2$ molecule/ion)	b° (degree)	R^2
m 2	4.7±0.3	-0.95 ± 0.12	0.97
m 18	5.0±0.3	-0.98 ± 0.12	0.98
m 28	9.2±0.6	-0.92 ± 0.13	0.98
m 44	14.9±0.5	-0.90 ± 0.13	0.91

Table 7.1: *Fit parameters for different RGA species as shown in figure 7.4 for the equation y =(a/(b+θ))*

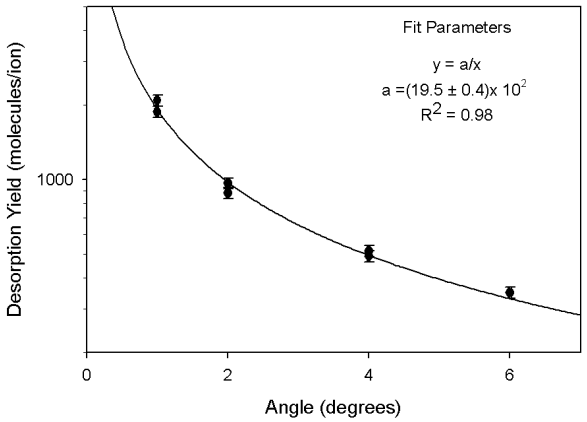

Figure 7.5: *Dependence of desorption yield on the angle of incidence for mass 28 ;* $^{129}Xe^{16+}$ *, 8MeV/amu on a copper target; for incident intensity at BSX 200nA*

changes. When the data points in figure 7.5 are fitted with the equation $y = a/(b+\theta)$, the best fit has $b = (-0.04 \pm 0.008)^\circ$ and $a = (20 \pm 1) \times 10^2$ molecules/ion indicating a significantly reduced angular systematic error.

7.5 Dependence on target material

Existing literature [15] indicates that the amount of gas desorbed from the target surface also depends on the material. We investigated a dependence on the surface material as shown in figure 7.6. From the experiments we observed that for all rest gas species the yield from the aluminum surface is considerably lower than the others. Experiments conducted at GSI [30] for a U^{73+} at energies 15, 40 and 100 MeV/amu show the desorption yield of copper to be less than aluminum or stainless steel. These measurements have been done for perpendicular incidence at

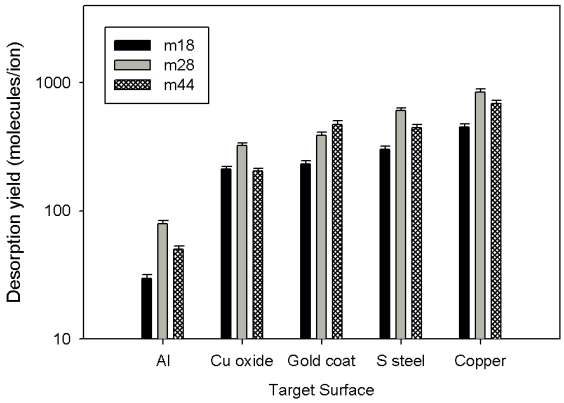

Figure 7.6: *Dependence of desorption yield on different target surfaces at 2° for $^{40}Ar^{5+}$ at 8 MeV/amu, with incident intensity of 200 nA at BSX*

Target material	Density (g/cm^3)
Aluminum	2.7
Copper oxide	5.2
Gold on top of copper	19.3
Stainless Steel	8.0
Copper	8.9

Table 7.2: *Density of different materials used in SRIM*

a base pressure of 10^{-10} mbar, which differ from our experimental conditions and may explain the deviation from our observations.
The yield from the gold coated surface is less than the yield from the stainless steel and the freshly machined copper surfaces, but this decrease is not very significant. The low yield for aluminum prompted us to investigate a potential density dependence as shown in figure 7.7. Here the increase in pressure is plotted as a function of target material density in g/cm^3. The target density is taken to be the density of the surface material. For the gold coated copper at small angles the density of gold is used since SRIM simulations show that ions for our angular range do not penetrate through the gold layer into the bulk material.

Table 7.2 gives a list of our target materials and their density taken from [62]. However we do not observe a simple linear dependence on target density. This leads us to consider material density alone might not be the explaining factor.

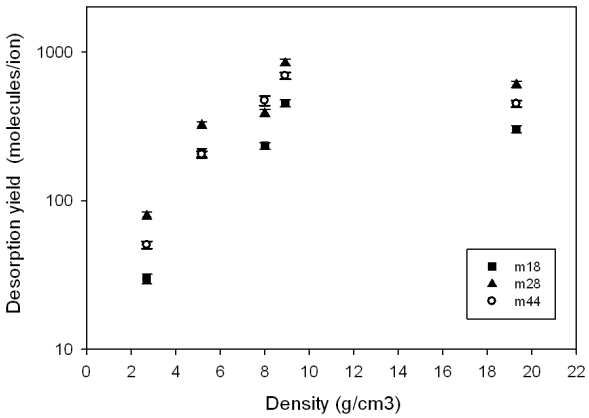

Figure 7.7: *Dependence of desorption yield for different target surface densities (used in SRIM [62]) at 2°, for $^{40}Ar^{5+}$ at 8 MeV/amu, with incident intensity of 200 nA at BSX*

7.6 Dependence on stopping power

Desorption is caused by the breaking of van der Waals bonds on the target surface by secondary electrons. Existing models for desorption (as listed in [29] and [52]) predict a scaling with the electronic stopping power $(dE_e/dx|_i)^n$ on incidence:

- The electronic stopping power, dE_e/dx, is used since it is a good measure of the power input at the surface.
- The stopping power at incidence is used because the release of materials is assumed to be from the surface of the target.

The most widely accepted model is the thermal spike model according to which the desorption yield scales with $\left(\frac{dE}{dx}\right)^2$ [15]. Other models predict a stopping power scaling with $n = 1.5$ (shock wave model [49]) and $n = 3$ (pressure pulse model [51]). However, the results obtained from our experiments are not consistent with either of those models.
Figure 7.8 shows the desorption yield as a function of the electronic stopping power on incidence. In the figure the data with the lowest $\left(\frac{dE}{dx}\right)_e$ have been obtained with the O^{2+} beam while the highest $\left(\frac{dE}{dx}\right)_e$ have been obtained with the Xe^{16+} beam. Note that in our case the stopping power has been varied by changing the ion species while having the same energy per amu and not by changing the ion energy [52]. In previous experiments [30] the data have been fitted to the model with

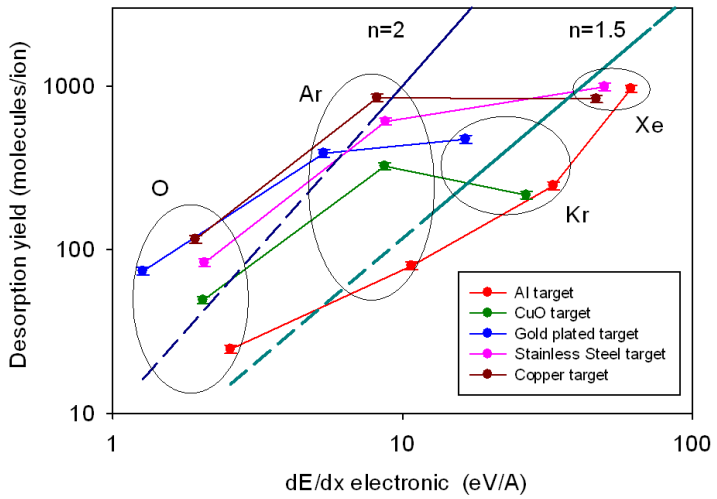

Figure 7.8: *Dependence of desorption yield on the surface stopping power compared to different models ([29] and [52]); for mass 28, 200 nA at BSX; all beams on target at 2°*

Ion	Energy (MeV/amu)	Pressure (mbar)	Angle (degree)	Target	Yield (1/ion)	Yields (KVI) (1/ion)
Ar^{9+} [63]	9.7	10^{-10}	90 °	Cu	53	82 (Ar^{5+})
Pb^{27+} [13]	4.2	10^{-10}	5.2°	SS	1234	1575 (Pb^{27+})
Pb^{27+} [13]	4.2	10^{-10}	0.8°	SS	5575	8230 (Pb^{27+})
Ar^{10+} [30]	40	10^{-10}	90°	SS	47	55 (Ar^{5+})

Table 7.3: *Desorption yield as determined by different experiments, compared to yields from our experiment (all at 8 MeV/amu). Results from KVI have been scaled to the angles (SS stands for stainless steel). For the Pb we use data from Cu as this no data for Pb on stainless steel.*

an arbitrary scaling factor. To represent these models in our fits we have also used an arbitrary scaling factor.

The average desorption yield is significant, releasing about 10^3 molecules per ion incident at 2°. This is roughly of the same order when compared to desorption yields from other experiments, see Table 7.3. For all of our experiments the energy is 8 MeV/amu. For the comparison of our results with the previous measurements our measurements have been scaled using a $1/\sin(\theta)$ dependence. This angular dependence might not be valid at larger angles as seen in [13]. For perpendicular incidence only the surface energy density has a effect (as stated by the thermal spike model) while for grazing angles we expect the total energy deposit to be significant. Future

experiments at higher angles of incidence are required to complete our understanding of the angular dependence. In the comparison for small angles, we have used data for incidence of Pb on Cu as we did not have any data on stainless steel. Going by the trends as shown in figure 7.8 we expect yields for stainless steel to be comparable. We expect our desorption yields to be higher since the energy deposition of the particle track in the bulk also contributes. The total energy is also higher in our case.
The existing models (thermal spike, shock wave) have all been developed for perpendicular incidence and thus have limited applicability in our case. Based on these observations we tried to come up with a different mechanism to explain desorption at small angles of incidence.

7.7 Model for desorption

The desorption yields found in our experiments and the disagreement between the data and models discussed in chapter 5 (figure 7.8) in terms of stopping power dependence prompted us to look into the possible desorption mechanisms at grazing angles of incidence. From the experimental results we have determined an inverse dependence on the angle of incidence. This angular dependence can be explained in different ways:

- Change in surface area: Desorption depends on the surface area being heated by a single beam particle on a particular target, which depends on the impact angle. Figure 7.9 shows a schematic diagram for beam on target, where the area over which the energy is initially deposited by an individual beam particle (the Bohr adiabatic radius or the secondary electron range, whichever is larger) is represented by a cylinder. The area of the intersection of this cylinder, in which the energy is initially deposited, and the target surface scales with $1/\sin(\theta)$. In a simplified picture this may explain the observed $1/\sin(\theta)$ behaviour of the desorption yield.

- Change in the depth of the Bragg peak: When a beam particle is incident on a surface at an angle, the range of the particle in the material remains the same. The temperature increase at the target surface caused by the diffusion of the energy deposited along the track into the target material will in first order be inversely proportional to $\sin(\theta)$ and to the distance along the particle track. This temperature increase will lead to additional outgassing as compared to the prediction of the thermal spike model.

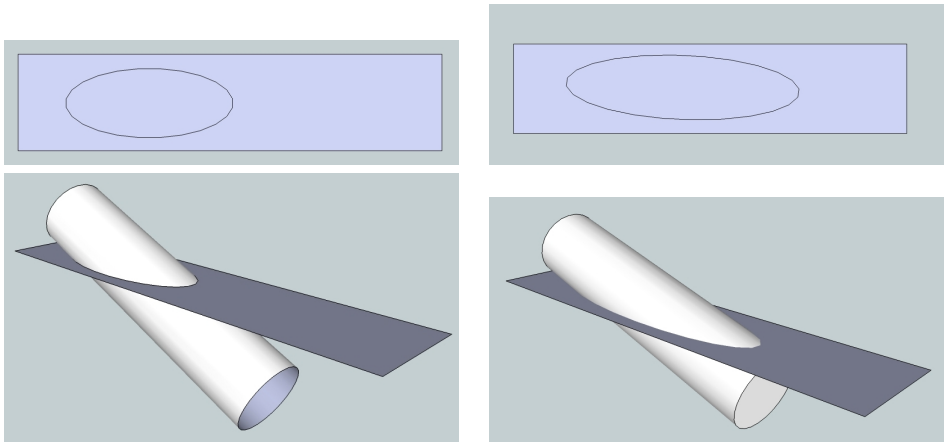

Large angle of incidence Small angle of incidence

Figure 7.9: *Schematic diagram of a beam on target surface for small and large angles*

The shockwave mechanism described in chapter 5.4, that also has a $1/\sin(\theta)$ dependence [49], is expected to give a minor contribution to the total desorption yield because the conditions are fulfilled for very small part of the particle track only.

Based on these observations we propose an extension of the thermal spike model

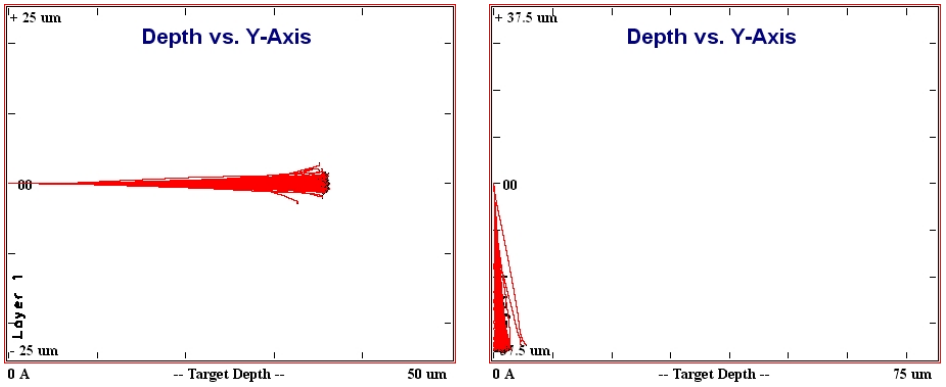

Perpendicular incidence 2° angle of incidence

Figure 7.10: *Ion tracks for $^{40}Ar^{5+}$ at 8MeV/amu on copper for normal and grazing angles of incidence as calculated by TRIM [62].*

as a possible mechanism for the angular dependence of the desorption yield at grazing incidence. The energy initially deposited in a cylinder of which the axis is the particle trajectory and the radius the Bohr adiabatic radius, diffuses into the target

material and creates a time dependent temperature distribution at the surface that leads to increased outgassing according to equations 5.7 and 5.8. The temperature distribution $T(r,t)$ in these equations can be calculated by numerical integration in 3 dimensions of the diffusion equation 5.1, using equation 5.6 to define the initial temperature distribution along the particle track.

Figure 7.10 shows the ion tracks for $^{40}Ar^{5+}$ at 8 MeV/amu on copper at perpendic-

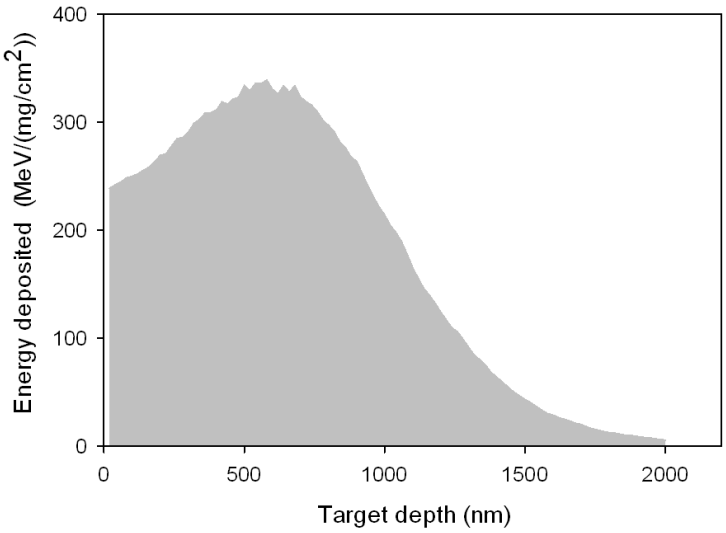

Figure 7.11: *Depth distribution of deposited energy for $^{40}Ar^{5+}$ at 8 MeV/amu on a copper surface , 2° angle of incidence*

ular and at 2 deg incidence, simulated using TRIM [62]. The average energy deposition as a function of depth below the surface integrated over the particle tracks for the 2° case is displayed in figure 7.11.

From these simulations we calculate the energy deposit weighted depth according to equation 7.1 for all target - ion combinations.

Along the energy deposition curve, the energy lost per unit tracklength (x), at a depth $d(x)$ (taken on an axis perpendicular to the surface), is taken to be $S(x)$ in MeV/(mg/cm^2). The weighted depth, $\bar{d}$, is determined from:

$$\bar{d} = \frac{\int (S(x) \times d(x) dx}{\int S(x) dx} \tag{7.1}$$

Figure 7.12 shows the dependence of the desorption yield on the weighted depth. As in figure 7.8, we have different ion species at the same energy per amu. The lines joining the plotted points are to guide the eye. From the figure, we observe

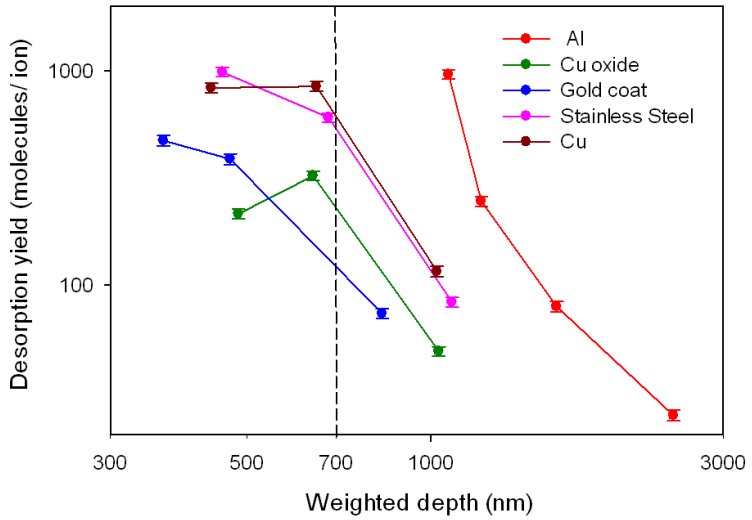

Figure 7.12: *Dependence on weighted depth compared to different models; for mass 28, 200 nA at BSX; all beams on target at 2°*

a saturation depth at around 700 nm: if the ion has a weighted depth less than the saturation depth, the desorption yield is fairly constant, while for higher weighted depths the desorption yield decreases with weighted depth. Further experiments are needed to quantify and verify the dependence of desorption yield on weighted depth.

7.8 Conclusion

We investigated the ion-induced desorption yield on various targets at shallow angles of incidence. We observed a linear dependence with the beam intensity and an inverse dependence on the angle of incidence. The observed angular dependence can in a simplified view be explained by the $1/\sin(\theta)$ dependence of the cross section between the surface and the radial energy distribution around the track. The stopping power dependence of the thermal spike model does not match our results, as shown in figure 7.8. The experiments show desorption yields at 2° to be of the

order of 10^3 molecules/ion. We have compared our results to other experiments (table 7.3) and have found their yields to be similar to our experimental results.
To present the effect of energy deposited below the surface, we propose a new parameter, the weighted depth $\bar{d}$. For any beam on a target material the weighted depth can be calculated using equation 7.1. Using the parameter $\bar{d}$ and the trend for desorption as shown in 7.12, the desorption yield may be predicted within a factor two or three.
A more detailed analysis requires a comprehensive 4D simulation of the heat diffusion starting from the actual particle track to determine the evolution of the surface temperature distribution and the consequent desorption.
We also calculated the desorption yield in the cyclotron from the experimental data

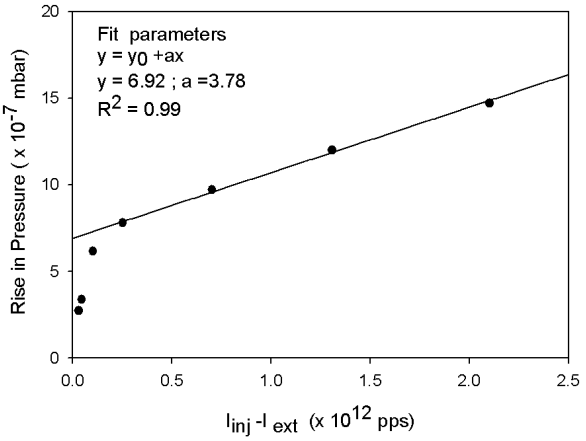

Figure 7.13: *Ratio of rise in pressure per lost beam particles in the cyclotron for $^{40}Ar^{5+}$ at 8 MeV/amu*

as shown in figure 1.1 using the simple model in equations 1.1 and 1.2. Assuming that the overall effective pumping speed in the cyclotron is about 500 liters/s from the slope of rise in pressure per number of particles lost as shown in figure 7.13, we calculate the total desorption yield in the cyclotron to be 4500 molecules/ion. From our desorption measurements for the same beam we determine the desorption yield for the same beam to be 2300 molecules/ion. This difference may be due to the contribution to the vacuum degradation of desorption related to rest gas ionization by the beam particles. The low energy ions produced in this process will hit the walls of the vacuum chamber and release adsorbed material. Another possible explanation is that the effective pumping speed in the cyclotron is lower than anticipated.

Chapter 8

Summary and outlook

8.1 Summary of results

Vacuum induced beam loss and the subsequent feedback loop in the AGOR cyclotron is a limiting factor in delivering higher intensities for low energy heavy ion beams, especially for the ^{206}Pb beam. Our exercise in understanding the subsystems involved in the beam loss process yielded the following results.
During acceleration, some of the beam particles undergo a charge exchange with the rest gas present in the machine and start to move on a modified trajectory, and are eventually lost in the cyclotron. The number of particles lost depends on the pressure in the cyclotron and the cross-section of interaction. Our calculations show that for an equilibrium pressure higher than 10^{-7} mbar, the transmission in the machine decreases quite rapidly (figure 3.3b). A similar decrease in the transmission is also calculated for the low energy beam line connecting the ECR ion source to the cyclotron. Based on these calculations improvements were made in the vacuum of the LEB line which improved the transmission significantly.
The charge exchanged particles precess in the machine till they hit either the center or the periferial walls of the cyclotron. The orbit calculations show that in particular for heavier ions like Xe and Pb, most of the particles need multiple charge exchanges till they finally hit the periphery walls. The number of charge exchanges required for the orbit to become unstable so that the particle ends up on the walls decreases with radius. Simulations also showed that the particles which do hit the walls after a single charge exchange have a very shallow angle of incidence between 1° and 8°.
On hitting the walls of the cyclotron, these lost particles deposit their energy and subsequently desorb materials from the surface. Based on the results of the orbit calculations an experiment was set up to measure ion-induced desorption for shallow angles of impact. Using a rest gas analyzer it was possible to obtain species specific data where we observed that while the base pressure was water dominated, a substantial contribution of the pressure rise came from CO and CO_2.
We measured with a finer angular spacing than previous experiments [15] and the results showed the desorption yield to be inversely proportional on the impact an-

gle. This angular dependence is valid for all rest gas species individually.
The experimental results also show aluminium to have the least desorption at grazing angles of incidence. Gold plating did not result in a substantial decrease in the desorption yield in contrast with results obtained at GSI [59] at much lower pressures.
Desorption yields from our experiments are of the order of 10^3 for most of the beams (all at energies 8 MeV/amu) on different surfaces. These values are in reasonable agreement with those of other desorption experiments at grazing angles [13].
To compare our results we consider existing models, notably the thermal spike model. The thermal spike model has been previously used for perpendicular incidence of beam particles on targets and considers only the energy lost on the surface. Our results do not agree with yields predicted by the thermal spike model used in other experiments [29]. For small angles of incidence we argue that the contribution from the energy deposited in the sub-surface layers is also significant and that a 3D extension of the thermal spike model may explain the measurements. A new parameter 'weighted depth' is introduced which aims to predict the desorption yield at small angles for any beam on a particular target surface.

8.2 Outlook

To gain a better understanding of the beamloss processes further investigation of the following aspects is desirable :

- Desorption yields have an inverse dependence on the angle of incidence at small angles. However, we have no data to verify this scaling for larger angles especially for perpendicular impacts. Experiments over the entire angular range from 10° to 90° would be able to bridge this gap.

- In our experiments all the beams had the same energy per amu. To have a better predictability at small angles we need to know the dependence of desorption yield on the total beam energy. This information can be obtained by performing experiments for the same ion species at different total energies.

- We did not measure the temperature in our target material. The pressure rise spectrum for the rest gas species, especially the water peak, suggests that apart from instantaneous effects, bulk effects such as temperature rise are also significant. Future experiments might consider recording and controlling the temperature in the target material.

- For the AGOR cyclotron, determination of the effective pumping speed still remains to be done. An accurate pressure profile in the interior of the cyclotron would also improve the accuracy of our calculated transmissions. We also do not have RGA data during experiments in the cyclotron. In the future recording the species specific data for the rest gas due to ion induced desorption in the cyclotron is recommended.

8.3 Mitigation Methods

To improve transmission for heavy ion beams in the cyclotron, we look at the three main aspects leading to transmission losses as shown in figure 8.1

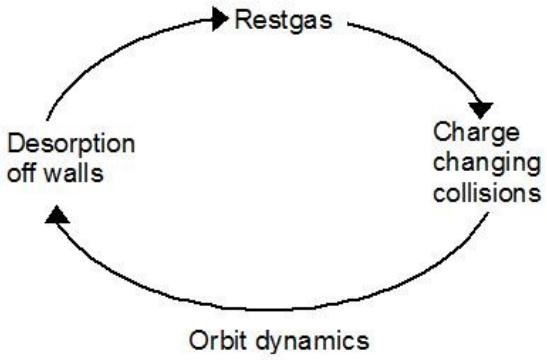

Figure 8.1: *Schematic diagram of the beamloss feedback cycle*

- Rest gas: Ideally improving the effective pumping speed inside the machine should give a better transmission for heavy ions. From transmission calculations we have seen that a factor of 10 decrease in equilibrium pressure leads to a substantial rise in transmission as shown in figure 3.3b. We are currently restricted in the lowest standard operating pressure of the machine to a few times 10^{-7} mbar due to design constraints. An 18 mm vertical aperture in the vacuum chamber and presence of physical obstructions like the RF liners and the extraction elements limit the effective pumping speed in the cyclotron. Therefore, it is not possible to increase the pumping speed substantially.
- Charge changing collisions: The charge exchange process between the rest gas and beam particles is a physical phenomena in which the cross-section

is dependent on the energy and the charge state of the beam projectile. As shown in figure 3.2, the cross-section for charge exchange is lower for higher charge states. However higher charge states have lower intensities from the ECR source. To obtain the best charge state we need to optimize the beam-loss and the intensity available at the source for the given charge state.

- Ion induced desorption: This is the only part of the feedback cycle which we might influence. Decreasing desorption yield due to the beam will lead to reduced beam losses. We look at three possible ways of doing so.

  1. Introduction of scrapers
  2. Coating to seal bulk effects
  3. Surface treatments

  A short discussion about the feasibility and limitations of each of these processes is given below.

8.3.1 Scrapers

The orbit calculations show that most of the beam particles which hit the outer wall of the cyclotron are incident at a shallow angle. The desorption experiment shows that the yield decreases with an increase in angle of incidence. From these two observations it can be concluded that if the lost particles can be made to hit the outer walls perpendicularly, then the contribution from ion-induced desorption can be limited. Introduction of scrapers along the outer wall is a possible solution in this respect. Similar scrapers have also been employed at the SIS18 in GSI [64]. However there are limitations in attaching scrapers to the side walls. Near the extraction radius the outer most orbits of the stable beam are only millimeters away from the outer wall. Any scraper in that region will shave off accelerated beam, which is not acceptable.

8.3.2 Surface coating

Another method to limit ion induced desorption is to coat specific surface areas with different materials. Based on studies done at GSI [59] which claim a substantial decrease in the desorption yield for perpendicular incidence on gold (25-80 molecules/ion instead of 10^3 molecules/ion without the coating), gold plating was done on roughly half the circumference of the outer walls of the AGOR cyclotron vacuum chamber. The median plane region of the RF liners and the inflector housing has been coated, with a 0.5 μm nickel later on the copper surface and a 1 μm

gold layer on top of the nickel. During subsequent operations the dependence of the pressure on the beam intensity did not decrease significantly. In our experiments to measure desorption, a gold plated surface gave an improvement in the desorption yield by only a factor of 2.
From the experimental results it has been seen that aluminum has a lower desorption yield at grazing angles of incidence. An extensive study is needed to determine the feasibility of aluminum coating in our case.

8.3.3 Surface treatment

Experiments done with heavy ion beams for beam time greater than 72 hours have shown a gradual improvement of vacuum inside the machine due to beam cleaning of the interior of the cyclotron. In our desorption experiments we have also seen an improvement in the vacuum due to beam-cleaning of the target surface. This method can be used to help improve the vacuum, but it is not durable. It has been observed during experiments that after beam induced cleaning is done, the effect does not last after beam is switched off.

Appendix A

Pressure profile calculations

In order to obtain an estimate of the pressure distribution in the cyclotron simulations were done with the MOLFLOW [26] code. MOLFLOW is a Monte Carlo code that tracks individual particles in the vacuum, neglecting collisions between particles. The surface geometry of the vacuum chamber is in MOLFLOW defined by triangular facets. To these surface facets an outgassing rate and a sticking probability is associated and the pressure is measured as the surface density of hits. MOLFLOW

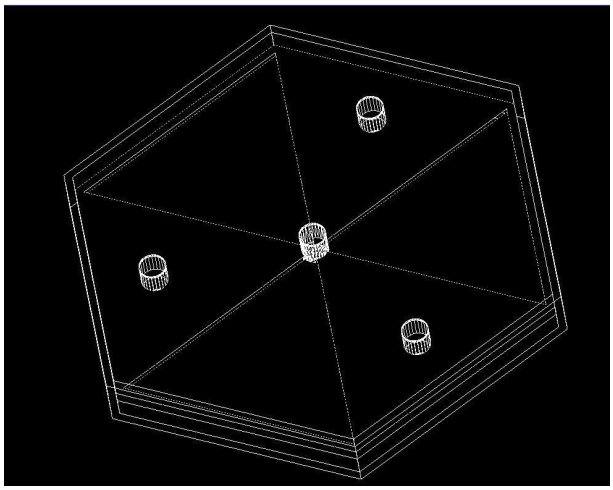

Figure A.1: *Diagram of vacuum chamber used in MOLFLOW calculations*

accepts the chamber geometry in the form of STL files [65]. Due to the difficulty in making STL files of complex geometries we simplified the geometry of our vacuum chamber and represented it by a hexagon as shown in figure A.1. The six triangles make up the 3 hills and 3 valleys respectively. In the center there are two circular openings in the top and bottom representing the axial injection line and inflector line. The center of each sector has a circular opening on the top and bottom which represents the cryo-pumps. The distance from the center to the outer boundary is

100 mm while each of the circular opening has a diameter of 10 mm, thus representing a 1:10 scale model of the cyclotron. These pumping surfaces have a sticking

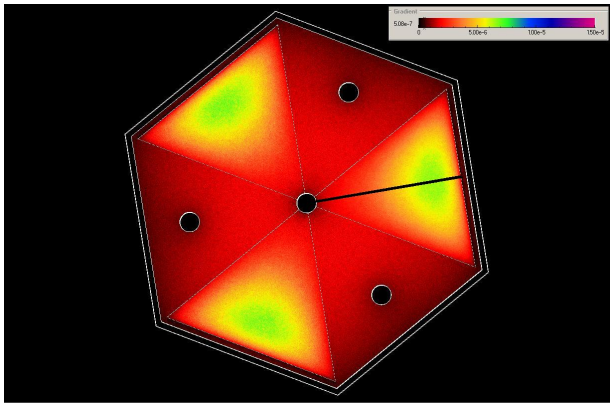

Figure A.2: *Density of hits on the inner wall of the vacuum chamber, with the center acting as a pump*

factor of 1. Three boundary walls on the circumference have a sticking factor of 0.5, representing the turbo pumps. The rest of the surfaces have an outgassing rate of

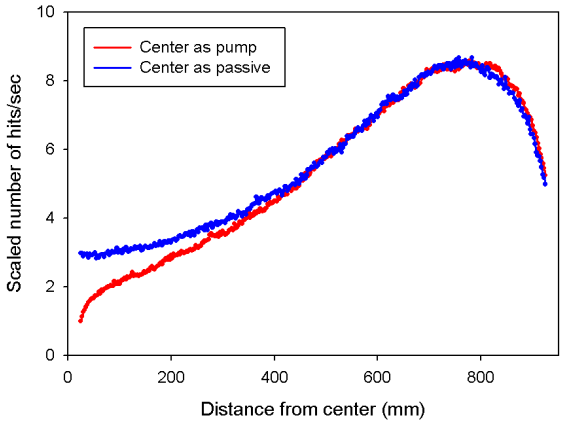

Figure A.3: *Scaled relative pressure in the interior of the machine along a valley sector*

1 m^3/s. The values used are just to give a relative pressure profile. In three sectors we simulated the extraction channels by adding an inner wall 2 mm away from the

outer boundary wall. The outer walls of the extraction channels also have a sticking factor of 1 to simulate pumping at the circumference. Simulations were done taking the central region as a pump and as a passive element (no desorption, no sticking). Figure A.2 shows the density of the number of hits on the top wall. The average pressure profiles along one of the hills (as shown by the line in A.2) is plotted in figure A.3. This profile is relative, with the pressure at the center, with the center as a pump, being considered as unity. The pressure in the central region depending on it being a pump or a passive region, varies to a factor of three. The pressure in the valleys is lower than the hills due to the close proximity to the pumps. In the cyclotron also we expect that the pressure measured at the perifery near the pumps is greater than the actual pressure in the central injection region.

Appendix B

Bending and focussing limits

B.1 Bending limit

The bending limit of a cyclotron which gives the maximum energy of the accelerated particle, is defined by the maximum possible field strength and the extraction radius.The magnetic field strength B is related to the momentum of the accelerated particle p and the charge q by

$$B\rho = \frac{p}{q} \tag{B.1}$$

where ρ is the bending radius of the particle. At extraction ρ is a constant (extraction radius) and p reaches its maximum. Using the classical expression for kinetic energy $T = p^2/2m$, where m is the mass of the particle, and equation B.1, the maximum achievable energy is given by

$$\frac{T}{m} = \frac{B^2\rho^2q^2}{2m^2} \tag{B.2}$$

The mass can be written in atomic mass units ($m = A \times amu$) and the charge is written in therms of the charge state ($q = Q \times e$). Taking all the constants together. equation B.2 can be rewritten as

$$\frac{T}{m} = K_b(\frac{Q}{A})^2 \tag{B.3}$$

where K_b is called the bending limit.

B.2 Focussing limit

The focussing limit of a spiral sectored cyclotron is determined by the conditions of axial beam stability that follow from the equation of motion for the axial betatron motion of the particles. When accelerating particles to relativistic energies in a cyclotron the magnetic field has to increase with radius in order to maintain the isochronism needed for continued acceleration. This radial gradient causes an axial defocussing that has compensated by the axial focussing provided by the azimuthal

field variation in order to have axial confinement of the beam. The vertical betatron frequency for acyclotron with spiralled sectors is given by

$$\nu_z^2 = k + \frac{N^2}{N^2 - 1} F(1 + 2\tan^2 \xi) \tag{B.4}$$

where N is the number of sectors in the machine and ξ is the spiral angle [66]. The parameter k represents the field index which gives a measure of the change in the magnetic field as a function of the radius r.

$$k(r) = -\frac{r}{B}\frac{dB(r)}{dr} \tag{B.5}$$

In a relativistic case where the magnetic field scales as the relativistic factor γ to maintain isochronism, equation B.5 can be written as

$$-k(r) = 1 - \gamma^2 = (\beta\gamma)^2 \propto (p/m)^2 \tag{B.6}$$

where p is the momentum and m is the mass of the particle.
The factor F or flutter, gives a measure of the field modulation as shown

$$F = \frac{\langle B^2 \rangle - \langle B \rangle^2}{\langle B \rangle^2} = \frac{(B_{hill} - B_{valley})^2}{8\langle B \rangle^2} \tag{B.7}$$

where B_{hill} and B_{valley} is the field in the hill and valley sector, and $< B >$ is the magnetic field averaged over a certain radius [66].
In a normally conducting machine the flutter is constant with $B_{hill} - B_{valley}$ scaling with $\langle B \rangle$. In a superconducting machine where the magnet iron is completely saturated, $B_{hill} - B_{valley}$ is a constant hence $F \propto 1/\langle B \rangle^2$. Using equation B.1 the flutter can be written as $F \propto q^2/p^2$. Using the approximations for the field index and the flutter, we can write the axial betatron frequency as

$$\nu_z^2 = -C_1(p/m)^2 + C_2(q^2/p^2) \tag{B.8}$$

where C_1 and C_2 are appropriate constants. Axial focussing vanishes at $\nu_z = 0$, i.e. for $p^4 = Cq^2m^2$.
From the expression for energy $T = p^2/2m$, mass and charge, we find

$$\frac{T}{m} = \frac{p^2}{2m^2} = \frac{Cqm}{2m^2} = K_f(\frac{Q}{A}) \tag{B.9}$$

where K_f is called the focussing limit.

Bibliography

[1] K. Jungmann, G. P. Berg, U. Dammalapati, P. Dendooven, O. Dermois, M. N. Harakeh, R. Hoekstra, R. Morgenstern, A. Rogachevskiy, M. Sanchez-Vega, R. Timmermans, E. Traykov, L. Willmann, and H. W. Wilscut, "TRIμP-trapped radioactive atoms-icrolaboratories for fundamental physics," *Physica Scripta*, vol. 2003, no. T104, p. 178, 2003.

[2] D. Bakker, J. Beijers, G. Berg, A. van den Berg, S. Brandenburg, O. Dermois, H. van der Duin, I. Formanoy, K. Jungmann, H. Kiewiet, P. Kroon, F. Rengers, J. Sijbrin, L. Slatius, I. Smid, R. Terol, D. Toprek, S. van der Veen, J. de Vries, N. van Wiefferen, P. Wieringa, and H. Wilschut, "Upgrade of the AGOR facility for the TRIμP project," annual report, Kernfysisch Versneller Instituut, 2002.

[3] R. Calder, "Ion induced gas desorption problems in the ISR," *Vacuum*, vol. 24, no. 10, pp. 437 – 443, 1974.

[4] J. Bosser, C. Carli, M. Chanel, C. Hill, and A. Lombardi, "Experimental investigation of electron cooling and stacking of lead ions in a low-energy accumulation ring," *Part. Accel.*, vol. 63, pp. 171–210, 1999.

[5] W. Fischer, "Vacuum pressure rise with intense ion beams in RHIC," in *Proceedings of the European Particle Accelerator Conference*, 2002.

[6] A. Kramer, O. Boine-Frankenheim, E. Mustafin, H. Reich-Sprenger, and P. Spiller, "Measurement and calculation of U28+ beam lifetime in SIS," in *Proceedings of the European Particle Accelerator Conference*, 2002.

[7] S. Brandenburg, "AGOR status report," in *Proceedings of the 17th International Conference on Cyclotrons and their Applications*, p. 90, 2004.

[8] S. Brandenburg, "High intensity operation of the AGOR cyclotron for RIB production," in *Proceedings of the 18th International Conference on Cyclotrons and their Applications*, p. 493, 2007.

[9] M. Hofstee, S. Brandenburg, and W. K. van Asselt, "Improvement in the AGOR vacuum," Annual report, Kernfysisch Versneller Instituut, 2003.

[10] S. P. Moller, "Beam-Residual gas interactions," in *CERN Accelerator School- Vacuum Technology*, 1999.

[11] E. Mustafin, O. Boine-Frankenheim, I. Hofmann, H. Reich-Sprenger, and P. Spiller, "A theory of the beam loss-induced vacuum instability applied to the heavy-ion synchrotron SIS18," *Nuclear Instruments and Methods in Physics Research Section A: Accelerators, Spectrometers, Detectors and Associated Equipment*, vol. 510, no. 3, pp. 199 – 205, 2003.

[12] V. Nuttens, "Cyclotron vacuum model and H-gas stripping losses," in *Proceedings of the 19th International Conference on Cyclotrons and their Applications*, p. 200, 2010.

[13] E. Mahner, J. Hansen, J.-M. Laurent, and N. Madsen, "Molecular desorption of stainless steel vacuum chambers irradiated with $4.2\ \mathrm{MeV/u}$ lead ions," *Phys. Rev. ST Accel. Beams*, vol. 6, p. 013201, Jan 2003.

[14] O. Malyshev and A. Rossi, "Ion desorption vacuum stability in the LHC the multigas model," in *Proccedings of European Particle Accelerator Conference*, 2000.

[15] E. Mahner, "Review of heavy-ion induced desorption studies for particle accelerators," *Phys. Rev. ST Accel. Beams*, vol. 11, p. 104801, Oct 2008.

[16] E. O. Lawrence and M. S. Livingston, "The production of high speed light ions without the use of high voltages," *Phys. Rev.*, vol. 40, pp. 19–35, Apr 1932.

[17] S. Brandenburg, W. van Asselt, M. Hofstee, and H. Post, "Vertical beam motion in the AGOR cyclotron," in *Proceedings of European Particle Accelerator Conference*, 2004.

[18] S. Brandenburg and L. de Vries, "The RF system of the AGOR cyclotron," in *Proceedings of the 15th International Conference on Cyclotrons and their Applications, Caen, France*, 1998.

[19] L. H. Thomas, "The paths of ions in the cyclotron i. Orbits in the magnetic field," *Phys. Rev.*, vol. 54, pp. 580–588, Oct 1938.

[20] K. R. Symon, D. W. Kerst, L. W. Jones, L. J. Laslett, and K. M. Terwilliger, "Fixed-Field Alternating-Gradient particle accelerators," *Phys. Rev.*, vol. 103, pp. 1837–1859, Sep 1956.

[21] S. Brandenburg, W. van Asselt, H. Post, and H. Schreuder, "Beam diagnostics in the AGOR cyclotron," in *Proceedings DIPAC*, p. 80, 2003.

[22] M. Stokroos and S. Brandenburg, "Revision of the AGOR main magnet power supplies," annual report, Kernfysisch Versneller Instituut, 2004.

[23] S. Brandenburg, L. Roobel, and H. Post, "Vertical perturbation of high-energy proton beams in the AGOR cyclotron," in *Proceedings of the 17th International Conference on Cyclotrons and their Applications*, p. 408, 2001.

[24] Leybold, *Operating Instructions TURBOVAC 1000*. LEYBOLD AG, ga 05.103 ed.

[25] A. Horbowa and S. Buhler, "The AGOR cyropumps," in *12th International conference on cyclotrons and their applications* (B. Martin and K. Zeigler, eds.), p. 224, 1989.

[26] R. Kersevan, *MOLFLOW users guide*. Sinchrotrone Trieste, 1991.

[27] P. Grafström, "Lifetime, cross-sections and activation," in *CERN Accelerator School - Vacuum in Accelerators*, 2007.

[28] P. Miller, D. Lawton, and F. Marti, "Beam loss from charge changing collisions in a cyclotron," in *Proc. of the 14th Int. Conf. on cyclotrons and their applications.*, 1999.

[29] M. Bender, H. Kollmus, H. Reich-Sprenger, M. Toulemonde, and W. Assmann, "An inelastic thermal spike model to calculate ion induced desorption yields," *Nuclear Instruments and Methods in Physics Research Section B: Beam Interactions with Materials and Atoms*, vol. 267, no. 6, pp. 885 – 890, 2009. Proceedings of the Seventh International Symposium on Swift Heavy Ions in Matter.

[30] E. Hedlund, "Study of gas-flow metrology and ion-beam induced desorption," Master's thesis, Uppsala University, 2006.

[31] I. D. Kaganovich, E. Startsev, and R. C. Davidson, "Scaling and formulary of cross-sections for ion-atom impact ionization," *New Journal of Physics*, vol. 8, no. 11, p. 278, 2006.

[32] A. Schlachter, "Charge Changing collisions," in *Proceedings of 10th Int. Conference on cyclotrons and its applications*, 1984.

[33] F. Marti, R. C. York, H. Blosser, M. M. Gordon, D. Gorelov, T. Grimm, D. Johnson, P. Miller, E. Pozdeyev, J. Vincent, X. Wu, and A. Zeller, "Analysis of a cyclotron based 400 Mev/u driver system for a radioactive beam facility," 2007.

[34] H. Knudsen, H. K. Haugen, and P. Hvelplund, "Single-electron-capture cross section for medium- and high-velocity, highly charged ions colliding with atoms," *Phys. Rev. A*, vol. 23, pp. 597–610, Feb 1981.

[35] B. Franzke, "Vacuum requirements for heavy ion synchrotrons," *Proceedings of the 9th IEEE Particle Accelerator Conference*, vol. 28, p. 2116, 1981.

[36] H.-D. Betz, G. Hortig, E. Leischner, C. Schmelzer, B. Stadler, and J. Weihrauch, "The average charge of stripped heavy ions," *Physics Letters*, vol. 22, no. 5, pp. 643 – 644, 1966.

[37] R. E. Olson, R. L. Watson, V. Horvat, A. N. Perumal, Y. Peng, and T. Stohlker, "Projectile electron loss and capture in MeV/u collisions of U 28+ with H 2 , N 2 and Ar," *Journal of Physics B: Atomic, Molecular and Optical Physics*, vol. 37, no. 22, p. 4539, 2004.

[38] G. Weber, C. Omet, R. D. DuBois, O. de Lucio, T. Stöhlker, C. Brandau, A. Gumberidze, S. Hagmann, S. Hess, C. Kozhuharov, R. Reuschl, P. Spiller, U. Spillmann, M. Steck, M. Thomason, and S. Trotsenko, "Beam lifetimes and ionization cross sections of U^{28+}," *Phys. Rev. ST Accel. Beams*, vol. 12, p. 084201, Aug 2009.

[39] L. Roobol, "Orbit calculations," annual report, Kernfysisch Versneller Instituut, 1999.

[40] H. Akima, "A new method of interpolation and smooth curve fitting based on local procedures," *J. ACM*, vol. 17, pp. 589–602, Oct. 1970.

[41] B. Milton, "TRIUMF design note, CYCLONE," Tech. Rep. vers 8.4, TRIUMF, 1999.

[42] K. Atkinson, *An Introduction to Numerical Analysis*. John Wiley and sons, New York, 1978.

[43] R. Schuch, H. Schöne, P. D. Miller, H. F. Krause, P. F. Dittner, S. Datz, and R. E. Olson, "Charge and angle-correlated inelasticities in collisions of bare fast carbon ions with neon," *Phys. Rev. Lett.*, vol. 60, pp. 925–928, Mar 1988.

[44] R. E. Olson, J. Ullrich, and H. Schmidt-Böcking, "Multiple-ionization collision dynamics," *Phys. Rev. A*, vol. 39, pp. 5572–5583, Jun 1989.

[45] C. Cocke and R. Olson, "Recoil ions," *Physics Reports*, vol. 205, no. 4, pp. 153 – 219, 1991.

[46] J. P. Schapira, S. Brandenburg, and P. Mandrillion, "Axial injection system for the superconducting cyclotron AGOR," in *Proceedings of the 11th International Conference on Cyclotrons and their Applications*, 1986.

[47] C. Reimann, "Theoretical models for sputtering and desorption of bio-organic molecules under collisional and electronic excitation by ion impact," *Det Kgl. Danske Videnskab. Selskab Mat. Fys. Medd.*, vol. 43, p. 351, 1993.

[48] R. Johnson, "Mechanisms for the desorption of large organic molecules," *International Journal of Mass Spectrometry and Ion Processes*, vol. 78, no. 0, pp. 357 – 392, 1987.

[49] I. Bitensky and E. Parilis, "Shock wave mechanism for cluster emission and organic molecule desorption under heavy ion bombardment," *Nuclear Instruments and Methods in Physics Research Section B: Beam Interactions with Materials and Atoms*, vol. 21, no. 14, pp. 26 – 36, 1987.

[50] A. Mozumder, *Advances in Radiation Chemistry, v.1*. Wiley -Interscience, New York, 1969.

[51] R. R. Lucchese, "Thermal spike model for heavy ion induced desorption from surfaces," *The Journal of Chemical Physics*, vol. 86, no. 1, pp. 443–453, 1987.

[52] A. W. Molvik, H. Kollmus, E. Mahner, M. K. Covo, M. C. Bellachioma, M. Bender, F. M. Bieniosek, E. Hedlund, A. Krämer, J. Kwan, O. B. Malyshev, L. Prost, P. A. Seidl, G. Westenskow, and L. Westerberg, "Heavy-Ion-induced electronic desorption of gas from metals," *Phys. Rev. Lett.*, vol. 98, p. 064801, Feb 2007.

[53] Y. Yamamura, "Theory of sputtering and comparison to experimental data," *Nuclear Instruments and Methods in Physics Research*, vol. 194, no. 13, pp. 515 – 522, 1982.

[54] A. Pfeiffer, *Operating Instructions, BALZERS TPH240*. BALZERS, 3 ed.

[55] A. Roth, *Vacuum Technology*. North-Holland, 1976.

[56] Balzers, *Partial pressure measurement in vacuum technology*. Balzers Instruments, 2008.

[57] "Pfeiffer vacuum, turbomolecular pump operating principle www.pfeiffer-vacuum.com/know-how/vacuum-generation/turbomolecular-pumps/design-operating-principle/turbomolecular-pump-operating-principle/technology.action?chapter=tec2.8.1.1."

[58] E. P. Degarmo, J. T. Black, and R. A. Kohser, *Materials and Processes in Manufacturing*. Wiley, 9th ed., 2003.

[59] C. Omet, H. Kollmus, H. Reich-Sprenger, and P. Spiller, "Ion catcher system for the stabilisation of the dynamic pressure in SIS18," in *Proceedings EPAC*, 2008.

[60] "Measurement computing daq software (www.mccdaq.com)."

[61] "MKS instuments, Microvision 2 www.mksinst.com/product/product.aspx?productid=184."

[62] J. Ziegler, "SRIM : www.srim.org."

[63] E. Hedlund, L. Westerberg, O. Malyshev, E. Edqvist, M. Leandersson, H. Kollmus, M. Bellachioma, M. Bender, A. Kramer, H. Reich-Sprenger, B. Zajec, and A. Krasnov, "Ar ion induced desorption yields at the energies 5-17.7 MeV/u," *Nuclear Instruments and Methods in Physics Research Section A: Accelerators, Spectrometers, Detectors and Associated Equipment*, vol. 599, no. 1, pp. 1 – 8, 2009.

[64] P. Spiller, L. Bozyk, H. Eickhoff, H. Kollmus, P. Puppel, and H. Reich-Sprenger, "Acceleration of intermediate charge state heavy ions in SIS18," in *Proceedings of IPAC10, Kyoto, Japan*, 2010.

[65] M. Burns, *Automated Fabrication*. Prentice Hall, 1993.

[66] F. Chautard, "Beam dynamics for cyclotrons," in *CERN accelerator school , Small accelerators;*, 2005.

Samenvatting

In het kader van het TRIμP onderzoeksprogramma naar schending van fundamentele symmetrien, dat op het KVI wordt uitgevoerd, wordt het AGOR cyclotron gebruikt om bundels zware ionen met een hoge intensiteit (¿10^{12} deeltjes per seconde) te produceren. Typische voorbeelden: ^{206}Pb met een energie van 8 MeV/amu en ^{20}Ne met een energie van 25 MeV/amu. Gedurende de bundelontwikkeling voor deze experimenten werd geconstateerd dat vacuum verslechtering ten gevolge van bundelverlies (en een terugkoppeling tussen bundel intensiteit en vacum verslechtering die daarvan het gevolg is) de maximaal haalbare bundelintensiteit beperkt. Dit proefschrift beschrijft een studie naar de factoren die bijdragen aan het bundelverlies, met name de terugkoppel mechanismen, en daarnaast een verkenning van mogelijke methoden om de sterkte van deze terugkoppeling te verminderen en daarmee de maximaal mogelijke bundelintensiteit te verhogen.
Positief geladen ionen die worden versneld in een cyclotron kunnen door botsingen met moleculen van de restgas atmosfeer (druk 10^{-7} mbar) een ladingsverandering ondergaan, waarna ze in een verstoorde baan verder bewegen. Deze omgeladen deeltjes blijven precederen in het cyclotron en ondergaan vervolgens weer ladingsveranderingen, totdat ze uiteindelijk tegen obstakels in het centrum of tegen de buitenrand van de vacum-kamer botsen. Bij deze botsing verliezen de deeltjes al hun energie en maken hierdoor materiaal vrij aan het oppervlak (desorptie). Het vrijkomende materiaal veroorzaakt een verslechtering van het vacum. Dit veroorzaakt een positieve terugkoppeling tussen bundelverlies en verslechtering van het vacum, die bij hoge intensiteiten steeds sterker wordt. Om dit bundel verlies proces te begrijpen, hebben we de verschillende processen onderzocht die bijdragen aan de terugkoppeling:

1. Ladingsverandering van bundeldeeltjes door botsingen met restgas: Er zijn twee soorten ladingsveranderingen mogelijk: vangst (van een extra elektron) en strippen (verlies van een elektron). De fractie van de bundeldeeltjes die een omlading ondergaat hangt af van de (energie afhankelijke) werkzame doorsnede van de interactie, de padlengte van het versnelde ion en de plaatselijke dichtheid (druk) van het restgas. Er bestaan verschillende semi empirische theorieen die de werkzame doorsnede voor vangst en strippen voor dergelijke ion-atoom interacties voorspellen. Met behulp van deze theorien

is een model gemaakt om de transmissie door het cyclotron voor verschillende bundels als functie van de druk te kunnen berekenen. Bij een lage bundel intensiteit zijn experimenten gedaan om de transmissie in het cyclotron te meten. De gemeten waardes zijn binnen de verwachte systematische onnauwkeurigheden (m.n. onzekerheid in de drukverdeling in het cyclotron, die niet gemeten kan worden) in overeenstemming met de voorspellingen van het model.

2. Baan dynamica: Na een ladingsverandering blijven ionen in het cyclotron 'baantjes draaien' totdat ze de buitenwand of obstakels in het centrum van de versneller raken. De banen van de ionen na een ladingsverandering zijn gesimuleerd en hieruit is bepaald waar en onder welke hoek de deeltjes op de wand vallen. Uit deze simulaties blijkt dat de meeste ionen na een enkele ladingsverandering blijven ronddraaien in een iets uit het centrum liggende baan. Pas na meerdere ladingsveranderingen wordt de baan instabiel en botsen de deeltjes ergens op de wand. De afwijking van de nominale baan, waarbij de deeltjesbaan instabiel wordt, is afhankelijk van de straal van de baan. Voor laag-energetische deeltjes is een grotere afwijking nodig om de baan instabiel te maken dan voor hoog-energetische deeltjes. Dit betekent dat laag-energetische deeltjes, die in het midden van het cyclotron ronddraaien, meer ladingsveranderingen moeten ondergaan voordat hun baan instabiel wordt dan hoog-energetische deeltjes, waarvan de baan zich aan de rand van het cyclotron bevindt. Deze laatsten botsen met een kleine hoek van inval (tussen 0 - 5 graden) op de wand. Op kleinere straal hebben de ionen die uit de bundel verloren gaan een lagere energie en een grotere spreiding in invalshoek, waardoor ze minder materiaal uit de wand vrijmaken.

3. Desorptie door ionen: Door de energie, die de ionen in de wand van het cyclotron deponeren wordt materiaal van het oppervlak vrijgemaakt (desorptie). Om dit effect te kunnen kwantificeren zijn experimenten buiten het cyclotron uitgevoerd dooreen aantal materialen, die representatief zijn voor het binnenste van de versneller, te bestralen met verschillende ionenbundels. Resultaten uit de literatuur van de desorptie opbrengst zijn niet direct toepasbaar op onze situatie, aangezien geen van deze experimenten de voor ons relevante regimes van druk, energie en hoek combineert:

    - AGOR werkt met een basisdruk van ongeveer 10^{-7} mbar, terwijl de meeste experimenten bij een veel lagere druk van 10^{-10} mbar zijn uitgevoerd.
    - Het voor ons relevante energie gebied is tot ongeveer 10 MeV/amu. Andere experimenten zijn veelal uitgevoerd bij hogere energie (zoals van

150 MeV tot GeVs).

- Uit de baan berekeningen blijkt dat vooral kleine invalshoeken van belang zijn. Eerdere experimenten hebben deze hoeken niet in detail onderzocht.

Onze experimenten laten zien dat de desorptie opbrengst evenredig is aan de bundel intensiteit en omgekeerd evenredig aan de invalshoek. Met behulp van een restgas analysator hebben we data verzameld voor de verschillende soorten moleculen die van de wand worden gedesorbeerd en vastgesteld dat deze omgekeerde evenredigheid geldt voor alle soorten moleculen waarvan een significante hoeveelheid werd gemeten.
Van de onderzochte materialen bleek aluminium de laagste desorptie opbrengst te hebben. Het bedekken van koper met een goudlaagje verminderde de desorptie opbrengst met een factor twee, terwijl op basis van de literatuur een verbetering met een factor tien verwacht werd.
De gemeten desorptie opbrengsten zijn ruwweg 10^3 moleculen per ion dat op de wand botst, in overeenkomst met in de literatuur gevonden waardes. Echter, onze uitkomsten zijn niet in overeenstemming met de voorspellingen van bestaande modellen, met name het thermal spike model. Aangezien het thermal spike model is ontwikkeld voor loodrechte invalshoek en zich beperkt tot oppervlakte effecten, verwachten we dat een 3-D uitbreiding van dit model (welke rekening houdt met de bijdrage van onderliggende lagen van het materiaal) de verschillen met onze metingen kan verklaren. Dit valt echter buiten het bestek van dit proefschrift.

Om de transmissie te verbeteren is het noodzakelijk de bundelverliezen te verminderen. Uit onze studies concluderen we dat het verhogen van de effectieve pompsnelheid in het cyclotron verreweg de beste manier is om dit te bereiken. De geometrie van de vacumkamer van het AGOR cyclotron maakt het echter onmogelijk de effectieve pompsnelheid substantieel te verhogen.
Andere mogelijkheden om de desorptie te verminderen en daarmee de maximaal haalbare bundelintensiteit te verhogen zijn:

- Schrapers: Het introduceren van schrapers op strategische punten van de buitenwand van de vacumkamer om de hoek waaronder ionen op de wand vallen te vergroten en daarmee de desorptie te verminderen. In het AGOR-cyclotron is dit geen optie omdat de versnelde bundel vlak langs de wand scheert zodat schrapers ook een deel hiervan onderscheppen. .

- Coating van het oppervlak: Het coaten van het oppervlak kan de desorptie-opbrengst verminderen. Aluminium is een goede kandidaat als coating mate-

riaal, omdat het de laagste desorptie opbrengst blijkt te hebben. De duurzaamheid en uitvoerbaarheid van een dergelijke coating moeten nog nader onderzocht worden.

- Oppervlakte behandeling: Langdurig schoonbranden van het oppervlak door invallende bundel veroorzaakt een langzame verbetering van het vacum. Deze methode is echter niet duurzaam.

Samenvattend concluderen we uit onze experimenten dat de desorptie, die veroorzaakt wordt door op de wand botsende ionen, de mogelijkheid om met het AGOR cyclotron (en vergelijkbare versnellers) een bundel zware ionen met hoge intensiteit te produceren aanzienlijk beperkt. Er zijn weliswaar mogelijkheden deze beperkingen enigszins te verminderen, maar voor een echte oplossing had al tijdens de ontwerpfase de geometrie van de vacumkamer geoptimaliseerd moeten worden qua pompsnelheid. Bij het ontwikkelen van nieuwe versnellers van zware ionen bundels met hoge intensiteit moet daarom al tijdens het ontwerp aandacht besteed worden aan een maximale pompsnelheid en het verminderen van desorptie.

Acknowledgments

The work done in this thesis would not have been possible without the constant help and support of Prof. dr. Sytze Brandenburg, Dr. Mariet Hofstee, Dr. Marc-Jan van Goethem and others in the AGOR cyclotron group.
The help and support from my supervisor Mariet Hofstee, has helped me a lot in my learning experience. Thank you for all the help and advice through these four years. I am especially grateful for the ready response you had to all my queries whenever I would land up at your office. Such a steep learning curve could not be scaled individually. It was a lot of fun working with you and the words 'Don't Panic' is something I am sure to remember in all my future endeavours.
I am also grateful to my promoter Sytze Brandenburg for his guidance and his suggestions, especially during the times he put me back on track whenever I would get stuck or digress. Our discussions about accelerators, AGOR and all other topics were always informative and interesting.
I would like to thank Marc-Jan van Goethem especially for his help in the simulations and the experimental design. It was always a pleasure to discuss ideas with you and to share our inputs.
I am grateful to the members of my reading committee: Prof. dr. K. Hatanaka, Prof. dr. ir. O.J. Luiten and Prof. dr. ir. R. Hoekstra for their time in carefully reading my thesis.
I would like to express my gratitude to Harry Kiewiet for all his assistance during the design of the experimental setup and the experiments. I also thank Henk Gorter for all his input and his suggestions for all vacuum related issues.
A successful beamtime experiment would not have been possible without the help Emiel van der Graaf, Reindt Ostendorf, Hans Beijers, Vladimir Mironov, Josbert Mulder, Jan de Jong, Jan Mulder and Rob Kremers. I would also like to thank the cyclotron operators group: Harm, Niek, Roel, Ronald, Remco, Dennis and Dragos for their help during all the experiments.
I would also thank all the people working in the mechanical, electronics and IT

group at the KVI for their help at various stages in my experiments. I am also grateful to KVI financial and personnel section for all the help during my stay in KVI.
Staying four years away from home is not easy and thanks to my colleagues in KVI my stay in Groningen was quite memorable: Jordy, Krijn, Ina, Gabriel, Ruud, Renato, Hong, Daren, Duurt, David, Mayer, Olmo, Wilbert, Oksana, Ola, Oscar, Sybren, Stefan, Simona, Victor, Ganesh, Suresh, Manisha, Gouri and Kalpana. Olena, Olga, Ali and Qader: would miss all the lunch discussions with you guys.
Groningen would not have been the same without Sujata Ghosh and Avik Kumar Maitra. Soumya, Dipayan, Sreekanth, Pavan and Neha: it was a pleasure to share life with you guys.
Bodha - Thanks and all the best!
Special thanks to Avik Kumar Maitra and Abhishek Majumder for designing the cover on such short notice.
Finally, these acknowledgments would not complete without the support of my teachers, friends and family. I wish to thank my teachers at school and university and my research guides at HRI and PRL. Dhara, you are always a darling! Sir and Miss: Thanks for being a part of the journey. Didi: Yes! My parents, who have constantly supported me have always been a lifeline. Last of all for my wife Ishita, whose ready encouragement, infinite patience and minor textual corrections has been a major contribution : Yaaaayyyy !
To my roots - Durgapur, Kharagpur and Groningen, 'So long and thanks for all the fish !'

Ayanangsha Sen
Groningen
February 14, 2013